

Drag Reduction in Turbulent Flows by Polymers and Surfactants

An Experimental Study Into the Mechanisms of Drag Reduction by Additives

A. Toutouh



2018

Azeddine Toutouh

Drag Reduction in Turbulent Flows by Polymers and Surfactants

Drag Reduction in Turbulent Flows by Polymers and Surfactants

An Experimental Study Into the Mechanisms of Drag Reduction by Additives

By

Azeddine Toutouh

In partial fulfillment of the requirements for the degree of

Master of Science

in Applied Earth Sciences

Petroleum Engineering and Geosciences

at the Delft University of Technology,

to be defended publicly on Thursday August 30, 2018 at 15:00

Supervisors:	Prof. Dr. J. Bruining	(Delft University of Technology)
	Dr. A. Fadili	(Shell Global Solutions B.V.)
	Dr. S. Vincent-Bonnieu	(Shell Global Solutions B.V.)
	Dr. S. Jones	(Delft University of Technology)
Thesis committee:	Prof. Dr. P.L.J. Zitha, (Chair)	(Delft University of Technology)
	Prof. Dr. H. Bruining	(Delft University of Technology)
	Dr. A. Fadili	(Shell Global Solutions B.V.)
	Dr. D. V. Voskov	(Delft University of Technology)
	Dr. K.H.A.A. Wolf	(Delft University of Technology)



2018

Azeddine Toutouh

Drag Reduction in Turbulent Flows by Polymers and Surfactants

Abstract

In 1949, Toms (Toms B.A., (1949, 1977)) observed that small amounts of a drag reducing agent (DRA) could cause a considerable drag reduction in turbulent pipe flow. In application of polymer enhanced oil recovery, degradation of polymers in the supply lead could cause clogging. It was, however observed that surfactants at sufficiently high concentration also showed drag reduction without the problem clogging. A DRA reduces the energy loss by friction and unstable flow, thus improving injection throughput with the same pressure pump and thereby reducing the exergetic pumping costs. This study investigates experimentally the drag reducing capacity of surfactants and compares it to the drag reducing capacity of polymers.

For the experiment, a set-up consisting of a pump, a coiled test tube with a length of 1.48 m and an inner diameter of 0.5 mm and pressure gauges is built. The diameter of the coil is 12.5 cm. We use a pump capable of injection up to 200 ml/min. The pressure drop is measured between the entrance and end of the tube. The injection rate is varied between 1 and 200 ml/min, roughly corresponding to Reynolds numbers between 50 and 10,000. The additives are dissolved in brine with a 33,000 ppm salt concentration. The viscosity of the solution is dependent on the concentration of the DRA. The ratio of the measured pressure drop with only brine and the pressure drop with the DRA solution was used to calculate the drag reduction (DR) factor, as from a technical point of view we are only interested whether adding DRA reduces the drag with respect to the original brine solution. From an academic point of view, we remark that for low concentrations the viscosity enhancement due to the presence of the DRA is negligible. As polymers we use xanthan (a biopolymer), and a synthetic emulsion polymer based on polyacrylamide. Maximum DR factors are 23% for xanthan at 90ppm and 32% at 90ppm for the synthetic emulsion polymer. DR only occurs at turbulent conditions.

Three types of surfactants, each from a different branch of surfactants are used in this study. The surfactants used are AOS { α -Olefin Sulfonate}, CTAB {hexadecyltrimethylammonium bromide} and APG {Alkyl PolyGlucoside} which are a cationic, anionic and a nonionic surfactant respectively. The surfactants did not show any DR at (for DRA applications) high concentrations up to 20,000ppm. Addition of Sodium Salicylate (NaSal) to CTAB with a 1:1 ratio led to a maximum DR of 33% at 2500 ppm concentration.

Several pressure gauges have been installed along the test tube in order to observe how the pressure drops along the tube, how the DRAs affect these pressure drops and at what location of the test tube the DR factor is the highest. It is found that xanthan has the same DR factor at each location of the test tube, the emulsion polymer has a decreasing DR factor as the distance from the inlet of the test tube increases and the CTAB+NaSal DRA has an increasing DR factor as the distance from the inlet increases.

The DRAs are sheared using a constriction in the flow loop while the degradation is monitored. It is observed that xanthan is less susceptible to degradation in comparison to the emulsion polymer due to its more rigid chemical structure. But xanthan and the emulsion polymer would be inefficient to use in looped flow systems as they are affected by degradation. The CTAB+NaSal DRA on the other hand shows no degradation meaning that the micellar rod-like structures that give the DR effect are being repaired when the shear force is being removed. However, for surfactants higher concentrations (1000-2500 ppm) are required.

2018

Azeddine Toutouh

Drag Reduction in Turbulent Flows by Polymers and Surfactants

Acknowledgements

All praises and thanks be to Allah the Almighty, the Most Beneficent, the Most Merciful

First and foremost I would like to express my gratitude to my supervisor Prof. Dr. J. Bruining for his support, encouragement and valuable feedback throughout this challenging process. I would also like to thank my other supervisors, Dr. A. Fadili and Dr. S. Vincent-Bonnieu for giving me the opportunity to pursue this topic in cooperation with Shell and guide me through it.

Secondly I want to thank Dr. S. Jones for her support and insightful comments during this process. This work would not have been possible without her support.

And last but not least I would like to express my deepest gratitude to my parents, my brothers and my sisters. This academic achievement would not have been possible without their unconditional support.

*Azeddine Toutouh
Amsterdam, August 2018*

2018

Azeddine Toutouh

Drag Reduction in Turbulent Flows by Polymers and Surfactants

Contents

Abstract	i
Acknowledgements	iii
Nomenclature.....	3
List of Figures and Tables	5
Figures	5
Tables	7
1. Introduction	8
1.1. Research Objectives.....	9
1.2. Scope of Work.....	10
1.3. Thesis Organization.....	10
2. Theory and Key Concepts.....	11
2.1. General Aspects of Drag Reduction	11
2.1.1. Drag reduction mechanisms.....	12
2.2. Drag Reduction Using Polymers.....	14
2.2.1. The polymers used in this study	14
2.3. Drag Reduction Using Surfactants	15
2.3.1. Micellar shapes.....	16
2.3.2. The surfactants used in this study	17
2.4. Turbulent and Laminar Pipe Flow	18
2.5. Degradation of DRAs.....	21
2.6. Viscosity sensor.....	22
3. Experiments	23
3.1. Materials and Methods.....	23
3.1.1. Brine composition.....	23
3.1.2. Solution preparations	24
3.2.1. Phase 1: Pressure Drop measurements and DRA screening	25
3.2.2. Phase 2: Rheology, pressure drop localization and degradation	28
4. Numerical Model	32
4.1. Laminar flow	32
4.2. Turbulent flow.....	32
4.2.1. The $k - \epsilon$ model.....	33

4.2.2.	Wall functions.....	33
4.2.3.	Boundary conditions.....	34
5.	Results and Discussion	35
5.1.	Pressure Drop Measurements, Validation of Set-up	35
5.2.	Drag Reduction By Polymers.....	36
5.2.1.	Xanthan.....	36
5.2.2.	FLOPAAM EM5205.....	38
5.2.3.	Polymer DRA comparison	40
5.3.	Drag Reduction by Surfactants	41
5.3.1.	Critical Micelle Concentrations.....	41
5.3.2.	Hydrated particle diameter and anisotropy	43
5.3.3.	Drag reduction.....	44
5.4.	Rheology	47
5.4.1.	Shear rheology of the polymeric solutions.....	47
5.4.2.	Shear rheology of the surfactant solutions	48
5.5.	Pressure Drop Localization	49
5.6.	Drag Reducing Agent Degradation.....	52
5.6.1.	Degradation monitoring using pressure drop	52
5.6.2.	Degradation monitoring using in-line viscosity sensor.....	53
5.7.	Numerical Results	56
6.	Conclusion.....	58
7.	Recommendations	60
	Appendix A: z-Average	61
	Appendix B: Rheology of non DR surfactants	62
	Appendix C: Degradation Monitoring Using the Rheometer.....	63
	Appendix D: Calibration of the In-line Viscosity Sensor.....	64
	Appendix E: Connection of a Core Flood Set-up	66
	Appendix F: PHREEQC Geochemical Simulation	67
	Bibliography.....	69

Nomenclature

In order of appearance

<i>DRA</i>	Drag Reducing Agent	
<i>DR</i>	Drag Reduction	
<i>%DR</i>	Drag Reduction factor	
<i>AOS</i>	α -Olefin Sulfonate	
<i>CTAB</i>	hexadeCylTrimethylAmmonium Bromide	
<i>APG</i>	Alkyl PolyGlucoside	
<i>NaSaL</i>	Sodium Salicylate	
<i>EOR</i>	Enhanced Oil Recovery	
<i>CMC</i>	Critical Micelle Concentration	
<i>DLS</i>	Dynamic Light Scattering	
<i>CMC_{II}</i>	Transition concentration from spherical micelles to rod-like or cylindrical micelles	
<i>V</i>	Volume of the hydrophobic group	[m ³]
<i>l</i>	Length of the hydrophobic group	[m]
<i>a</i>	Cross sectional area of the hydrophilic group	[m ²]
<i>A</i>	Cross sectional area of the pipe	[m ²]
ρ	Fluid density	[kg/m ³]
<i>v</i>	Fluid velocity	[m/s]
<i>s</i>	Coordinate along the pipe	[m]
<i>t</i>	Time	[s]
<i>p</i>	Pressure	[Pa]
<i>F_g</i>	Gravity force	[N/m]
<i>F_f</i>	Friction force	[N/m]
μ	Dynamic viscosity	[Pa · s]
<i>f</i>	Moody friction factor	[-]
<i>D</i>	Pipe diameter	[m]
<i>N_{Re}</i>	Reynolds number	[-]
ϵ	Absolute pipe roughness	[-]
<i>Q</i>	Flowrate	[m ³ /s]
<i>e</i>	Pipe roughness	[m]
Δp	Pressure drop without DRA	[Pa]
Δp_{DRA}	Pressure drop with DRA	[Pa]
<i>F</i>	Force exerted at center of the chain	[N]
η	Viscosity of the solvent	[Pa · s]
$\dot{\epsilon}$	Strain rate	[s ⁻¹]
<i>M_w</i>	Molecular weight	[u]
<i>K, α</i>	Mark-Houwink parameters	[-]
<i>AV</i>	Acoustic Viscosity	[-]

WF	Weight of filled syringe	[g]
WE	Weight of emptied syringe	[g]
W	Weight of added polymer	[g]
Q_w	Amount of added brine	[g]
CE	Activity of the emulsion polymer	[%]
w_t	Total weight	[g]
w_{surf}	Weight of the surfactant	[g]
w_{brine}	Weight of the brine	[g]
CE_{surf}	Activity of the surfactant	[%]
γ	Surface tension	[N/m]
ω_0	Constant angular velocity	[rad/s]
$\dot{\gamma}$	Shear rate	[s ⁻¹]
$r_{1,2}$	Radius of cylinder 1 or 2	[m]
τ	Shear stress	[Pa]
M	Torque	[N · m]
H	Height of cylinder	[m]
u	Fluid velocity	[m/s]
ζ	Second viscosity	[-]
M_{Nr}	Mach number	[-]
c	Velocity of sound through a certain medium	[m/s]
k	Turbulent kinetic energy	
ϵ	Dissipation	
μ_T	Turbulent viscosity	
η_0	Low-shear Newtonian viscosity	[Pa · s]

List of Figures and Tables

Figures

Figure 1-1: Diagram showing the process of this study.....	10
Figure 2-1: Classification of drag reducing methods	12
Figure 2-2: (a) A schematic drawing of a polymer being distorted by the flow. (b) The elastic dumb-bell model of a distorting polymer. (Hinch, E.J., 1977)	13
Figure 2-3: Schematic structure of the main part of the two polymers used in this study where, a) polyacrylamide and b) xanthan.....	15
Figure 2-4: Schematic Phase diagram for surfactant solutions (Lu, B. (1997))	16
Figure 2-5: Transition from (a) monomers to (b) spherical micelles to (c) rod like micelle structures.	17
Figure 2-6: Schematic structure of the different kind of surfactants where, a) AOS, b) APG and c) CTAB	17
Figure 2-7: Stream line and velocity profile of (a) laminar flow and (b) turbulent flow	19
Figure 2-8: Friction factor as function of Reynolds number for different values of dimensionless roughness ϵ . The graph is split into three parts depicting three flow regimes, viz., A= laminar-, B= transitional- and C= turbulent flow regime.....	20
Figure 2-9: Sensor surface showing the TSM of vibration	22
Figure 3-1: Schematic view of the phase 1 of the experiments	26
Figure 3-2: Kibron tensiometer used to measure the surface tension.....	26
Figure 3-3: Du Noüy-Padday method for measuring the surface tension.....	27
Figure 3-4: Concentration against the measured surface tension for a surfactant.	27
Figure 3-5: Malvern Zetasizer Nano ZS	27
Figure 3-6: Schematic view of the main components in a DLS device	28
Figure 3-7: The Anton Paar MCR302 rheometer used for the rheology study	29
Figure 3-8: Schematic view of the concentric cylinder system filling	29
Figure 3-9: Top view of the concentric set-up with coquette flow.	29
Figure 3-10: Schematic view of phase 2 of the experiment.....	30
Figure 3-11: Test tube used for the pressure drop localization	31
Figure 3-12: Tee (T) fitting connection for the in-line BAW viscosity sensor	31
Figure 4-1: Velocity profile along the pipe wall where the fluid close to the wall is divided into four sublayers...	33
Figure 4-2: True flow field and computed flow field when using wall function.....	34
Figure 5-1: Pressure drop measurements at each flow rate for brine. A transition where the pressure drop increases is clearly visible between a flow rate of 70 ml/min and 80 ml/min	35
Figure 5-2: Reynolds number against the friction factor. The friction factor is derived from the experimentally obtained pressure drops. The black line shows the friction factor for laminar flows and approximately satisfies $f = 64/NRe$	36
Figure 5-3: Flow rate against the pressure drop for different concentrations of xanthan dissolved in brine	37
Figure 5-4: Flow rate against the pressure drop at turbulent flow for the different concentrations of xanthan dissolved in brine.....	37
Figure 5-5: Flow rate against the %DR for the different concentrations of xanthan dissolved in brine	38
Figure 5-6: Flow rate against the pressure drop for different concentrations of emulsion polymer dissolved in brine	39
Figure 5-7: Flow rate against the pressure drop for different concentrations of emulsion polymer dissolved in brine	39

Figure 5-8: Flow rate against the %DR for the different concentrations of emulsion polymer dissolved in brine .	40
Figure 5-9: Maximum %DR and %DR at 200 ml/min as function of concentration for the polymeric solutions used in this study.....	40
Figure 5-10: Friction factor as function of Reynolds number for the polymeric solutions at various concentrations	41
Figure 5-11: Surface tension as function of the logarithm of surfactant concentration, where (a) AOS, (b) APG and (c) CTAB. The arrow points out the critical micelle concentration	42
Figure 5-12: z-Average diameter as function of the AOS concentration. The error bars depict the standard deviation calculated from the successive measurements at each concentration	44
Figure 5-13: (a) Pressure drop as function of flowrate for the surfactants and brine as baseline. All the data points for the surfactant solutions coincide with the data points obtained for brine, meaning that the solutions do not show any DR. (b) %DR as function of flowrate for the surfactants. All data points are close to 0 or lower than zero meaning no significant DR occurs. The surfactant concentrations are 10.000 ppm and the ratio between APG and 1-pentanol is 1:1. The ratio 1:0.15 shows the same result.	45
Figure 5-14: (a) Pressure drop as function of flowrate for the CTAB+NaSaL solutions and brine as baseline. The data points for 100 ppm solution coincide with the data points obtained for brine, this solution therefore does not reduce drag. (b) %DR as function of flowrate for the CTAB+NaSaL solutions. All data points for the 100 ppm solution are close to 0 also implying that this solution does not reduce drag. The other concentrations reduce drag significantly when the flow is turbulent	46
Figure 5-15: Maximum %DR and %DR at 200 ml/min as functions of concentration for the CTAB+NaSaL surfactant	47
Figure 5-16: Viscosity as function of shear rate for the polymeric solutions used in this study.....	48
Figure 5-17: Viscosity as function of shear rate for different concentrations of CTAB+NaSaL.	49
Figure 5-18: Schematic view of the placement of the pressure gauges along the test tube and the names for the pressure drop calculations	50
Figure 5-19: Distance from the inlet of the test tube against the pressure for: (a) a laminar flow of 50 ml/min and (b) a turbulent flow of 200 ml/min. The concentrations are 90 ppm, 90 ppm and 2500 ppm respectively for xanthan, EM and CTAB+NaSaL	50
Figure 5-20: Pressure drop over each interval normalized over one meter. The pressure drop calculations are taken at a flow rate of 200 ml/min	51
Figure 5-21: %DR at each interval over which the pressure drop is calculated. The pressure drop calculations are taken at a flow rate of 200 ml/min	51
Figure 5-23: DR as function of time for the different DRAs at a flow rate of 140 ml/min.....	53
Figure 5-23: Pressure drop evolution over time for the DRAs at a flow rate of 140 ml/min.....	53
Figure 5-24: Acoustic viscosity (AV) as function of time for the DRAs.....	54
Figure 5-25: Elbow fitting used to connect the viscosity sensor to the flow loop. A dead volume where no flow occurs is marked green	55
Figure 5-26: Recommended way of connecting viscosity sensor to the flow loop	55
Figure 5-27: Surface plot of the velocity over the first 100 mm of the test tube. The flow enters the test tube from left and flows to the right. Note that the velocity field takes approximately 70 mm to fully develop. The same can be seen in the three dimensional plot. The velocity profiles at laminar and turbulent flow are also plotted. Note that usage of the $k - \epsilon$ model for turbulent flow simulation does not result in having a zero velocity at the boundary wall.....	55
Figure 5-28: Velocity profile derived using the low Reynolds number $k - \epsilon$ model. Note that the velocity is zero at the wall.....	56

Figure 5-29: Pressure along the length of the tube and the fully developed velocity along the radius of the tube for a velocity of 4.24 m/s and a velocity of 16.97 m/s respectively	57
Figure A: Viscosity as function of shear rate for the solutions that did not show DR	62
Figure B: Viscosity as function of shear rate for the different DRAs both for a fresh prepared solution as a for 2 days sheared solution	63
Figure C: Viscosity against concentration glycerol	64
Figure D: Viscosity against glycerol concentration for the dynamic viscosity and the theoretical viscosity	65
Figure E: Schematic view of the set-up where a core flood set-up is attached.....	66

Tables

Table 2-1: Typical values for v/la and their corresponding micellar shapes (Zakin, J.L., et al., (1998))	16
Table 3-1: Brine composition (Synthetic Seawater)	23
Table 4-1: Turbulence model parameters.....	33
Table 5-1: CMC values for the three different surfactants measured at a temperature of $23.5^{\circ}\text{C} \pm 0.5^{\circ}\text{C}$	43
Table 5-2: z-Average diameters and polydispersity index values obtained for AOS. All samples are measured at least three times successively and the values in the table depict the averages of the obtained values.....	44
Table A: Information of the used solutions for calibrating the sensor	64
Table B: Data obtained from the viscosity sensor whilst being connected to the flow loop. The theoretical viscosity is calculated using the equation provided earlier.	65

1. Introduction

Turbulent flow in pipes causes additional energy losses by friction and unstable flow leading to an increased pressure loss. The objective of a Drag Reducing Agent (DRA) is to reduce the energy loss by friction and the instability of the flow, thus improving injection throughput with the same pumping energy, which reduces the pumping costs. This improvement can be obtained by adding low concentrations of a DRA to the injection stream. DRAs reduce the pressure loss by reducing the level of turbulent eddies in the flow. Drag reduction (DR) in turbulent flow was first discovered by Toms in the summer of 1946 and his results were eventually published at an international congress in Holland in 1949 (Toms, B.A., (1949)). Since this publication progress has been made and significant advances in the field of DR both practical and theoretical have occurred as is recently reviewed by Tiong, et al., (2015). Still the exact mechanisms of turbulent DR by additives remain unresolved until today.

DRAs have several applications in the petroleum industry and the district heating/cooling industry (Hellsten, M. (2002), Huang, T. (2007), (Burger, E.D, et al., (1982))). This research will focus on polymeric and surfactant agents for DR. Polymers and surfactants are also used in Enhanced Oil Recovery (EOR) applications. Polymers are added to the injected water to increase its viscosity, improving the mobility ratio and therefore favor an enhanced displacement efficiency and areal/vertical sweep-efficiency. Surfactants are used in EOR applications to lower the interfacial tension of oil, allowing the oil to be displaced more efficiently. The same polymer or surfactant that can be classified as a DRA can thereby in theory also be used to enhance the oil recovery.

Usage of polymers is often limited to once-through systems because of degradation. In circulating fluid systems, degradation of polymers can cause loss of DR. For these systems drag reducers based on surfactants may be preferred. In this study two kinds of polymers and three kinds of surfactants are tested on their DR abilities. The polymers used are xanthan and an emulsion polymer based on polyacrylamide, which are a biopolymer and a synthetic polymer respectively. The surfactants used are α -Olefin Sulfonate (AOS), hexadecyltrimethylammonium bromide (CTAB) and Alkyl Polyglucoside (APG) which are a cationic, anionic and a nonionic surfactant respectively.

1.1. Research Objectives

The main objective of this study is to create an experimental set-up that can be used to evaluate the DR abilities of certain agents. The agents are comprised of polymers or surfactants. In order to achieve this main objective certain sub objectives can be formulated:

- determine the critical micelle concentration for the different surfactants and quantify the degree of DR at these concentrations;
- quantify the degree of DR for the polymers
- quantify the DR factor of the used additives and determine what additives can be classified as an DRA;
- perform rheological measurements on the solutions used to help determine a mechanism for explaining the DR;
- investigate whether the pressure drop along the tube drops gradually. Examine the effect of the DRA and its dependence on the position in the tube in terms of the pressure drop;
- examine the importance of degradation on the drag reducing abilities of the DRAs;
- quantify the degradation of the polymers using a bulk acoustic wave viscosity sensor;
- develop a numerical model for turbulent flow and compare the model with the experimental results.

1.2. Scope of Work

This study starts with a thorough literature review into the different kind of drag reducing methods. After this a set of possible DRA is selected and a set-up is built with a flow loop that can realize turbulent flow conditions. The set-up consists of pressure sensors along a small diameter tube. DRA solutions are made by dissolving the chosen concentration of a DRA in brine with a 33.000 ppm salt concentration. Critical Micelle Concentration (CMC) of the surfactants is determined using a surface tension meter. The concentration at which the surfactants form large aggregates cylindrical rod-like micelles is measured using Dynamic Light Scattering (DLS).

Addition of multiple pressure gauges along the tube made it possible to gain insight into the drop of pressure along the tube and how the DRA affects this drop. Polymer degradation is quantified by monitoring the DR factor, and the viscosity change using an in-line bulk acoustic wave viscosity sensor over time whilst the DRAs are being sheared. Finally a numerical turbulent flow model is developed using COMSOL and these results are compared with the experimental results.

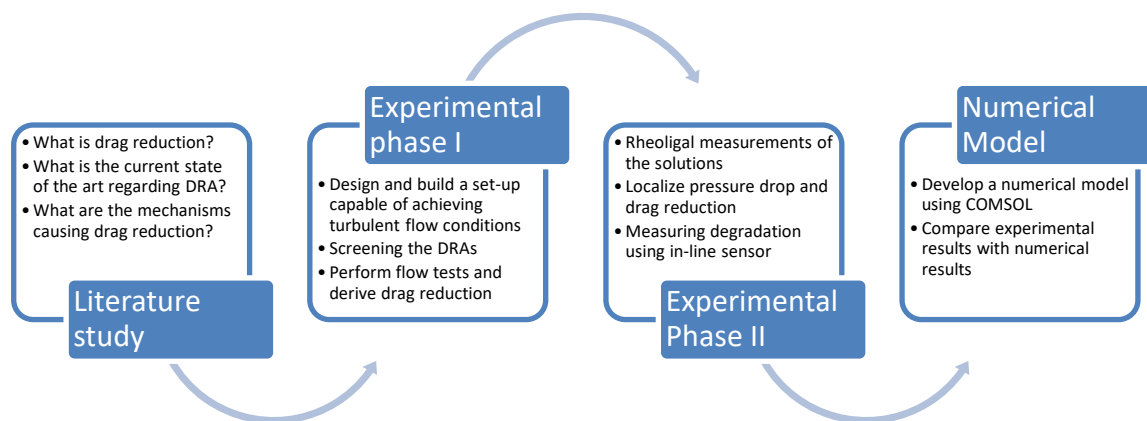


Figure 1-1: Diagram showing the process of this study

1.3. Thesis Organization

This thesis is comprised of 7 chapters. Chapter 1 gives an introduction into the matter while also stating the motivation and objectives. In chapter 2 relevant literature is cited, which give the reader a broader insight into the matter. Chapter 3 contains information about the experimental set-up and the methods used to obtain the useful results. Chapter 4 describes the numerical model used to simulate turbulent flows. The results are highlighted and discussed in chapter 5. The conclusions of this work are listed in chapter 6. Chapter 7 contains the recommendations that have emerged as a result of this research.

2. Theory and Key Concepts

This chapter reviews the key concepts and theory behind drag reduction (DR). For quantitative purposes drag reduction is defined as the pressure drop in the presence of a drag reducing agent divided by the pressure drop of the brine solution in the absence of a drag reducing agent (Li, P.W., et al., (2000)). Different kinds of drag reducing techniques and their accompanying pros and cons will be discussed in this chapter. Also the applications of DR will be highlighted. In order to obtain a further insight into the mechanisms of DR, multiple theories about the mechanisms of DR will be discussed. In this study surfactants and polymers are tested as a DRA. This chapter summarizes the previous work done using these agents as drag reducers and will also show the chemical structure of the possible DRAs used in this study. Furthermore will this chapter discuss the general concepts of pipe flow and turbulence and how degradation can be quantified using the in-line viscosity sensor.

2.1. General Aspects of Drag Reduction

Drag reduction can be achieved using non-additive and additive techniques as can be observed in Figure 2-1. Non-additive techniques can be labelled as techniques that need a physical adjustment of the flow medium in order to achieve DR. Additive techniques are techniques where something is added to the flow and that addition leads to DR. Non-additive techniques are comprised of wall surface modifiers like riblets, dimples, oscillating walls, compliant surfaces or even microbubbles. Non-additive drag reduction techniques have the advantage over additive techniques that they are all considered environmentally acceptable and do not alter the physical and chemical properties of the fluids. From the non-additive DR techniques microbubbles are reported to achieve the highest DR (up to 80%). However, microbubbles are not suitable for pipe flow as the bubbles tend to coalesce decreasing the DR (Wu, S. J., (2007)). Furthermore, the mechanisms of DR by microbubbles are complex and poorly understood (Wu, S. J., (2008)). Other non-additive techniques that can be used in pipe flow are usage of riblets and oscillating walls. Usage of riblets can lead to a practical DR of 5-8% and requires little to no maintenance. Using riblets as a DR technique is challenging as the effect of riblet spacing on DR is poorly understood and an inaccurate riblet configuration can increase the drag. Usage of oscillating walls can achieve a DR up to 46%, but installation and maintenance of this technique is complex (Abdulbari, H.A., et al., (2013)).

Additive techniques for DR are usage of fibers, surfactants and polymers. Additive techniques for DR are less suitable for industries where the physical and chemical properties of the fluid are important for product quality (e.g., food industry and pharmaceutical industry). This study will focus on the drag reducing ability of two additives, namely surfactants and polymers. Besides the great impact DR can have on the petroleum industry, numerous other applications of DR are possible. In aviation for example filling the fuel tanks can take a long time. In order to speed this up all major airports use DRAs to speed up filling the fuel tank. This decreases the fueling time in most airports almost by half (Brostow, W., (2008)). A further incomplete list of DR applications is stated below:

- fluid transportation (e.g., oil pipelines)
- sewer systems
- flood water disposal
- fire fighting
- irrigation
- water heating and cooling systems
- blood flow
- formula-1

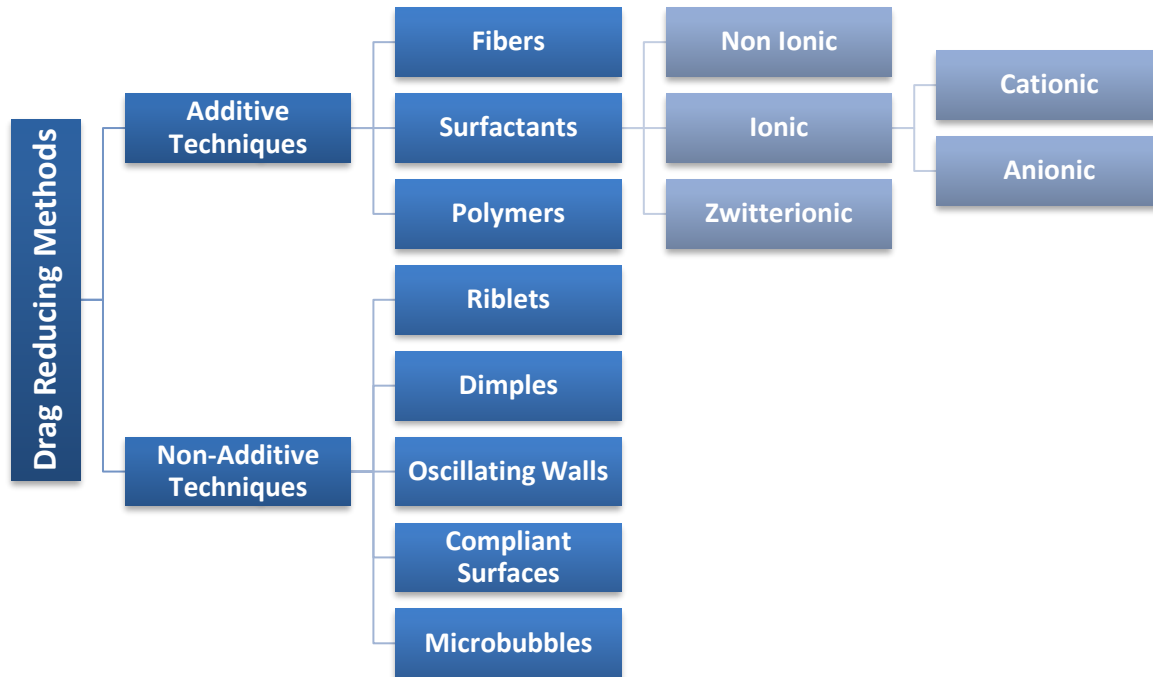


Figure 2-1: Classification of drag reducing methods

2.1.1. Drag reduction mechanisms

As flowrate increases in a pipe, so does turbulence. Forces near the pipe wall exceed the liquids ability to slip past itself. Eddies spin off and swirl through the flow producing turbulence that causes inefficient pipeline flow and wasted energy. At higher flow rates greater turbulence causes higher operating pressure limiting the throughput of the pipeline. DRAs reduce pipeline turbulence by interacting with the turbulent eddies, causing them to diminish. In principle this interaction can be explained in at least two ways. Namely, the DRAs reduce the formation of turbulent eddies, i.e., reduce the production of turbulent energy and the other way is to reduce the dissipation of energy into heat.

Multiple theories are stated which depict the way in which the DRA molecules interact with the turbulent flow. Lumley (1969) attributes DR by polymers to molecular extension of the polymer molecules. DR polymer molecules transition from a coiled state to a more stretched state due to the straining flow field leading to an increased extensional viscosity. The onset of this transition occurs when the relaxation time of the molecule is longer than the timescale of turbulence. These stretched out polymer molecules act as shock absorbers, reducing the overall level of turbulence in the pipe. Hinch (1977) agreed that the extensional viscosity in turbulent flows is the principal instrument in drag reduction, but did not find such a plain explanation satisfactory enough. Hinch therefore further studied the extended state of the coiled

molecules and considered four models. These models show the importance of the finite extensibility of the polymer chain and the variation of the friction coefficient with extension.

Hinch's first model considers the dependence of stretching by bulk flow on the distortion. Using these models Hinch concluded that the frictional grip of the flow increases with the distortion and that the particle spins with a sum of the full vorticity but only part of the straining motion. The second conclusion is less important in dilute solutions as the ones used in this study. The second model considers the effect of hydrodynamic stretching and finite extensibility. The polymer is therefore regarded as a flexible thread that straightens as tension snaps the thread straight. The third model states that small transverse distortions are caused by weak motions acting on a straight thread. These transverse distortions are described by a diffusion process in the deformation space.

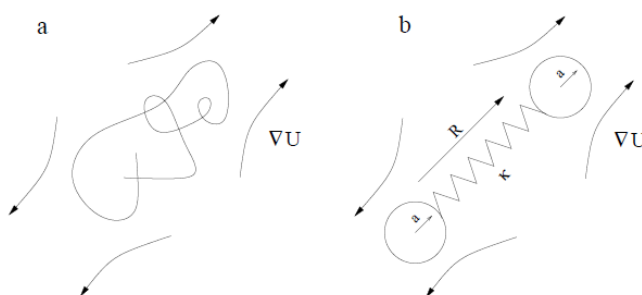


Figure 2-2: (a) A schematic drawing of a polymer being distorted by the flow. (b) The elastic dumb-bell model of a distorting polymer. (Hinch, E.J., 1977)

The fourth model describes the coiling of the polymer chain as an elastic rod. This model shows that the polymer can respond much slower or much faster than the relaxation time of the coiled polymer. If the flow is turbulent enough to create the large distortions of the random coil, the polymer seems to be fully extended. The polymer then responds very quickly and often almost as a rigid rod. If the polymer is not fully stretched then its response time is much longer than that of a random coil.

A different theory is proposed by De Gennes in 1986. His theory suggests that at each distance y from the wall, there is a cascade of turbulent eddies which are truncated elastically. This results in a law for minimum eddy size against the distance from the wall. The flexible coils behave elastically and therefore diminishing the cascade of turbulent eddies leading to less drag. De Gennes theory is therefore somewhat different than the viscous effect theory proposed by Lumley. Both theories do have in common that the additive enhances the buffer layer of the tube and that the additive interacts with the small turbulent structures and therefore changes the dissipation of turbulent energy. Another theory which attribute the DR of additives to the turbulent production is laid out by Landahl (1977). Landahl's theory is based on the coupled motion at two scales. The first scale is in the order of the boundary layer thickness. The second-scale is smaller and in the order of the viscous sublayer thickness. Based on Landahl's theory the phenomenon of turbulent drag reduction due to additives can be explained as being caused by the stabilization of the inflectional velocity profile in the small scale field due to the elongation of the added molecules.

Some of the arguments stated by the previous models can be used to explain all kinds of drag reduction by additives. Surfactant molecules consist of a hydrophilic and a hydrophobic part and tend to form aggregates, called micelles in water when above a certain concentration. Depending on the chemical structure of these surfactants and the dispersant used, the concentration and temperature, micelles can have different structures. Surfactants can only exhibit DR if the surfactant solution contains rod-like micelles. The diameter of such rod-like micelle is typically 2-4 nm and the length can vary between 25 and 250 nm (Gyr, A. and Bewersdorff, H.M., (1995)). Several hypothesis are proposed on the mechanisms of surfactant drag reduction. Many of them regard the rod-like micellar structures in surfactant solutions to have the same behavior as polymer molecules and therefore suggest that the same mechanisms that can be applied to polymers can also be applied on surfactant DRAs. Another explanation is that the micellar systems exhibit similarities with the DR fiber suspensions, as in these suspensions the alignment of the micellar structures in the flow direction also plays an important role. But this theory is incomplete since aligned particles can only weakly damp disturbances in flow direction, but strongly in the transverse direction.

2.2. Drag Reduction Using Polymers

Most of the standard DRAs are based on polymers. Polymers can be classified into two basic polymer types, namely synthetic polymers and biopolymers. Biopolymers have the advantage that they are environmentally acceptable and are less sensitive to mechanical degradation due to their more rigid molecular structure (Sorbie, K. S. (1991)). Addition of a few parts per million of a high molecular weight polymer can reduce the drag in pipe flow by up to 80% (i.e., increase the flow rate by a factor of five). Since Toms discovered this drag reducing property of polymers back in 1946 more than 7000 studies have been published on DR. The first commercial use of a polymeric DRA to increase the flow rate in crude oil pipelines began during 1979 in the Trans Alaska Pipeline System. Polymer concentrations from 5 to 25 ppm were used to increase the flowrate by up to 25% (Burger, E.D. et al. (1982)). Liaw et al., (1971) conducted experiments to observe how the molecular characteristics of polymers influence DR. They concluded that DR of polymer solutions depend on whether a critical concentration, i.e. the concentration at which DR starts to develop, is exceeded. A minimum chain size must be exceeded before significant DR occurs. Polymers differ in molecular size and weight and therefore the amount of DR will depend on the type of polymer. Depending on the type of polymer an optimum DR will occur at a certain concentration. At higher concentrations the viscosity enhancement of the polymer has a negative effect on the DR (Kim. N.J., et al., (2009), Virk, P.S., et al., (1967)).

2.2.1. The polymers used in this study

In this study xanthan and FLOPAAM EM 5205 (based on polyacrylamides), which are a biopolymer and a synthetic polymer respectively, are used as drag reducing agents. FLOPAAM EM 5205 is provided by the Shell lab as an emulsion polymer. An emulsion polymer is a colloidal dispersion of discrete polymer particles with a typical diameter of 0.01-1.0 microns in a medium such as water (Handbook of nonwovens, 2007). Xanthan is formed from the polymerization of saccharides. Wyatt et al. (2010) measured DR for xanthan for different concentrations in the range from 2% (20 ppm) to 35% (200ppm), and found out that xanthan is less susceptible to shear degradation compared to synthetic drag reducing polymers. Xanthan exhibits higher DR at temperatures in the range 50-60°C. This happens because xanthan molecules tend

to change their structure from aggregated helices to individual coils, leading to more favorable DR (Sohn, J.I. et al. (2000)). Various synthetic polymers have also been presented to reduce drag by 70-80% in an undisturbed pipeline at low concentrations. The synthetic polymer EM5205 is customized by the Shell lab to have excellent drag reducing abilities. This experiment will put the drag reducing abilities of this synthetic polymer to the test and compare it with xanthan.

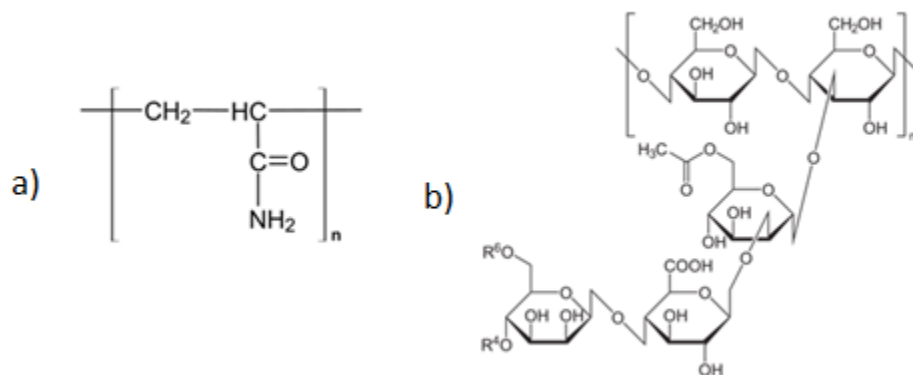


Figure 2-3: Schematic structure of the main part of the two polymers used in this study where, a) polyacrylamide and b) xanthan

2.3. Drag Reduction Using Surfactants

Usage of polymers is frequently limited to once-through systems because of permanent degradation. In circulating fluid systems, degradation of polymers causes rapid loss of DR. For these systems surfactants can be the solution. DR by aluminum disoaps in gasoline was first discovered and patented by Mysels in 1949. Aluminum disoaps form large aggregates that also degrade when subjected to high mechanical shear. With polymers this degradation is irreversible, whereas with aluminum disoaps it is reversible. The regeneration of the large aluminum disoap aggregates is a slow process which takes days to recover their drag reducing ability (Zakin, J.L. et al. (1998)). Recent studies have shown that environmentally acceptable surfactants can be used as an alternative to polymer for DRA applications (Hellsten, M. (2002)). For surfactants to be classified as a DRA, the surfactant need to form long rod-like micelles which have the ability to repair themselves in a time scale of seconds.

Surfactants can lower the surface tension between two fluids or between a fluid and a solid. Surfactant molecules have a hydrophilic head and a hydrophobic tail and can form aggregates, known as micelles. Surfactants can be classified into four classes of surfactants based on the composition of the hydrophilic head of the surfactant. The four classes of surfactants are known as:

- anionic: contain anionic functional groups (sulfate, sulfonate, phosphate and carboxylates)
- cationic: contain cationic functional groups at their head
- nonionic: contain covalently bonded hydrophilic groups containing oxygen that are bonded to hydrophobic groups.
- zwitterionic: contain both cationic and anionic centers attached to the same molecule.

For anionic surfactants high concentrations are required to observe DR. Furthermore, it is also reported that this class of surfactants interacts with ions like magnesium and calcium ions, cause precipitation and foam heavily (Zakin, J.L., et al. (1971)). Cationic surfactants encounter fewer problems and seem to be insensitive to ions present in water. Furthermore, cationic surfactants recover rapidly from shear but are not easily biodegraded making them not so environmentally acceptable (Chou, L.C. (1991), Singh, R.P. (2002)). Cationic surfactants do need counter ions or other additives to ensure drag reduction at low concentrations. The first additive to be used was 1-naphthol. Zakin et al., (1971) found out that 1500 ppm CTAB with equimolar 1-naphthol led to the highest critical shear stress (i.e., shear stress at which the surfactant loses its DR ability). Sodium salicylate is a counter ion that is the most widely used with cationic surfactants. Nonionic surfactants are more environmentally acceptable and are often more chemically stable (Zakin, J.L., et al. (1971)), but are not as effective as a drag reducer due to the narrow temperature range around the cloud point of the surfactant at which they are active (Hellsten, M., et al. (1994)). Zwitterionic surfactants have a wider temperature range for DR applications but are very sensitive to the ions present in water due to their cationic and anionic groups.

2.3.1. Micellar shapes

Micelles are formed when the concentration of the surfactant surpasses the critical micelle concentration (CMC). The shape of the micelles in a surfactant solution depends on besides the chemical structure of the surfactants also on the concentration and temperature as can be observed in Figure 2-4. Above the CMC the shape of a micelle is spherical or more ellipsoidal and as the concentration is further increased rod-like micelles will form. The surfactant is partially in crystal or gel form for temperatures lower than the Kraft point (Hunter, R.J., (2001). It can be observed that the CMC_I is almost independent of temperature, while the CMC_{II} (transition concentration from spherical micelles to rod-like or cylindrical micelles) increases with temperature. Micelles can form three different shapes (viz., monomers, spherical micelles and rod-like micelles). Tanford (1972) did some experiments on the size and shape of micelles in 1972 and proposed that the micellar shape is determined by the ratio of volume (V) of the hydrophobic group to the product of the length (l) of this group and the cross-sectional area (a) of the hydrophilic group. The packing parameter, V/la determines the shape of the micelles.

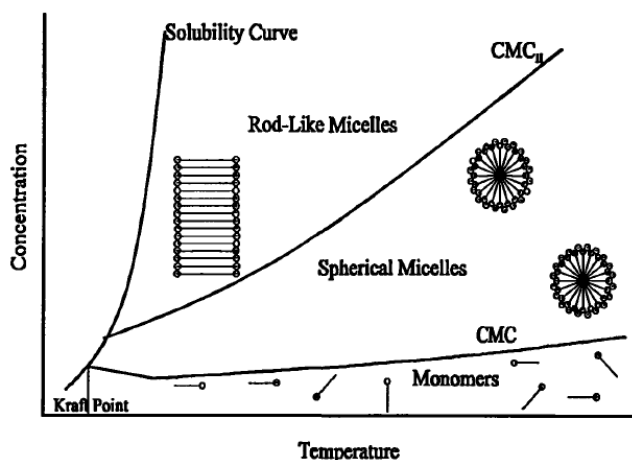


Figure 2-4: Schematic Phase diagram for surfactant solutions (Lu, B. (1997))

Table 2-1: Typical values for v/la and their corresponding micellar shapes (Zakin, J.L., et al., (1998))

Value of V/la	Shape of micelle
$\leq 1/3$	Spherical
$1/3 - 1/2$	Rod-like
$1/2 - 1$	Lamellar

In order to observe DR micelles should be rod-like and the value for the packing parameter should be between $1/3 - 1/2$. Addition of salts, co-surfactants or counter-ions can also induce the formation of rod-like micelles, by neutralizing or dispersing the electrostatic repulsion between the ionic head groups and therefore stabilize the micelle and stimulate formation of larger micelles. (Ohlendorf, D., (1986)).

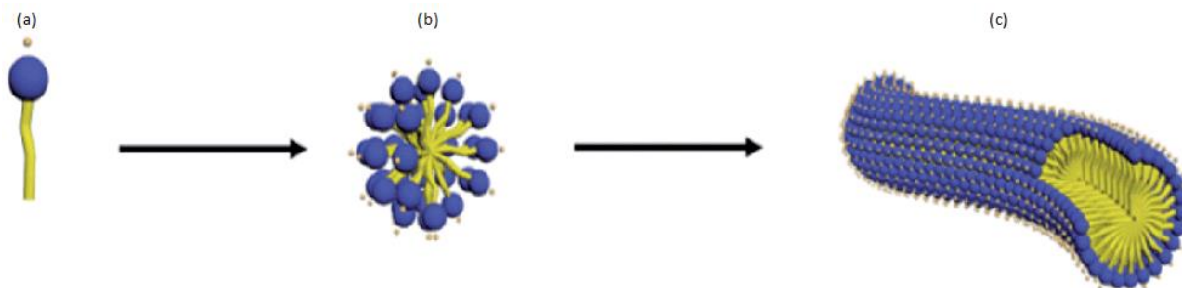


Figure 2-5: Transition from (a) monomers to (b) spherical micelles to (c) rod like micelle structures.

2.3.2. The surfactants used in this study

In this study an anionic surfactants, (i.e., Alpha-Olefin Sulfonate (AOS)), a nonionic surfactant, (i.e., Alkyl PolyGlucoside (APG)) and a cationic surfactant (i.e., hexadecylTrimethylAmmonium Bromide (CTAB)) are tested on their drag reducing properties. Chemical structures of these surfactants are shown in Figure 2-6. For these surfactants the goal is to observe a significant DR at low concentrations. Abed, M.A. et al., (2004) studied the micellization of alpha-olefin sulfonate in aqueous solutions in a concentration range of 0 to 100 mM. No sphere to cylinder transition in micellar structure was observed in the experimental concentration range and therefore also no DR is expected within this concentration range. Stradner, A., et al. (2000) showed that addition of a fatty alcohol to APG solutions has an enormous effect on the micellar size and shape, where the micelles grow controllably from short to giant and highly flexible micellar aggregates. Experiments conducted by Cai, S. (2014) proves that APG can be used as a drag reducer, but no exact values of DR are given. Drappier, J., et al. (2006) concluded that CTAB has significant drag reducing properties when combined with the counter-ion sodium salicylate (up to 80% at 10000ppm).

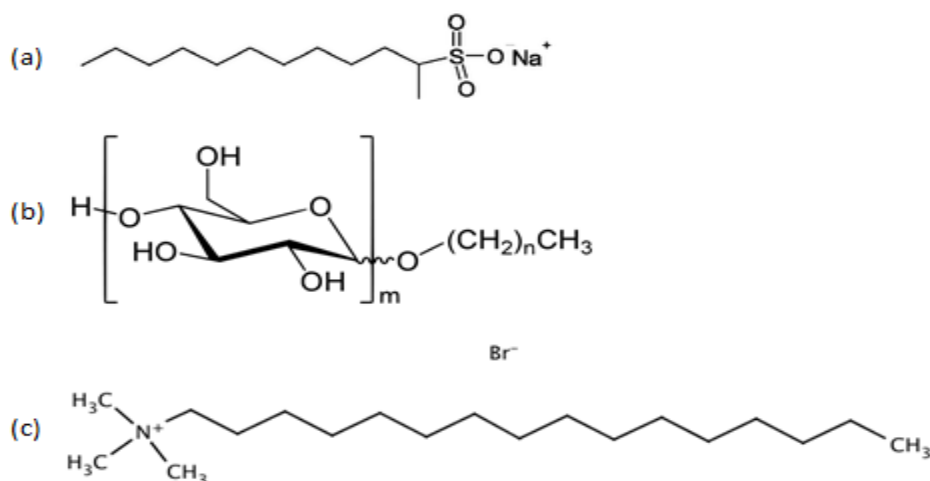


Figure 2-6: Schematic structure of the different kind of surfactants where, a) AOS, b) APG and c) CTAB

2.4. Turbulent and Laminar Pipe Flow

For an inclined pipe with constant cross sectional area and a known temperature profile along the pipe, the following mass balance equation can be obtained:

mass rate in – mass rate out = mass accumulated per unit time

$$A\rho v - A\left(\rho + \frac{\partial\rho}{\partial s} ds\right)\left(v + \frac{\partial v}{\partial s} ds\right) = A \frac{\partial\rho}{\partial t} ds, \quad (2-1)$$

where, A is the cross sectional area of the pipe in m^2 , ρ is the fluid density in kg/m^3 , v is the fluid velocity in m/s , s is the coordinate along the pipe in m and t is the time in s . The momentum balance per unit time can be written as:

momentum rate in – momentum rate out + pressure forces + gravity force + friction force = momentum accumulated per unit time

$$A\rho v^2 - A\left(\rho + \frac{\partial\rho}{\partial s} ds\right)\left(v + \frac{\partial v}{\partial s} ds\right)^2 + Ap - A\left(p + \frac{\partial p}{\partial s} ds\right) + F_g(\rho, s)ds + F_f(\rho, \mu, v)ds = A \frac{\partial(\rho v)}{\partial t} ds, \quad (2-2)$$

where, p is the pressure in Pa , $F_g(\rho, s)ds$ is the gravity force per unit length in N/m . $F_f(\rho, \mu, s)$ is the friction force per unit length in N/m and μ is the dynamic viscosity in $Pa \cdot s$. Equation (2-2) can be simplified into:

$$\begin{aligned} \frac{\partial(\rho v)}{\partial s} &= -\frac{\partial\rho}{\partial t}, \\ \frac{\partial(\rho v^2)}{\partial s} &= -\frac{\partial(\rho v)}{\partial t} - \frac{\partial p}{\partial s} + \frac{F_g}{A} + \frac{F_f}{A}. \end{aligned} \quad (2-3)$$

Under steady-state flow conditions equations (2-3) results in:

$$\begin{aligned} \frac{\partial(\rho v)}{\partial s} &= 0, \\ \frac{\partial(\rho v^2)}{\partial s} &= -\frac{\partial p}{\partial s} + \frac{F_g}{A} + \frac{F_f}{A}. \end{aligned} \quad (2-4)$$

The pipe used in this experiment is placed horizontally so F_g can be neglected as no change in pressure is caused by the change in the pipe's elevation.

Furthermore in equation (2-4), the term $\frac{\partial(\rho v^2)}{\partial s}$ can be written as: $\frac{\partial(\rho v^2)}{\partial s} = \frac{\partial(\rho v)}{\partial s} v + \rho v \frac{\partial v}{\partial s}$. Rearranging equation (2-4) results in the following steady-state expression for the pressure drop per unit length:

$$\frac{dp}{ds} = -\frac{\rho f v^2}{2D} - \rho v \frac{dv}{ds}, \quad (2-5)$$

where,

$\rho v \frac{dv}{ds}$ is the acceleration loss caused by a change in momentum when the fluid is accelerated due to expansion. This term is significant for gas flow. In this experiment this effect can be neglected.

$\frac{fv^2}{2D}$ is known as the friction loss caused by the dissipation of energy by viscous forces in the fluid and is strongly dependent on the fluid properties, velocity and flow regime.

f is the dimensionless Moody friction factor (Moody, L.F., (1944)), and D is the pipe diameter in m . The friction factor f is a function of the dimensionless Reynolds number and the absolute pipe roughness ϵ , which are defined as:

$$N_{Re} = \frac{\rho D v}{\mu} = \frac{4 \rho Q}{\pi \mu D}, \quad (2-6)$$

$$\epsilon = \frac{e}{D}, \quad (2-7)$$

where, Q is flowrate in m^3/s and e is the pipe roughness in m . Some DRA show significant DR at low concentrations such that the deviations in the shear viscosity compared to the shear viscosity of the solvent are negligible. If the deviations in shear viscosity are not negligible, the solvent physical properties are used to calculate the Reynolds number and friction factor. Admittedly this is a simplification, but it grasps the essence of DR using additives.

There are two main types of flow, namely laminar and turbulent flow. These types of flow occur depending on the velocity of the flow, the viscosity of the fluid and the roughness of the layer above which it flows. In laminar flows all molecules in a fluid flow parallel to each other in the direction of transport. Laminar flow can be visualized as a series of parallel streamlines. For laminar flow, where the Reynolds number is lower than 2000. The friction factor can be defined as:

$$f = \frac{64}{N_{Re}}. \quad (2-8)$$

When the flow velocity increases or the viscosity decreases, fluid transport perpendicular to the main flow direction occurs, characterizing turbulent flow. The streamlines in a turbulent flow move in a complex random manner called turbulent Eddies. The difference in streamlines and velocity profile of a laminar and turbulent flow is illustrated in Figure 2-7.

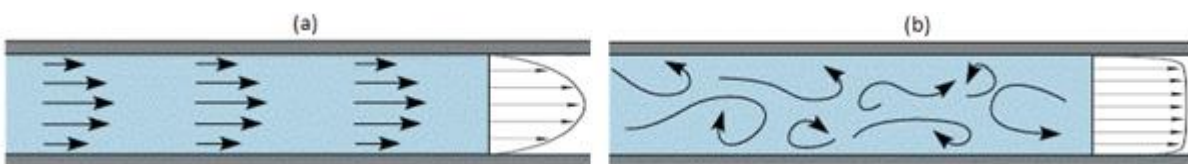


Figure 2-7: Stream line and velocity profile of (a) laminar flow and (b) turbulent flow

For turbulent flows where the Reynolds number is higher as 3000, various implicit and explicit approximations are available for the friction factor. One of the implicit approximations for f is given by the Colebrook (1939) equation:

$$\frac{1}{\sqrt{f}} = -1.74 + 2 \log_{10} \left(2\epsilon + \frac{18.7}{N_{Re}\sqrt{f}} \right). \quad (2-9)$$

One of the explicit approximations for f is the equation of Zigrang and Sylvester (1985).

$$f = \left(-2 \log_{10} \left(\frac{2\epsilon}{3.7} - \frac{5.02}{N_{Re}} \log_{10} \left(\frac{2\epsilon}{3.7} + \frac{13}{N_{Re}} \right) \right) \right)^{-2}. \quad (2-10)$$

Note: throughout this report the Moody friction factor is used, which is a factor 4 times larger than the Fanning friction factor.

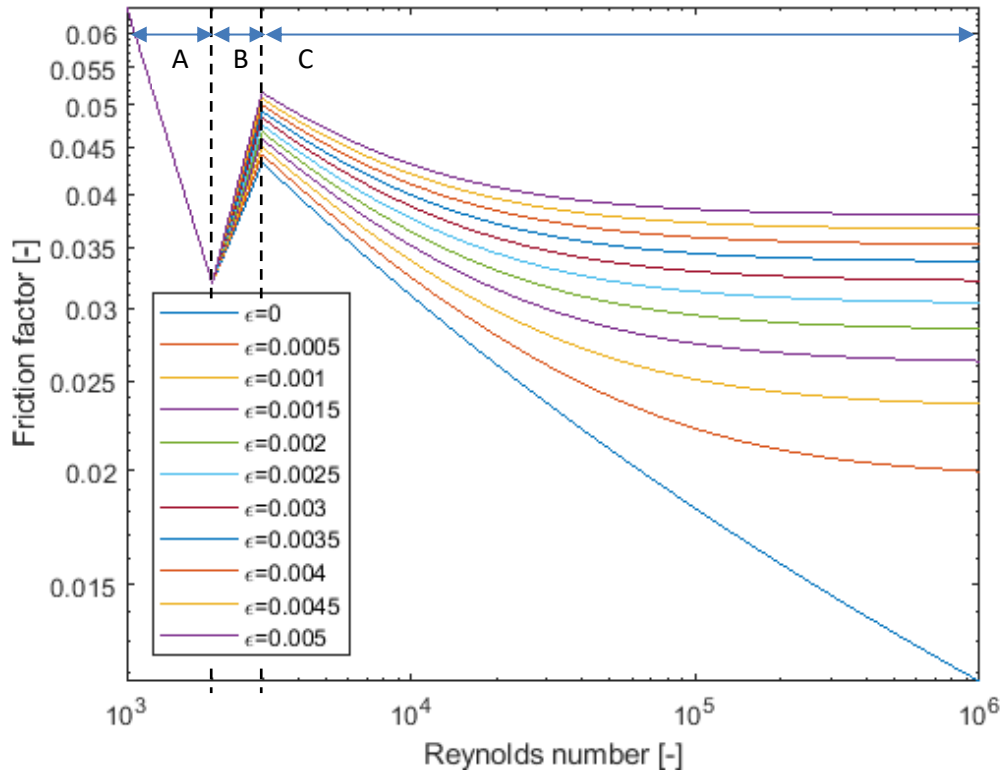


Figure 2-8: Friction factor as function of Reynolds number for different values of dimensionless roughness ϵ . The graph is split into three parts depicting three flow regimes, viz., A= laminar-, B= transitional- and C= turbulent flow regime.

Addition of minute amounts of the DRA to a turbulent system will lead to a decrease of the friction factor, thus decreasing the pressure drop necessary to achieve the same flow rate, or increase the flowrate at a certain fixed pressure drop. In pipe flow usage of a DRA will decrease the pressure drop necessary for achieving a certain flow rate. For a given flow rate, percentage of drag reduction (DR) can be defined as (Li, P.W., et al., (2000)):

$$\%DR = \frac{\Delta p - \Delta p_{DRA}}{\Delta p} * 100, \quad (2-11)$$

where, Δp is the pressure drop measured without DRA and Δp_{DRA} is the pressure drop measured with DRA.

2.5. Degradation of DRAs

Polymers and surfactants tend to degrade in high shear rate constrictions. Surfactant degradation is a reversible process whereas polymer degradation is an irreversible process. This can eventually reduce polymer usability as a DRA. The polymers are being stretched due to the flow field as discussed in chapter 2.1.1. This stretching of the polymer chains can lead to chain rupture and as a consequence reduce the DR of the polymer. Odell and Keller (1986) found out that when a polymer chain is stretched the stress distribution is parabolic with a maximum stress at the center of the polymer chain. The force F exerted at the center of the chain is proportional to:

$$F \propto \eta \dot{\epsilon} l^2, \quad (2-12)$$

where, η is the viscosity of the solvent, $\dot{\epsilon}$ is the extensional rate and l is the chain length. This equation shows that the force at the center of the chain increases as the chain length increases. It is therefore expected that the polymer chains scission at their center when the strain rate on the molecule is sufficient enough. The fracture strain rate scales according to:

$$\dot{\epsilon} = 1/l^2 \approx 1/M_w^2, \quad (2-13)$$

where, M_w depicts the molecular weight of the polymer chain. This scaling is confirmed in flows where the residence time was high enough for chains to completely extend (Odell, J.A. and Keller, A., (1986)). The elongation flow field is not uniform and chain scission therefore occurs depending on the position of the chain in the flow field. In closed loop flows at each passage there is a probability of the chains to be broken. Chain scission will be highest in the first passage and will decrease as the flow loops until a steady state occurs where all the chains are broken and that the chains cannot be degraded by the flow field anymore. A way of monitoring this degradation can therefore be useful. The Mark-Houwink equation gives a relation between intrinsic viscosity and molecular weight.

$$[\eta] = KM_w^\alpha, \quad (2-14)$$

where, η is the intrinsic viscosity of the polymer, M_w is the molecular weight and K and α are Mark-Houwink parameters. As the chain scissions the molecular weight of the chains decrease and therefore affect the viscosity. Biopolymers experience next to mechanical shear degradation also biological degradation by all kinds of bacteria that cut the polymeric chains into smaller pieces. When polymers degrade their molecular weight decreases and therefore also the viscosity. The change in viscosity can therefore be a measure of polymer degradation. A bulk acoustic wave viscosity sensor is placed in-line to observe this change in viscosity and therefore degradation.

2.6. Viscosity sensor

SenGenuity's ViSmart® VS2610 viscosity sensor can take measurements while the fluid is in motion and can therefore be connected in-line to the flow loop. Using this sensor makes it possible to monitor the relative viscosity in real-time and therefore visualize degradation. This sensor provides real-time viscosity and temperature measurements in an operating temperature range of -15°C to +105°C. This sensor has no moving parts and is based on Bulk Acoustic Wave (BAW) technology. The top of the sensor which is in contact with the fluid contains a piezoelectric sensing element that gets excited by a high frequency oscillator. This oscillator operates in the Thickness Shear Mode (TSM) of vibrations in which the shear displacement occurs on the crystal faces in the plane of the crystal plate. Displacement occurs along the thickness of the plate and is maximum at the surfaces, as depicted in Figure 2-9. When a fluid is covering the surface of this sensor this fluid will couple to the sensors vibrating surface. The viscosity of the fluid will determine the amount of damping of the sensor and therefore a decrease in the BAW oscillator's frequency. The viscosity is thereby back correlated using the measured BAW electrical parameters to the Acoustic Viscosity (AV) of the fluid. When assuming a constant density, the AV and dynamic viscosity have the following relationship:

$$AV = \mu * \rho . \quad (2-15)$$

The sensor is placed in-line with the flow loop. The sensors position in which it is placed connected to the flow loop and the way it interacts with the fluid is very crucial. Section 3 will discuss the placement of the sensor and the pros and cons of that way of placement in further detail.

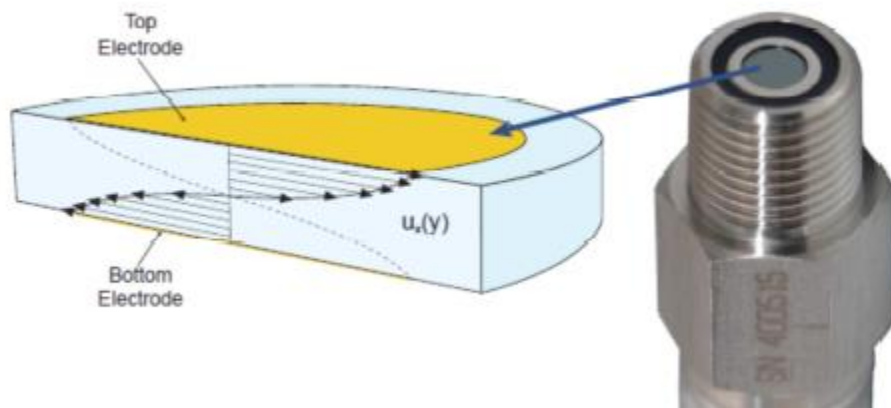


Figure 2-9: Sensor surface showing the TSM of vibration

3. Experiments

This chapter discusses the experimental procedures and set-ups used. Firstly the brine composition and preparation of the possible DRAs solutions are discussed. The experiment is divided into two phases. The first phase consists of building a flow loop capable of achieving turbulent flow. Also in the first phase of the experiment we screen the surfactant solutions based on their micelle shape. Once the behavior of the polymer and surfactant solutions in the flow loop is well understood and an appropriate concentration at which significant drag reduction occurs can be identified, we initialize phase 2 of the experiment and replace the test tube with a similar test tube but which has multiple pressure gauges along the tube. This is done to localize the pressure drop and see how the DRAs affect this pressure drop. The second phase of the experiment also consist of monitoring the degradation of the DRAs. For this we add the viscosity sensor is also connected to the flow loop.

3.1. Materials and Methods

The additives are dissolved in brine with a specific composition, mimicking sea water. The polymeric and surfactants are prepared in a certain manner as will be discussed here.

3.1.1. Brine composition

In order to assess the solutions on their DR in petroleum application all additives are dissolved in brine. The brine has a composition that resembles seawater. The composition of the brine is given in Table 3-1. The brine is made in batches of one or two liters. In order to prevent any precipitation we add the salts in the order as stated in Table 3-1. A simple geochemical simulation using PHREEQC is used to analyze equilibrium composition and see if unwanted compounds will form when making this brine. From this simulation it turns out that no significant formation of disturbing chemicals is formed. PHREEQC also calculates the density of the brine, which was $\sim 1.03 \text{ g/cm}^3$ at 25°C . This result was consistent with the density calculated using traditional methods (weigh and measure).

Table 3-1: Brine composition (Synthetic Seawater)

Total Salt Concentration		33123 [mg/L]	
Concentration of Cations [mg/L]		Weight of Salts for 1L of brine [g]	
Na^+	10182	1. $\text{CaCl}_2 \cdot 2\text{H}_2\text{O}$	1.4
K^+	371	2. $\text{MgCl}_2 \cdot 6\text{H}_2\text{O}$	10.3
Ca^{2+}	389	3. $\text{Na}_2\text{SO}_4 \cdot 10\text{H}_2\text{O}$	8.3
Mg^{2+}	1227	4. KCl	0.7
Concentration of Anions [mg/L]		5. NaCl	22.9
SO_4^{2-}	2478		
Cl^-	18476		

3.1.2. Solution preparations

The polymers and surfactants are all dissolved in brine with a composition as stated in Table 3-1. In order to make the brine a bottle is cleaned thoroughly with acetone, methanol and water. After the bottle is dried a magnetic stirrer is put in the bottle and both are weighed. 1L of demi-water is measured with a flask and poured into the bottle. The bottle is stirred using a magnetic stirrer and the salts are gently added in the order displayed in Table 3-1. The next salt is only added when the previous salt is completely dissolved. After addition of the last salt, the brine is degassed until no visible gas bubbles are observed. After this the brine is ready for addition of the DRA.

3.1.2.1. Polymers

Two types of polymers are used as DRA. Xanthan gum (Fluka/Sigma-Aldrich, France) was used in powder form and the correct weight is dissolved in demi-water to obtain the needed 1000 ppm concentration. Upon addition of the xanthan to the brine the brine is stirred using a magnetic stirrer. A vortex is created in the brine and xanthan is added gently so that no lumps are forming. The 1000 ppm solution can afterwards be further diluted to obtain solutions with the preferred concentrations.

Preparation of the emulsion polymer solutions is done by first making a mother solution with a 10.000 ppm active polymer solution. The polymer emulsion contains 30% by weight of active anionic polyacrylamide. The sample which contains the emulsion polymer is vigorously shaken prior to use. First 150 g of brine is poured into a 600 mL beaker. A magnetic stirrer is added to the beaker and the beaker is stirred at ~500 rpm. After this a syringe is filled with 6.66 g of emulsion polymer and the weight of the filled syringe is recorded (WF). After this the content of the syringe is rapidly dispersed into the vortex of the 600 mL beaker and the time is recorded. The empty syringe is weighed and the weight is recorded (WE). The amount of added polymer emulsion is therefore $W = WF - WE$. The beaker is afterwards filled with the following amount of brine (Q_w): $Q_w = W * CE - (150 + W)$, where CE is the activity of emulsion polymer in % (30% by weight for this emulsion polymer). The solution is left being stirred for a total of 30 minutes. After this the 10.000 ppm solution is ready and can be further diluted to obtain the preferred concentrations.

3.1.2.2. Surfactants

As a surfactant AOS, APG and CTAB are used. The AOS used is commercially known as BIO-TERGE® AS-40 and provided by Stepan®. The activity of the AOS used is 39%. The commercial name of the APG used is TRITON™ CG-650 and is provided by DOW® Chemicals. The activity of the APG used is 50%. The CTAB used was a powder bought from Alfa Aesar and has an activity of 98%. The amount of surfactant (w_{surf}) for a specific surfactant concentration knowing the amount of brine (w_{brine}) for a total weight (w_t) are calculated using:

$$w_t = w_{surf} + w_{brine} , \quad (3-1)$$

$$w_{surf} = \frac{w_{tot} - w_{brine}}{CE_{surf}} * 100 , \quad (3-2)$$

where, CE_{surf} is the activity of the surfactant in percentage.

3.2. Experimental Set-up

The building of the experiment is split up into two phases. The first phase consists of building a flow loop capable of achieving turbulent flow. The set-up is validated that it can achieve turbulent flows by performing pressure drop measurements along a single segment test tube. Furthermore, the surfactants are screened based on their micellar shape and their DR property is tested using the set-up. For the second phase the test tube is swapped for a test tube with multiple pressure gauges along the tube. Furthermore, the viscosity sensor is connected to the flow loop to monitor the degradation.

3.2.1. Phase 1: Pressure Drop measurements and DRA screening

In phase 1 a flow loop capable of achieving turbulent flow is built. The DRAs are also tested on their drag reducing abilities using this set up. Furthermore, the surfactant solutions are screened using a tensiometer and a Dynamic Light Scattering (DLS) device. The tensiometer is used for obtaining the CMC and DLS device is used to measure the size of the micelles.

3.2.1.1. *Experimental Set-up phase 1*

The set-up for phase 1 of the experiment is comprised of a Quizix QX1500 precision pump, two pressure gauges, a coiled test tube, a reservoir that is continuously magnetically stirred, a data acquisition box and a computer. The way in which these components are connected to each other is shown in Figure 3-1. The QX1500 precision pump can operate at pressures below the maximum allowed value of 103 bar and maximum flow rate of 200 ml/minute. A 150 bar pressure gauge is put at the entrance of the test tube and a 60 bar pressure gauge is put at the exit of the test tube. The coiled test tube is stretched out 1.48m long with an inner diameter of 0.5mm and a coil diameter of 12.5 cm. The pressure gauges are connected to a data acquisition box, and from that box the data is visualized on the computer. Before the fluids enter the test tube they pass a T fitting. When this fitting is switched the flow loop is disconnected and the fluids flow to the effluent bottle. This is done in order to flush and therefore clean the cylinders of the pump. The outflow line back to the reservoir is flexible (dashed line in Figure 3-1) so that it can be moved to let flow go to the effluent bottle instead of going back to the reservoir. In this way the all the lines used in the flow loop can be flushed and therefore cleaned. Flushing and cleaning the cylinders of the pump and the flow lines is done every time a different solution is introduced into the flow loop.

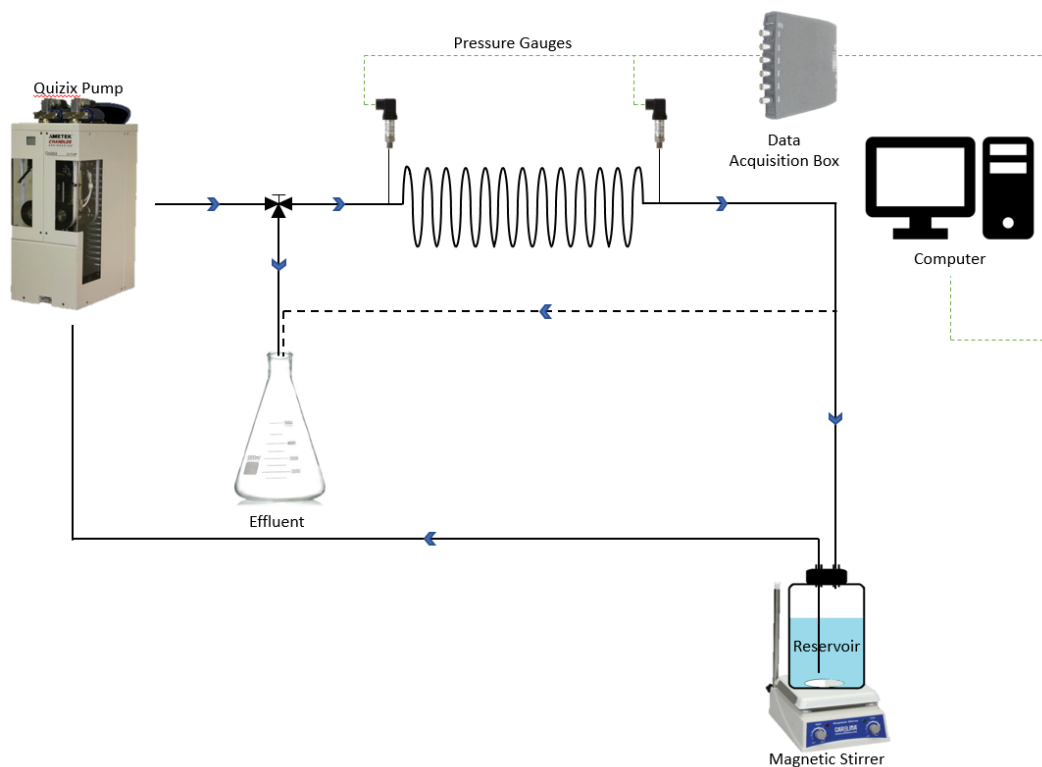


Figure 3-1: Schematic view of the phase 1 of the experiments

3.2.1.2. *Optimal conditions for drag reducing surfactants*

For surfactants to have DR abilities and to be classified as DRA, the surfactant solution need to have micellar structures which can interact with the turbulent flow. The surfactants tested for DR are first screened by measuring the CMC. The CMC is derived by measuring the surface tension of the various solutions at different concentrations. The surface tension (γ) is measured using a Kibron EZ-Pi + tensiometer with a measuring range of 0-300mN/m and a resolution of 0.01mN/m.



Figure 3-2: Kibron tensiometer used to measure the surface tension

Surface tension measurements are obtained by pulling a rod out of the sample using the Du Noüy-Padday method (Padday et al., (1975)) as is sketched in Figure 3-3. More information on how the surface tension is derived by measuring the maximum pull on a rod can be obtained in the article of Padday et al., (1975).



Figure 3-3: Du Noüy-Padday method for measuring the surface tension

The surface tension can be influenced by the composition of the brine. The CMC of a surfactant is therefore also dependent on the composition of the brine. The CMC can be obtained by plotting the log of the concentrations against the surface tension. The intersection of the two straight lines through the data points resembles the CMC as shown in Figure 3-4. This visual data analysis is highly subjective and can lead to very different CMC values depending on quality of the data and the chosen interval around the CMC.

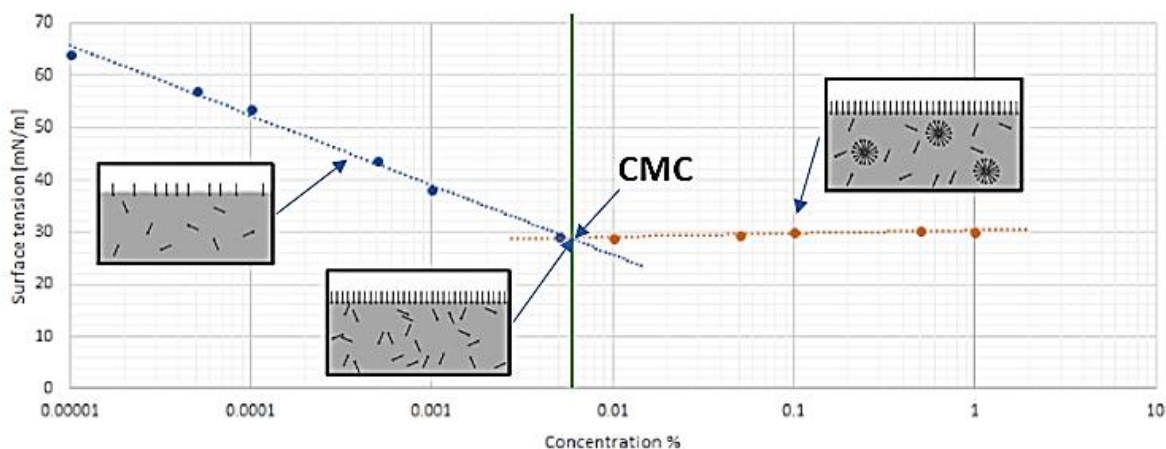


Figure 3-4: Concentration against the measured surface tension for a surfactant.

The micellar shape of the surfactants was discussed in Chapter 2.3.1. Figure 2-4 shows that the shape of a micelle can change to a more rod like structure when the concentration is increased. To observe this transition in micelle shape we use DLS to obtain size measurement of the samples at various concentrations. A DLS device illuminates the particles in the sample with a laser and analyzes the intensity fluctuations in the scattered light (Berne, B.J. and Pecora, R., (2000)). This gives a measure of the Brownian motion of a particle and from this, one can relate the size of that particle. Brownian motion is the movement of particles in a fluid due to the collision with



Figure 3-5: Malvern Zetasizer Nano ZS

the molecules of that fluid. A particle moving quickly will be smaller than a particle which moves more slowly. Based on the Stokes-Einstein equation the relationship of particle size and speed due to Brownian motion is defined. The DLS device used in this study is the Malvern Zetasizer Nano ZS. The Zetasizer measures the fluctuation in scattering intensity and creates a correlation function. Based on the shape of this correlation function the Zetasizer uses algorithms to extract the decay rates for a number of size classes to produce a size distribution. The Zetasizer Nano ZS main components are shown in Figure 3-6. It can be noted that the detector which detects the scattered light is placed close to 180° . This way of scatter detection is called backscatter detection. Backscatter detection has the advantage that the laser beam does not have to travel through the entire sample reducing the effect of multiple scattering, where already scattered light gets further scattered by other particles. Another advantage is that the effect of dust is significantly reduced using backscatter.

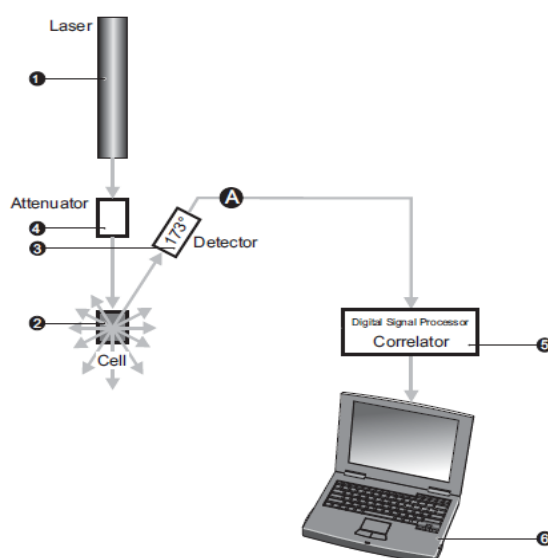


Figure 3-6: Schematic view of the main components in a DLS device

3.2.2. Phase 2: Rheology, pressure drop localization and degradation

In phase 2 of the experiment all the solutions that have been tested on the flow loop in phase one are also tested as to their rheological properties. The set-up for phase 2 of the experiment consist of the same components as phase 1 with the difference that the test tube is switched over to another tube that contains 4 extra pressure gauges. Furthermore is the viscosity sensor connected in-line with the flow loop.

3.2.2.1. Rheology

Rheology is the study of flow of matter. In this study the shear rate against the viscosity is measured using the Anton Paar MCR302 rheometer. This rheometer is used in combination with a concentric cylinder and a measuring cup. There should be enough fluid sample in the measuring cup so that the concentric cylinder is completely immersed. The rheometer used in this study is shown in Figure 3-7. Figure 3-8 shows a schematic drawing of the concentric cylinder and the measuring cup.



Figure 3-7: The Anton Paar MCR302 rheometer used for the rheology study

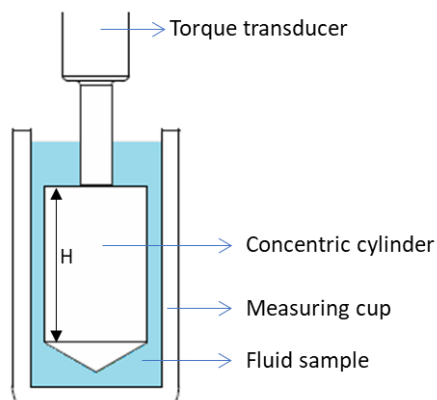


Figure 3-8: Schematic view of the concentric cylinder system filling

In this set-up the concentric cylinder moves while the measuring cup stand still. This results in a type of flow in the fluid sample which is called Couette flow. The inner cylinder is set to rotate with a constant angular velocity ω_0 , while the torque required to keep the cylinder in motion is recorded. The shear rate $\dot{\gamma}$ for a stationary flow with an angular velocity ω_0 is given by

$$\dot{\gamma} = \frac{r_2 \omega_0}{r_2 - r_1}, \quad (3-3)$$

where, r_1 and r_2 are the radii of the two cylinders as drawn in Figure 3-9. The torque M of the inner cylinder is measured by the rheometer. From this measured torque one can calculate the shear stress, τ using

$$\tau = \frac{M}{2 \pi r_2^2 H}, \quad (3-4)$$

where, H is the height of the rotating cylinder. The shear viscosity, η can therefore be found using

$$\eta = \frac{M(r_2 - r_1)}{2 \pi r_2^3 \omega_0 H}. \quad (3-5)$$

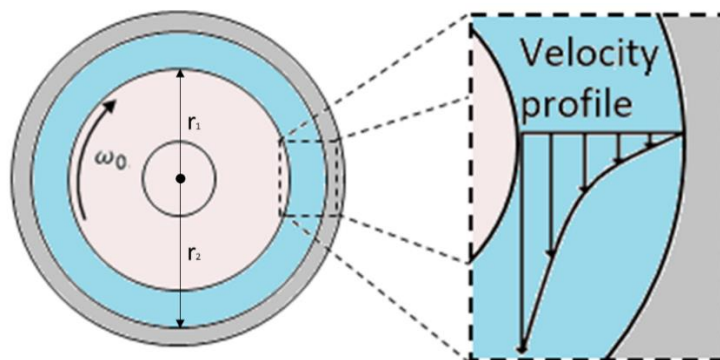


Figure 3-9: Top view of the concentric set-up with coquette flow.

3.2.2.2. *Experimental set-up phase 2*

The set-up shown in Figure 3-1 undergoes some changes in phase 2 of the experiment. Firstly, a second test tube is taken with an identical inner diameter as in phase 1 and switched with the first test tube. This test tube is divided into 5 sections with a total length of 1.5m. There are three sections of 40 cm, one section of 20 cm and one of 10 cm. The sections are connected in the order of smallest first, so the section of 10cm is closest to the inlet followed by the 20 cm section and the three 40 cm sections. The sections are connected using tee (T) pieces that have the same diameter as the test tube. The third opening of the tee (T) piece is connected to the pressure gauge. A 150 bar pressure gauge is placed at the inlet followed by two 100 bar pressure gauges and those are on their turn followed by three 60 bar pressure gauges. The experimental set-up in this phase has also the BAW viscosity sensor placed in-line. This sensor is connected to the flow set up using a Swagelock tee (T) fitting. Figure 3-10 shows how all these components are connected. The dashed line in this figure has the same function as in phase 1, namely to open up the possibility to flush and therefore clean the flow loop.

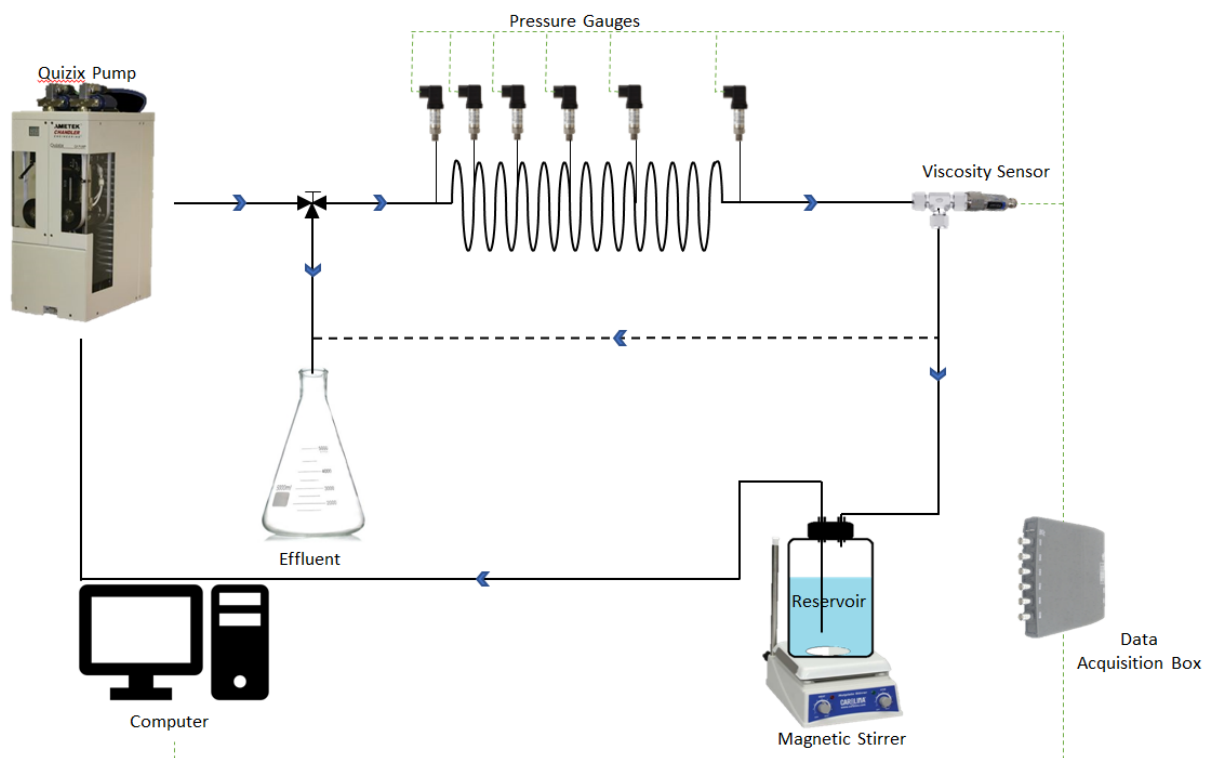


Figure 3-10: Schematic view of phase 2 of the experiment

3.2.2.3. Pressure drop localization

The test tube is in this experiment split up into 5 sections with a total length of 1.5 m. This is done in order to localize how the pressure drops along the test tube and how the DRAs affect this pressure drop. A high pressure is expected at the when the pump is set to its maximum. Therefore, a pressure gauge of 150 bar is placed at the entrance of the test tube. Figure 3-11 shows how the pressure gauges are placed using this test tube.

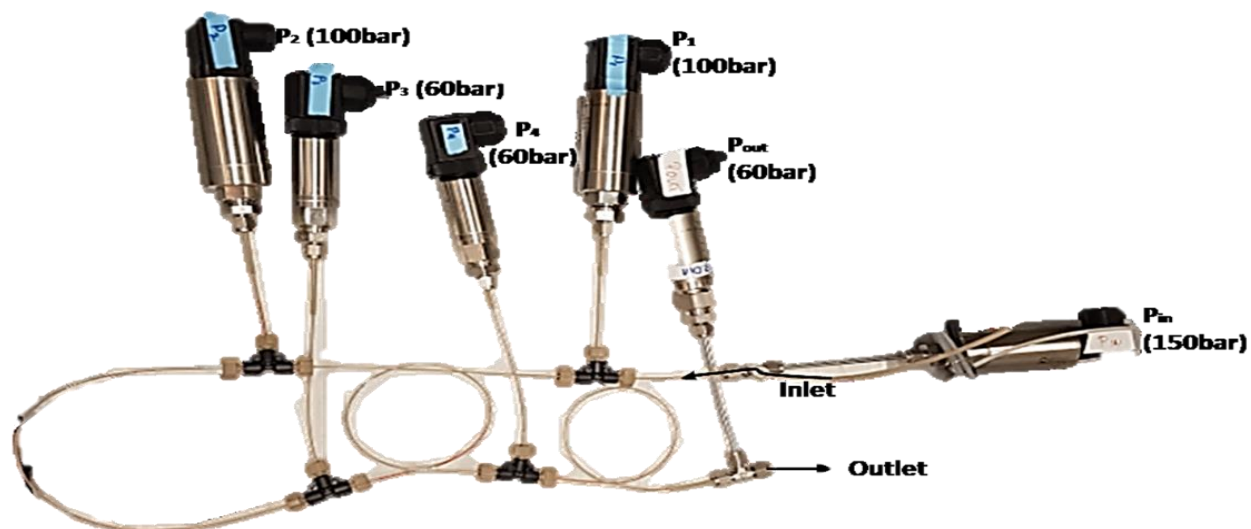


Figure 3-11: Test tube used for the pressure drop localization

3.2.2.4. Degradation

The set-up is built so that the fluids return to the reservoir. This looped flow makes it possible to run the experiment for a long time without the need of creating any new solutions. In chapter 2.5 it is discussed how degradation can be linked to viscosity using the Mark-Houwink equation. As the solutions are being sheared and degraded by the pump and the contractions and elbows present in the flow loop the viscosity should be affected and therefore the solutions viscosity will decrease. With the in-line viscosity sensor, it is possible to see any degradation as a decrease in viscosity measured by the sensor over time. The sensor is connected to the flow loop by using a Swagelok tee (T) fitting as shown in Figure 3-12. This way of connecting the sensor to the flow loop is not ideal as there might be a dead volume in front of the sensor face, leading to the sensor to measure the same fluid over and over again. In this experiment, quite high velocities are used from which the assumption is drawn that at these high velocities the effect of having a dead volume in front of the sensor would be minimalized. Furthermore, the BAW viscosity sensor has a read out in Acoustic Viscosity. This needs to be calibrated to know what actual viscosity is linked with it. For non-Newtonian fluids it is also necessary to know at what shear rate the sensor operates.

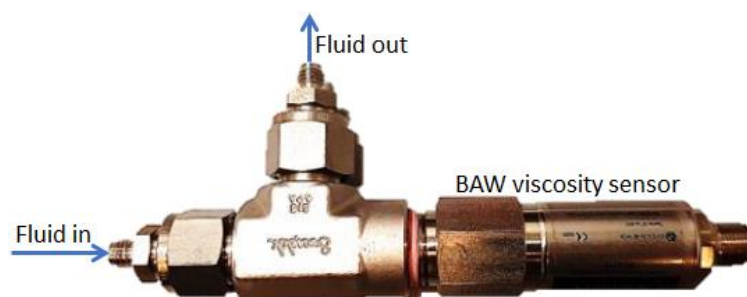


Figure 3-12: Tee (T) fitting connection for the in-line BAW viscosity sensor

4. Numerical Model

One of the most common models used in computational fluid dynamics to simulate turbulent flow is the $k - \epsilon$ model. This model is a two-equation model where in addition to the mass conservation law and the momentum balance equation, two partial differential transport equations are solved, namely the kinetic energy (k) and the rate of dissipation of turbulent energy (ϵ). The $k - \epsilon$ model has a good convergence rate and relatively low memory requirements making it a popular model for industrial applications. Compared to other models the $k - \epsilon$ model is less nonlinear making it easier to converge without providing a good initial guess. This chapter will discuss the numerical model used in this study as a comparison to the experimental results.

4.1. Laminar flow

For laminar flow the fluid flow is predicted by solving the Navier-Stokes equations. The Navier-Stokes equations are based on Newton's second law of motion for fluids. For a compressible Newtonian fluid representing the conservation of momentum this yields

$$\rho \left(\frac{\partial \mathbf{u}}{\partial t} + (\mathbf{u} \cdot \nabla) \mathbf{u} \right) = -\nabla p + \left(\mu \Delta \mathbf{u} + \left(\zeta + \frac{1}{3} \mu \right) \nabla(\nabla \cdot \mathbf{u}) \right) + \mathbf{F} , \quad (4-1)$$

where, \mathbf{u} is the fluid velocity (vector), p is the fluid pressure, ρ is the fluid density, μ is the dynamic viscosity and ζ is the second viscosity (resisting volume change) of the fluid. Equation (4-1) consists of four parts. The first part, corresponding to the terms on the left relate to inertial forces, the second part (first term on the right) corresponds to pressure forces, the third part (second part on the right) corresponds to viscous forces and the fourth and last part corresponds the external forces applied on the fluid. Equation (4-1) is always solved with the conservation of mass equation which yields:

$$\frac{\partial \rho}{\partial t} + \nabla \cdot (\rho \mathbf{u}) = 0 . \quad (4-2)$$

Mach numbers is the ratio for the fluid velocity to the local speed of sound in that medium. $M_{Nr} = |\mathbf{u}|/c$, where, c is the velocity of sound through that medium. In our experiment we deal with low Mach numbers for which the fluid can be considered as incompressible. For incompressible flow equation (4-2) becomes $\nabla \cdot \mathbf{u} = 0$. This makes the last part of the viscous term in the conservation of momentum equation $\left(\left(\zeta + \frac{1}{3} \mu \right) \nabla(\nabla \cdot \mathbf{u}) \right)$ zero for incompressible flows.

4.2. Turbulent flow

For flows where the Reynolds trespasses a critical value, perturbations are no longer damped out, and the flow becomes turbulent. When the flow becomes turbulent, usually the averaged equation is used. So we write all dependent variables as a sum of an averaged part and a fluctuating part, e.g., $\mathbf{u} = \bar{\mathbf{u}} + \mathbf{u}'$. After averaging all fluctuating parts become zero, because the average fluctuation is zero, except the term $\overline{((\bar{\mathbf{u}} + \mathbf{u}') \cdot \nabla)(\bar{\mathbf{u}} + \mathbf{u}')} = (\bar{\mathbf{u}} \cdot \nabla) \bar{\mathbf{u}} + \overline{(\mathbf{u}' \cdot \nabla) \mathbf{u}'}$. The term $\overline{(\mathbf{u}' \cdot \nabla) \mathbf{u}'}$ is the Reynolds stress. Turbulent flows are characterized by small scale fluctuations, which are impossible to solve even with present-day

computers or even present-day supercomputers. We can solve the averaged equations, but this requires closure equations, which can be found for instance if we use a $k - \epsilon$ model.

4.2.1. The $k - \epsilon$ model

The equations solved by the turbulent flow, $k - \epsilon$ model are the Navier-Stokes equations for conservation of momentum and the continuity equation for conservation of mass. Turbulence effects are modeled using the standard two-equation $k - \epsilon$ model with realizability constraints. In the $k - \epsilon$ model it is assumed that the turbulent shear stress is related to the mean rate of strain due to a turbulent viscosity (Jones, W.P. and Launder, B.E. (1971)). For the turbulent kinetic energy k we obtain:

$$\rho(u \cdot \nabla)k = \nabla \cdot \left(\left(\mu + \frac{\mu_T}{\sigma_k} \right) \nabla k \right) + p_k - \rho \epsilon , \tag{4-3}$$

whereas for the dissipation ϵ we assert that:

$$\rho(u \cdot \nabla)\epsilon = \nabla \cdot \left(\left(\mu + \frac{\mu_T}{\sigma_\epsilon} \right) \nabla \epsilon \right) + C_{\epsilon 1} \frac{\epsilon}{k} p_k - C_{\epsilon 2} \frac{\rho \epsilon^2}{k} , \tag{4-4}$$

where, $\mu_T = \rho C_\mu \frac{k^2}{\epsilon}$

$$P_k = \mu_T (\nabla u (\nabla u + (\nabla u)^T))$$

$C_\mu, C_{\epsilon 1}, C_{\epsilon 2}, \sigma_\epsilon$ and σ_k are all constants.

μ_T is known as the turbulent viscosity and differs from the molecular viscosity as it depends on the flow field and the density. Turbulent viscosity varies over the flow domain, depending on the turbulence conditions.

The model contains five parameters, which are assigned the values given Table 4-1. The value of K_ν and B are used in COMSOL to describe turbulence at low Reynold numbers. Flow close to walls is modelled using wall functions.

Table 4-1: Turbulence model parameters

$C_{\epsilon 1}$	1.44	σ_ϵ	1.3
$C_{\epsilon 2}$	1.92	K_ν	0.41
C_μ	0.09	B	5.2
σ_k	1		

4.2.2. Wall functions

Wall functions divide the turbulent flow near the pipe walls into four layers. As shown in Figure 4-1. The $k - \epsilon$ model uses wall functions so that the flow in the buffer region is not simulated and consequently the velocity profile at the wall becomes discontinuous. Indeed, at the pipe wall the fluid velocity is zero. The layer above the pipe wall is called the viscous

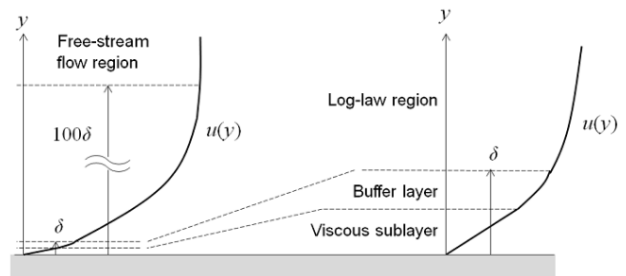


Figure 4-1: Velocity profile along the pipe wall where the fluid close to the wall is divided into four sublayers.

sublayer, and the layer above is called the buffer layer. In this layer turbulent stresses begin to dominate over viscous stresses. In the log-law region the average turbulent flow velocity at certain point is related to the logarithm of the distance from that point to the wall. Above the log-law region lies the free stream flow region. The viscous sublayer and the buffer layer are very thin compared to the other two regions. Wall functions ignore the flow field in the buffer layer and analytically compute a nonzero fluid velocity at the wall as can be observed in Figure 4-2.

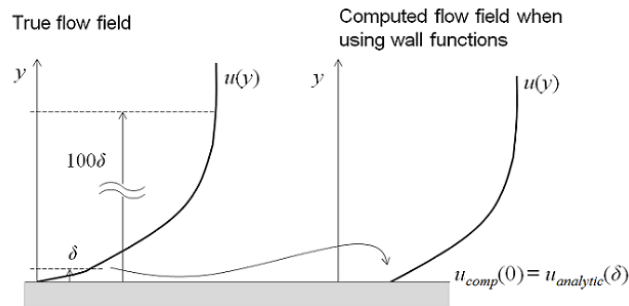


Figure 4-2: True flow field and computed flow field when using wall function.

4.2.3. Boundary conditions

A flow through a pipeline with the same diameter and length as used in the experiment will be implemented in the model. The flow is therefore axisymmetric and the boundaries on the wall and symmetry line are required to be stated. The procedures how to handle the boundary conditions for the $k - \epsilon$ model are rather vague. A fortiori it is not clear how COMSOL handles these boundary conditions. One of the clearest texts on this can be found in the book of Mohammadi and Pironneau (Mohammadi, B. and Pironneau, O., (1994)). At the boundaries we use $k = 0$ and $\epsilon = 0$. However, it is not clear what to do as the k-epsilon model is not valid near the wall. One option is to remove the viscous sublayer near the wall and specify k and ϵ at the boundary of the viscous sublayer. As all of this is not clear we assume that the log law is valid near boundary.

5. Results and Discussion

This chapter displays and discusses the results obtained during the experiments. First the experimental set-up is validated by running the base case solution, namely brine through the set-up. Then the results for the different polymeric and surfactant solutions are displayed and discussed. From this information we can derive which solution can be called a Drag Reducing Agent (DRA). As stated in chapter 2: for quantitative purposes Drag Reduction (DR) is defined as the pressure drop in the presence of a DRA divided by the pressure drop of the brine solution in the absence of a DRA. After this the results for the pressure drop localization using multiple pressure gauges and the DRA degradation are displayed and discussed. Finally, the results of the numerical simulation will be shown and compared with the experimentally obtained results.

5.1. Pressure Drop Measurements, Validation of Set-up

In order to validate the set-up, brine with a viscosity of 0.958 cp at 25°C is run through the set-up at flowrates from 1 ml/min up to 200 ml/min. At each flow rate the pressure drop over the inlet and outlet of the tube is measured. The result of this test can be observed in Figure 5-1. In this figure it can be observed that two trend lines can be fitted through the data points. These trends correspond to a turbulent and a laminar flow trend. The transition between laminar and turbulent can be seen as an additional increase in pressure drop as the flow rate increases. This transition happens at a flow rate between 70 and 80 ml/min and corresponds to Reynolds numbers 3179 and 3634 respectively. For flowrates above the 110 ml/min corresponding to a Reynolds number of 5000 the flow in the test tube is expected to be fully turbulent. DR is only expected to occur when there is turbulence in the system. According to Figure 5-1 this is associated with flowrates above 80 ml/min. Figure 5-2 shows the Reynolds number against the friction factor obtained by running brine through the flow loop. It can be observed that the friction factor is decreasing as the Reynolds number increases. From this figure it can be observed that at Reynolds numbers higher than 3000 the friction factor decreases with a slope that is smaller than at Reynolds numbers lower than 3000.

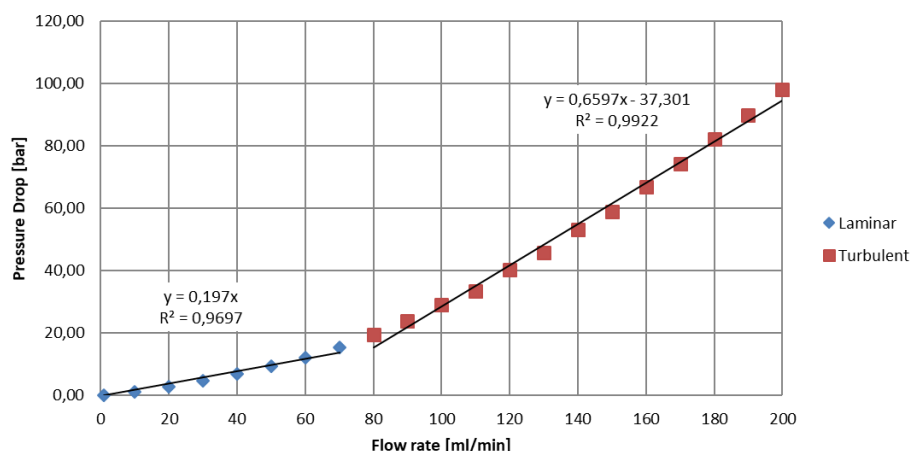


Figure 5-1: Pressure drop measurements at each flow rate for brine. A transition where the pressure drop increases is clearly visible between a flow rate of 70 ml/min and 80 ml/min

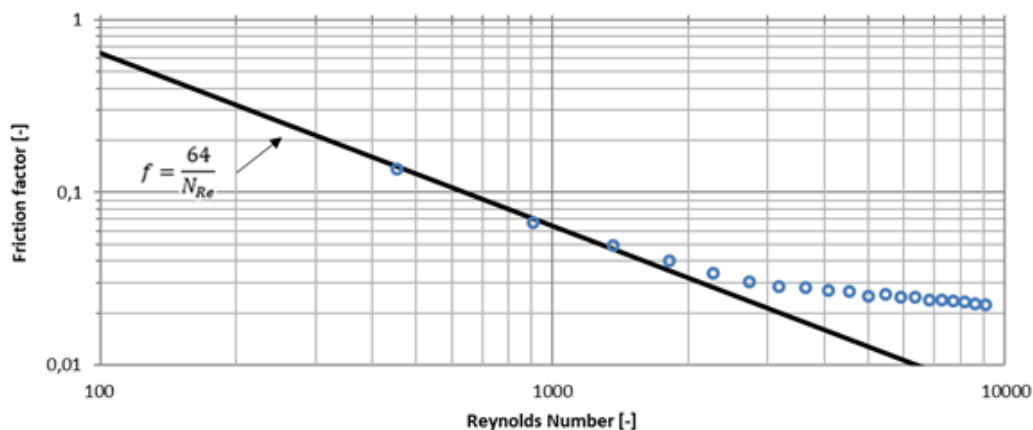


Figure 5-2: Reynolds number against the friction factor. The friction factor is derived from the experimentally obtained pressure drops. The black line shows the friction factor for laminar flows and approximately satisfies $f = 64/N_{Re}$

5.2. Drag Reduction By Polymers

Polymers are the most used drag reducers as it is reported that they can reduce drag significantly when only minute amounts are added to the solution flow. Polymers have therefore been studied extensively as DRAs. In this study two different types of polymers namely, biopolymers and synthetic polymers are tested on their DR abilities. The pressure drops obtained by flowing brine through the set-up are regarded as the base line from which the %DR is calculated.

5.2.1. Xanthan

Four different solutions with concentrations 10ppm, 30ppm, 90ppm and 1000ppm of xanthan dissolved in brine are made and tested on their drag reducing abilities. The solutions 10, 30 and 90 ppm solutions are created by diluting the 1000ppm solution. Figure 5-3 shows the flowrate against the pressure drop over the test tube for solutions of different xanthan concentrations compared to brine. The pressure drop over the test tube for the xanthan solutions is approximately the same as for brine at flowrates lower than 70 ml/min. The pressure drop seems to differ at flow rates higher than 80 ml/min corresponding to the turbulent flow regime as can be better observed in Figure 5-4. The 10 ppm xanthan solution has (within experimental error) the same pressure drop along the tube as for brine without xanthan. For the other concentrations a non-linear trend between the concentration and the pressure drop can be observed, where increasing the concentration leads to a lower pressure drop over the test tube. Figure 5-5 shows the flowrate against the percentage drag reduction (%DR) for the different xanthan solutions. The %DR is calculated using the pressure drop over the test tube for brine and for the solution as explained in chapter 2 by equation (2-11). In Figure 5-5 the 10 ppm xanthan solution does not show any DR within experimental error. For the other xanthan solution, it can be observed that DR only starts to occur at flowrates above 70 ml/min. This can be attributed to the fact that the DR ability is only at turbulent flow conditions. From this information it can be inferred that the critical concentration for xanthan at which significant DR occurs lies between 10 and 30 ppm. What is also very interesting in this figure is that at flowrates lower than 130 ml/min the 90 ppm xanthan solution seems to have a larger DR effect than the

1000 ppm xanthan solution. Also does the 1000 ppm xanthan solution show a negative %DR (corresponding to a drag increase) at flowrates where the flow is assumed to laminar. This observation can be attributed to the increase in viscosity caused by the relatively high concentration of xanthan. At very low flow rates this effect is even further increased.

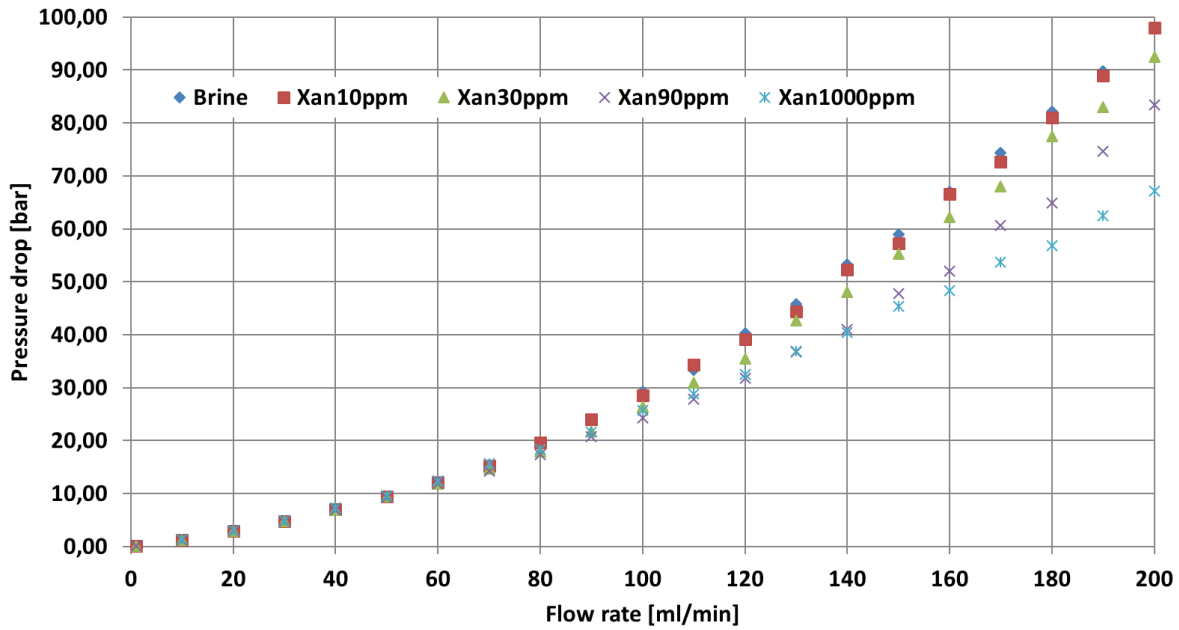


Figure 5-3: Flow rate against the pressure drop for different concentrations of xanthan dissolved in brine

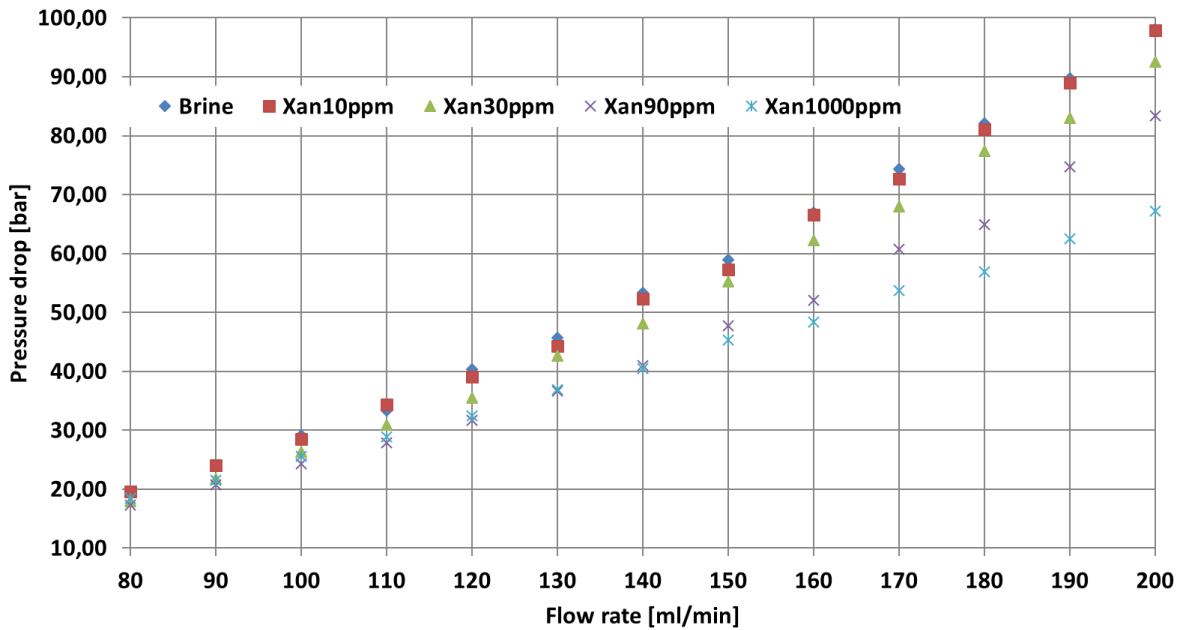


Figure 5-4: Flow rate against the pressure drop at turbulent flow for the different concentrations of xanthan dissolved in brine

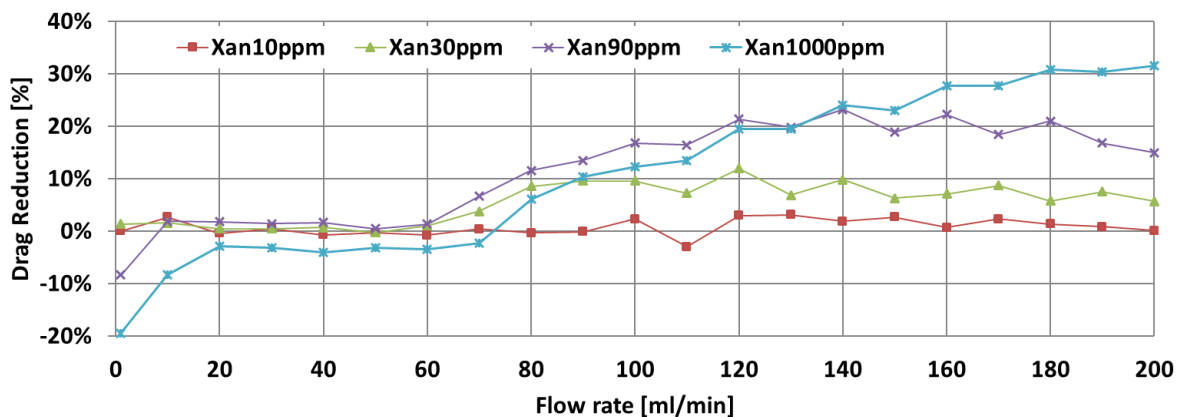


Figure 5-5: Flow rate against the %DR for the different concentrations of xanthan dissolved in brine

5.2.2. FLOPAAM EM5205

For the synthetic emulsion polymer FLOPAAM EM5205 three different solutions viz., of 10 ppm, 30 ppm and 90 ppm were prepared. These solutions are diluted from a mother solution with a concentration of 10.000 ppm that was prepared using the method described in chapter 3. These solutions are run through the flow loop at different flow rates and the pressure drop over the test tube is measured. Figure 5-6 shows the flow rate against the pressure drop for different concentrations of the emulsion polymer. At the flowrates that are assumed to have laminar flow all the solutions have approximately the same pressure drop over the test tube. At the flow rates where the flow is assumed to be turbulent all emulsion polymer solutions seem to have a lower pressure drop over the test tube compared to pressure drop measured in brine without any additive. The critical concentration for this polymer at which significant DR starts to occur is therefore less than 10 ppm. In Figure 5-7 it can be observed that the 10 ppm emulsion polymer solution shows the lowest pressure drop over the test tube at flow rates from 90 ml/min to 120 ml/min whereas the 30 ppm and 90 ppm solutions seem to have the same pressure drops over the test tube at these flow rates. For flow rates above 120 ml/min, the 10 ppm emulsion polymer solution has the highest pressure drop compared to the 30 ppm and the 90 ppm solution. For flow rates between 130 ml/min to 190 ml/min the 30 ppm solution has the lowest pressure drop over the test tube. At a flow rate of 200 ml/min the 90 ppm solution has the lowest pressure drop over the test tube. Figure 5-8 shows the flow rate against the %DR for each emulsion polymer solution. For all the flowrates where the flow is assumed to be laminar the pressure drop is larger than the pressure drop in the brine solution. The drag increase is related to the concentration of the emulsion polymer (i.e., the drag increases with increasing concentration). This effect is attributed to the viscosity enhancing effect of the emulsion polymer. At the flowrates where the flow is assumed to be turbulent all solutions show DR. The maximum DR for the 10 ppm solution is achieved at a flow rate of 110 ml/min, whereas the maximum DR's for the 30 ppm and 90 ppm solutions are achieved at 170 ml/min and 200 ml/min respectively. At flow rates above 110 ml/min the %DR decreases for the 10 ppm solution. The same happens at flowrates above 170 ml/min for the 30 ppm solution. A decrease in %DR for the 90 ppm solution could not be measured as the maximum flow is limited by the pump. Figure 5-8 shows that an increase in concentration leads to a higher maximum DR at turbulent flows but also an increase in drag at laminar flow conditions. The delay in reaching the maximum

DR when the concentration is increased can be related to the increase in viscosity. This increase in viscosity causes a higher pressure drop. In turbulent flows this increase in pressure drop needs to be overcome before DR is useful. Section 5.4 will discuss the rheology of these solution. When assuming a linear relationship between the viscosity and concentration, which is reasonable in this small range of concentrations (0 ppm – 90 ppm), the increase in viscosity due to the small amount of added polymer is ~ 0.04 cP per increase of 10 ppm of emulsion polymer and ~ 0.01 cP per increase of 10 ppm for xanthan.

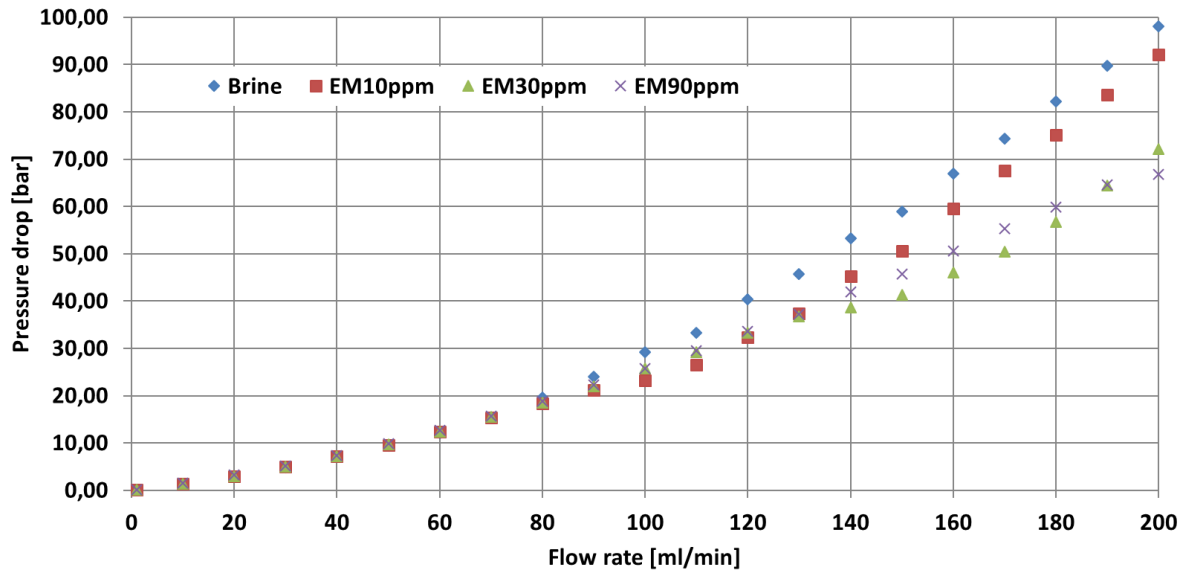


Figure 5-6: Flow rate against the pressure drop for different concentrations of emulsion polymer dissolved in brine

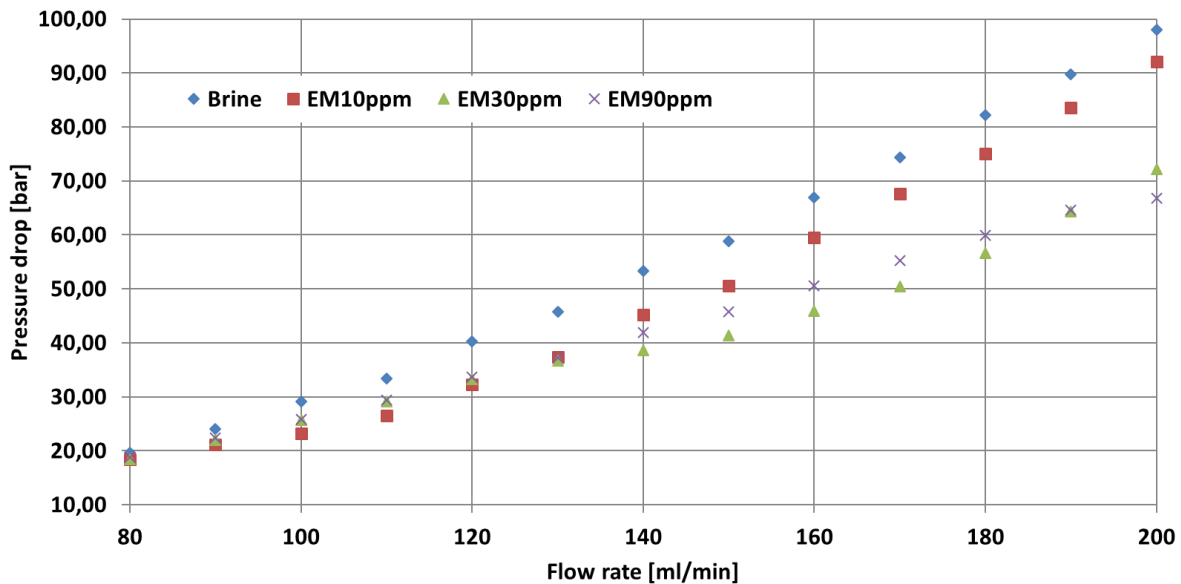


Figure 5-7: Flow rate against the pressure drop for different concentrations of emulsion polymer dissolved in brine

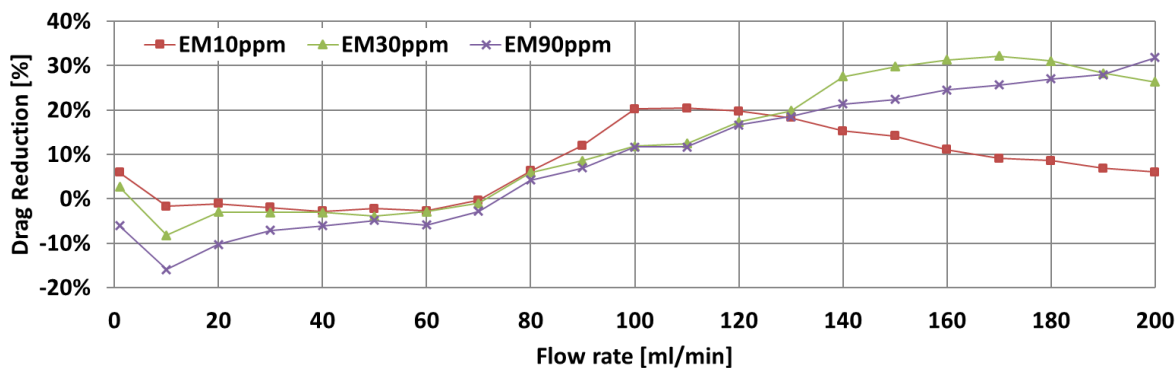


Figure 5-8: Flow rate against the %DR for the different concentrations of emulsion polymer dissolved in brine

5.2.3. Polymer DRA comparison

Both polymer types tested in this study can be classified as a DRA. Xanthan has a lower overall DR capacity than the emulsion polymer. A 10 ppm emulsion polymer solution has almost the same maximum DR as a 90 ppm xanthan solution. This can be attributed to the more flexible chemical structure of the emulsion polymer, causing it to align more properly with the flow lines and thus lead to a higher effectiveness in DR. Xanthan shows a slower decrease in DR when the flowrate increases above the flow rate at which the maximum DR occurs. The emulsion polymer has a higher increase in drag at the flow rates corresponding to laminar flow than xanthan due to the higher viscosity enhancing ability of the emulsion polymer. Figure 5-9 shows a comparison between the emulsion polymer and xanthan. For engineering applications the DR plot of Figure 5-9 is sufficient to describe the drag reduction due to addition of these additives. When comparing the Reynolds number against the friction factor for each solution one might need to correct the Reynolds number due to the influence of the increased solution viscosity. However, our definition of drag reduction is unambiguous and does not depend on the definition of the Reynolds number. The friction factor can be calculated from the measured pressure drop at each Reynolds number and can be plotted as is shown in Figure 5-10 where, the Reynolds number is calculated using: $N_{Re} = \rho v D / \mu_{brine}$.

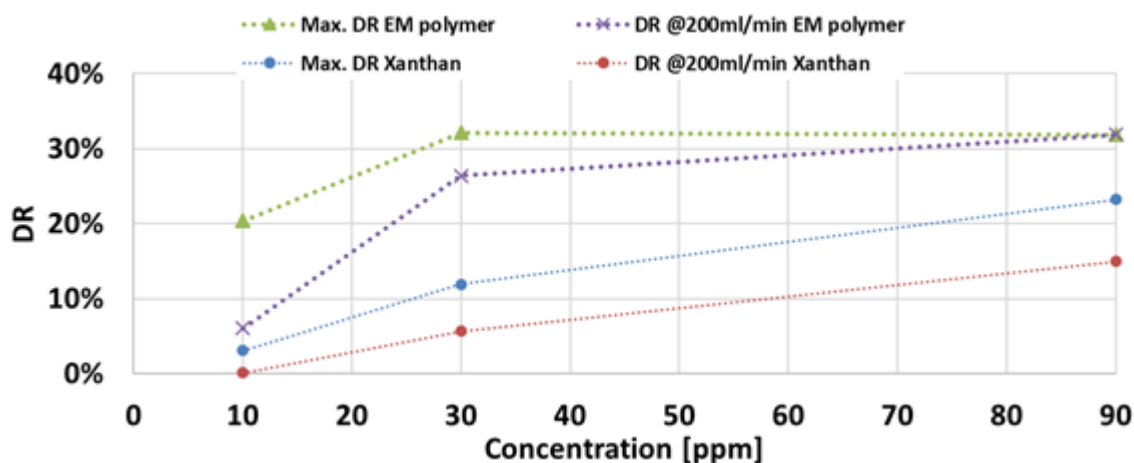


Figure 5-9: Maximum %DR and %DR at 200 ml/min as function of concentration for the polymeric solutions used in this study

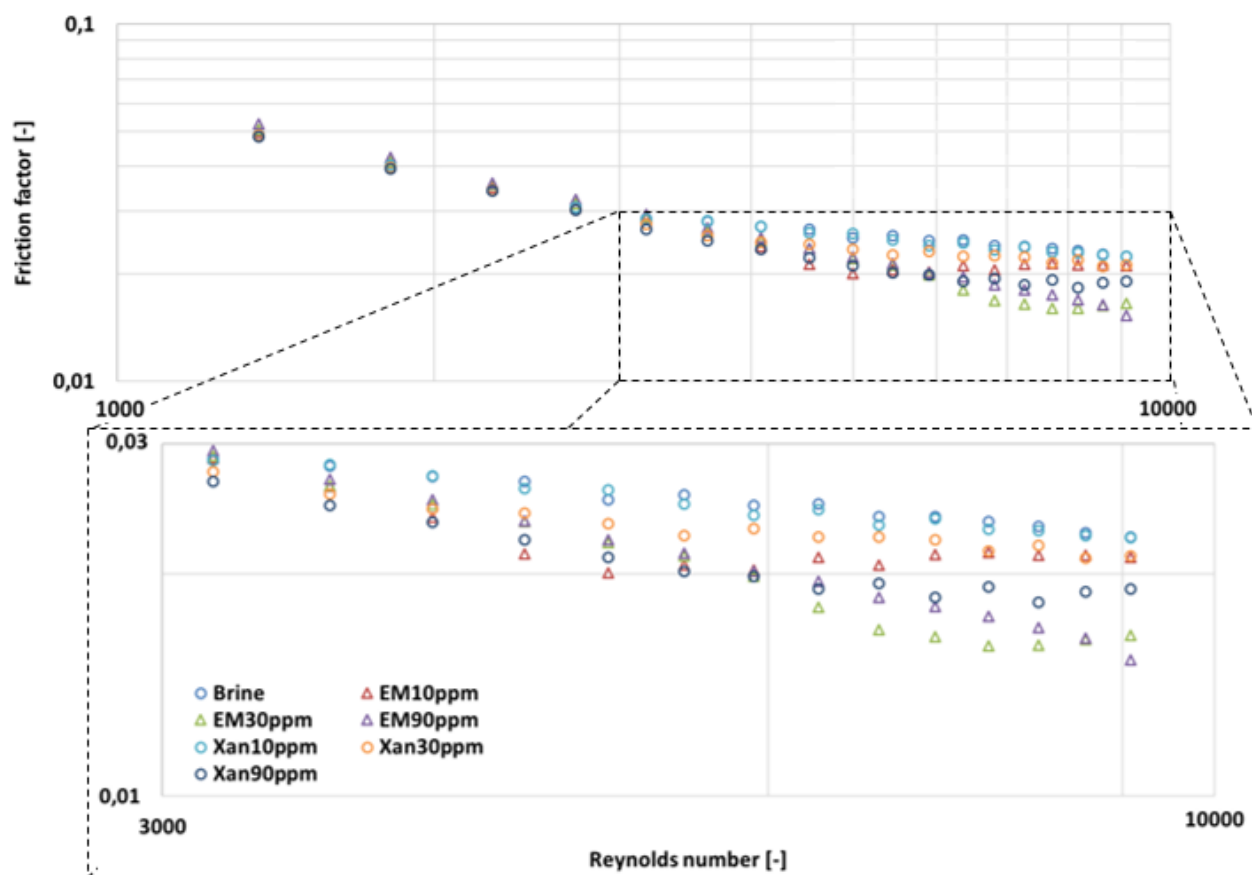


Figure 5-10: Friction factor as function of Reynolds number for the polymeric solutions at various concentrations

5.3. Drag Reduction by Surfactants

Surfactants are less used as drag reducers as their negative environmental footprint is larger than other DRAs. New surfactants that are more environmentally acceptable such as the nonionic APG are studied to be applied as DRAs. In this study three different branches of surfactants namely, cationic-, anionic- and nonionic surfactants are tested on their DR abilities. For a surfactant to reduce drag, the surfactant solutions need to contain aggregates of the surfactant molecules. These aggregates should interact with the turbulent flow thus, diminishing the turbulent eddies. Before the surfactants are deployed in the flow loop they need to be screened in order to get an idea at what concentrations the aggregates that lead to DR start to form.

5.3.1. Critical Micelle Concentrations

The critical micelle concentration (CMC) is the concentration at which aggregates known as micelles start to form. The CMC depends on the salt concentration (Humley, I.W., (2000)). In this study the surfactants are dissolved in a specific brine that is resembling sea water. The CMC needs therefore to be determined to know at what concentration micellar structures start to form. The CMC is derived by measuring the surface tension at different concentrations for the surfactants using a tensiometer. In this experiment for

each surfactant 10 diluted solutions with different concentrations were created. Plotting the concentration against the surface tension revealed that extra dilutions at certain concentrations are necessary to make the determination of the CMC more accurate. Eventually each surfactant needed more than 10 data points to come up with a reliable CMC. Furthermore, each measurement is repeated a minimum of 10 times for each concentration. The error bars show the standard deviation between these measurement values. The temperature was $23.5^{\circ}\text{C} \pm 0.5^{\circ}\text{C}$ during the experiments. The surface tension measurements as function of the logarithmic concentration of the surfactants can be exhibited in Figure 5-11. Table 5-1 shows the CMC values for the different surfactants.

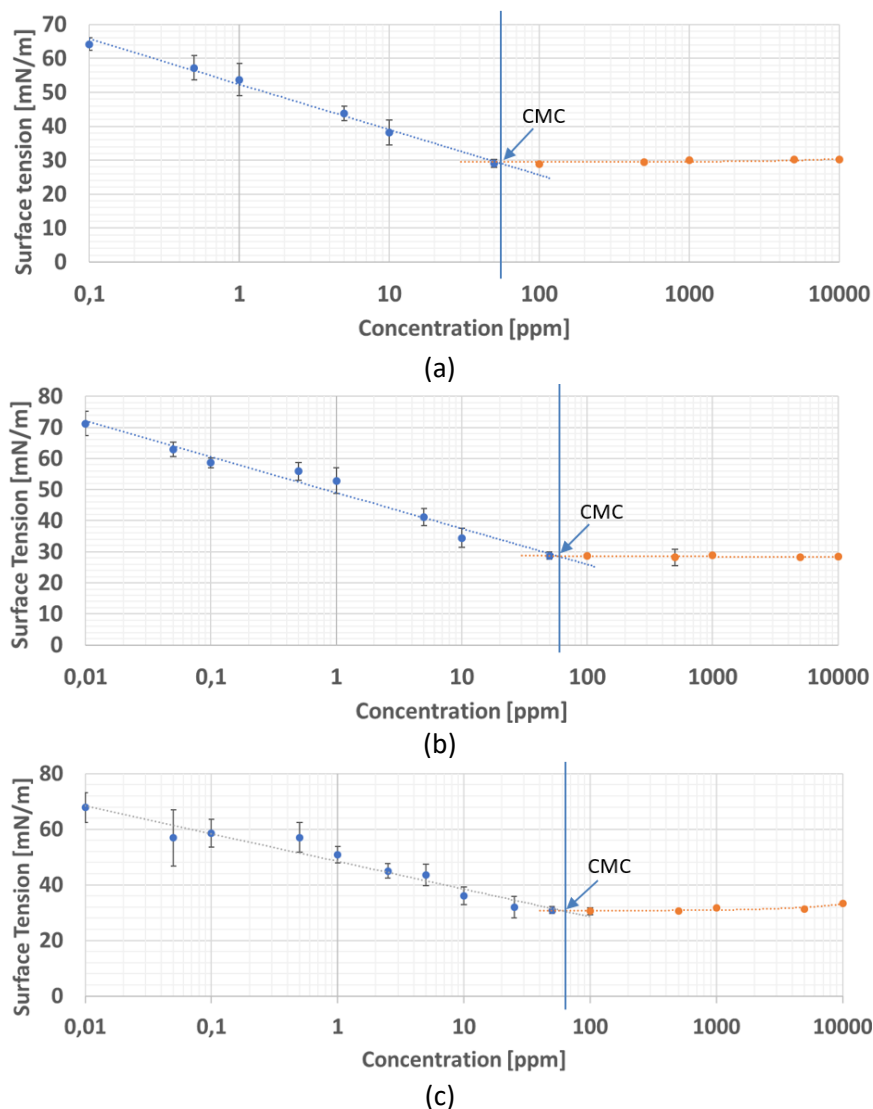


Figure 5-11: Surface tension as function of the logarithm of surfactant concentration, where (a) AOS, (b) APG and (c) CTAB. The arrow points out the critical micelle concentration

Table 5-1: CMC values for the three different surfactants measured at a temperature of $23.5^{\circ}\text{C} \pm 0.5^{\circ}\text{C}$

Surfactants	CMC
AOS	55 ppm
APG	60 ppm
CTAB	65 ppm

5.3.2. Hydrated particle diameter and anisotropy

Dynamic Light Scattering (DLS) (Berne, B.J. and Pecora, R., (2000)) makes it possible to measure the diffusion coefficients, which can be interpreted in terms of the hydrated particle size of the micelles (Hunter, R.J., (2001)) present in the surfactant solutions by measuring the time dependent fluctuations in the scattering intensity. The procedure used to determine the particle size is explained in chapter 3.2.1.2. The results of DLS are expressed in terms of the z-Average. For more information about how the z-Average is determined see Appendix A: z-Average.

Special care needed to be taken in making the surfactant solutions as they need to be as dust free and also not contain any air bubbles as this might influence the results. The z-average as function of the concentration is shown in Figure 5-12. At least three measurements are taken successively for each concentration. The standard deviation is calculated from these successive measurements and is depicted as error bars in Figure 5-12. Table 5-2 summarizes the z-average diameters (Koppel, D.E., (1972)) and polydispersity index values for each sample. The polydispersity index gives an estimate of the width of the size distribution. The particle size first decreases as concentration increases, but above a concentration of 10.000 ppm the particle size detected by the zeta sizer increases as can be observed in Figure 5-12. The decrease in the hydrated particle diameter can be attributed to the charge repulsion forces between the surfactant molecules, which increase as more surfactant molecules enter the solution. This repulsion increases the diffusion speed of the micelles and can thereby lead to a decrease in the hydrodynamic diameter. The increase in particle size may be due to growth of the micelles. The hydrated particle size does not tell much about the micellar shape, as an increasing particle diameter can simply mean that the micelles remain spherical but that the diameter of the micelle increases. For classification of the micellar shape, DLS is simply not enough. Other hydrodynamic methods to characterize micellar shape and size, such as Depolarized Dynamic Light Scattering (DDLS) or Multi Angle Dynamic Light Scattering (MADLS) are available. Bruining J. and Fijnaut, H.M., (1979) used DDLS and showed that they could determine the shape of ribosomes back in 1979. The zeta sizer used in this study could not perform these kinds of measurements.

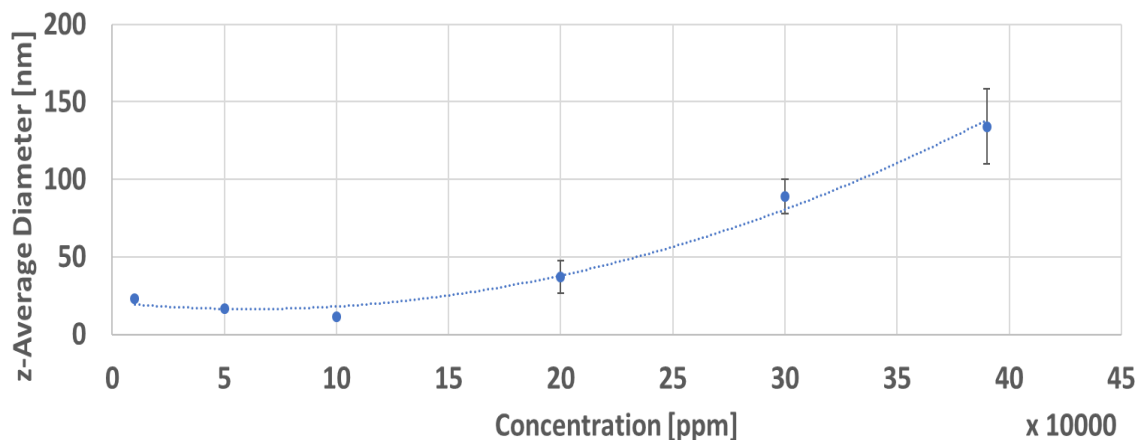


Figure 5-12: z-Average diameter as function of the AOS concentration. The error bars depict the standard deviation calculated from the successive measurements at each concentration

Table 5-2: z-Average diameters and polydispersity index values obtained for AOS. All samples are measured at least three times successively and the values in the table depict the averages of the obtained values

Concentration [ppm] x10000	z-Average [nm]	Polydispersity Index
39	134,18	0,325
30	89,03	0,275
20	37,03	0,253
10	11,12	0,222
5	16,34	0,322
1	23,29	0,175

5.3.3. Drag reduction

Size distribution derived from the DLS results showed that very high concentrations are needed to obtain significant changes in size of the particles present in the solutions. Using the surfactants at these concentrations in the flow loop would be very costly (Li, P.W., et al., (2000)). None of the surfactants showed DR even if it is known that at these concentrations micelles are present in the solutions and relatively high concentrations are used as shown in Figure 5-13. Abed, M.A. et al., (2004) showed that for AOS no spherical to rod-like micelle transition happens at concentrations from 0 to 100 mM. At these concentrations AOS surfactants should not have any drag reducing ability. This is consistent with this study where AOS showed no DR at concentrations up to 20.000 ppm. The hydrophilic head of the APG surfactant is electrically neutral. It was therefore expected that no additive is needed to ensure the formation of rod-like micelles and therefore DR. DR measurements with APG showed no DR for concentrations up to 20.000 ppm. This contradicts the work of Cai, S. and Higuchi, Y. (2014), who experimented on APG without adding any additives and observed DR. It should be noted that the commercial names of the used APG differ. The commercial name of the APG used in their study is Glucocon 600UP whereas the APG used in this study is commercially known as Triton™ CG-650 and supplied by DOW chemicals. Using additives to stimulate formation of rod-like micellar structures is therefore used. Stradner, A., et al. (2000) showed that addition

of a fatty alcohol to APG solutions has an enormous effect on the micellar size and shape, where the micelles grow to giant and highly flexible micellar aggregates. Stradner et al., used hexanol as a fatty alcohol. In this study 1-Pentanol (which can also be classified as a fatty alcohol) is added to the nonionic APG surfactant to induce these giant aggregates. APG and 1-pentanol solutions with concentrations up to 10.000 ppm with APG to 1-pentanol ratios of 1:0.15 and 1:1 did not show a drag reducing effect.

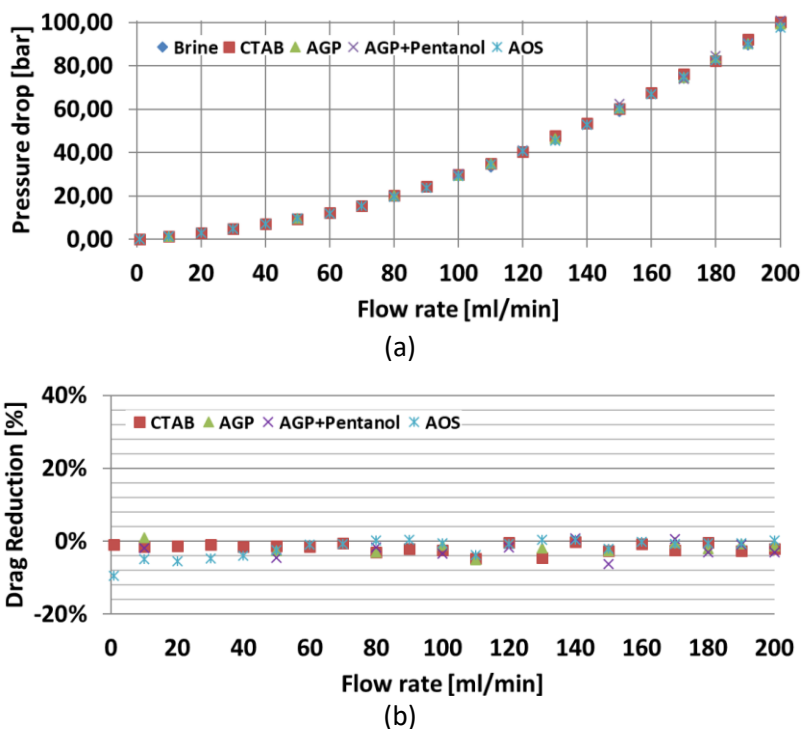


Figure 5-13: (a) Pressure drop as function of flowrate for the surfactants and brine as baseline. All the data points for the surfactant solutions coincide with the data points obtained for brine, meaning that the solutions do not show any DR. (b) %DR as function of flowrate for the surfactants. All data points are close to 0 or lower than zero meaning no significant DR occurs. The surfactant concentrations are 10.000 ppm and the ratio between APG and 1-pentanol is 1:1. The ratio 1:0.15 shows the same result.

Addition of the counter ion sodium salicylate (NaSaL) to CTAB can also induce the formation of rod-like micelles, by neutralizing the electrostatic repulsion between the ionic head groups (Ohlendorf, D., (1986)). The counter ion added to CTAB penetrates the organic core of the CTAB micelles and screens the positive charges of the cationic head groups. NaSaL therefore stabilizes the micellar structure of the CTAB micelles and thereby reduces the inter-micellar repulsive forces. This favors the formation of larger micelles that can even be rod-like. These rod-like micelles can entangle and form wormlike micelles. Where CTAB did not show any DR at concentrations up to 20.000 ppm, addition of NaSaL with a 1:1 ratio did lead to DR. This leaves the CTAB/NaSaL solution the only effective surfactant drag reducer in this study. Figure 5-14 shows the flowrate against pressure drop and %DR for the CTAB+NaSaL solutions. In Figure 5-14 (a) it can be observed that the pressure drop over the test tube is the same as brine for a 100 ppm concentration. The 2500 and 4500 ppm CTAB+NaSaL concentrations seem to have a comparable pressure drop over the test tube, which are lower than when brine flows through the flow loop. The 1000 ppm solution has a small reduction in pressure drop over the tube compared to brine. Figure 5-14 (b) shows the flow rate against the %DR for the CTAB+NaSaL solutions. Also, here it can be clearly observed that the 100 ppm

solution does not show DR, except at flow rates 1 and 10 ml/min where %DR is 4%. At these flow rates it takes a long time before the pressure stabilizes in the system. It can be that the experiment at these flowrates is stopped too early (i.e., before the pressure stabilized for that given flow rate), leading to a lower pressure drop calculation over the tube and therefore to an apparent DR. The 1000 ppm solution has a maximum %DR of 16% at a flow rate of 100 ml/min. The critical concentration at which DR starts to occur for a 1:1 CTAB:NaSaL solution lies between 100 and 1000 ppm. Increasing the flow rate above 100 ml/min reduces the %DR for the 1000 ppm solution. The 2500 ppm CTAB+NaSaL solution has a maximum %DR of 33% at a flow rate of 190 ml/min, and the 4500 ppm solution has a maximum %DR of 29% at a flow rate of 200 ml/min. In this study it is not made clear if at these flow rates the maximum %DR is achieved as the set-up used in this study has a pump with a limited maximum delivery rate of 200 ml/min. The solutions that decrease drag at flowrates where the flow is assumed to be turbulent also increase drag at flowrates where the flow is assumed to be laminar. The increased drag can be ascribed to the increase in viscosity of the solution due to the viscosity enhancement of the CTAB+NaSaL mixture. The decrease in %DR for the 1000 ppm solution when the flow rate becomes larger than 100 ml/min can be ascribed to the increase in shear that the micellar structures experience. The micellar structures can therefore break and lose their DR abilities.

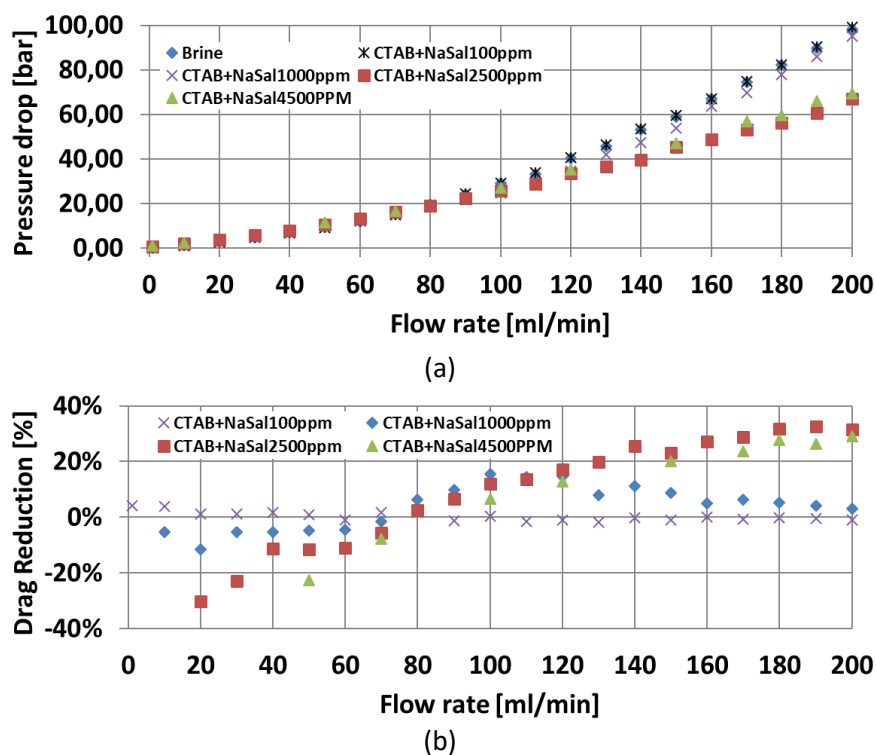


Figure 5-14: (a) Pressure drop as function of flowrate for the CTAB+NaSaL solutions and brine as baseline. The data points for 100 ppm solution coincide with the data points obtained for brine, this solution therefore does not reduce drag. (b) %DR as function of flowrate for the CTAB+NaSaL solutions. All data points for the 100 ppm solution are close to 0 also implying that this solution does not reduce drag. The other concentrations reduce drag significantly when the flow is turbulent

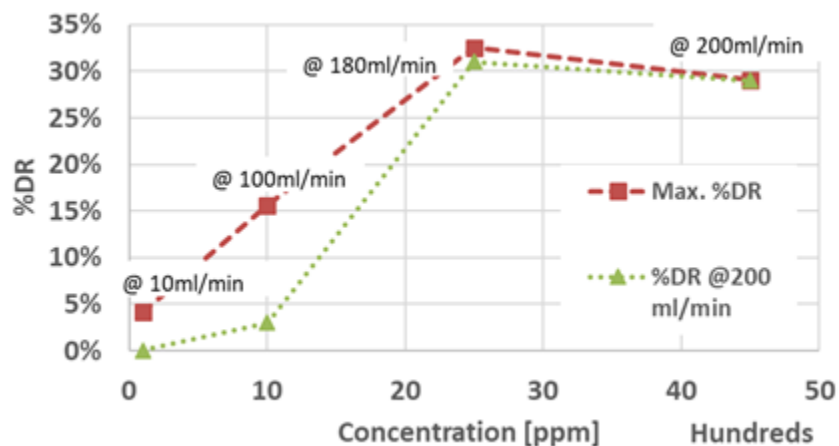


Figure 5-15: Maximum %DR and %DR at 200 ml/min as functions of concentration for the CTAB+NaSaL surfactant

5.4. Rheology

The results of the flow loop tests revealed that both polymers and the surfactant CTAB+NaSaL can be regarded as a DRA. Rheology measurements over a range of concentrations and shear rate are performed in order to gain a broader insight into the reason behind the drag reducing effect of these solutions at turbulent flow conditions. First the viscosity as function of shear rate for the polymeric DRAs will be discussed after which the results of the surfactants will be discussed. All the viscosity measurements are performed at a constant temperature of 25°C using the Anton Paar MCR302 rheometer with a concentric set-up (Couette flow configuration). The shear rate used ranges from 10^{-1} s^{-1} to 10^3 s^{-1} in this study. For low viscosities such as that of the brine the concentric set-up leads to untrustworthy results for shear rates less than 1 s^{-1} and above 100 s^{-1} . At high shear rates the flow around the concentric cylinder becomes turbulent as a result of which the concentric set-up is no longer a trustworthy measurement tool.

5.4.1. Shear rheology of the polymeric solutions

Figure 5-16 shows the viscosity of the polymeric solutions as function of the shear rate. It can be observed that the xanthan and emulsion polymer solutions up to 90 ppm behave as a Newtonian fluid (i.e., the shear stress of the fluid is directly proportional to the gradient of the flow perpendicular to the shear plane). The viscosity of these solutions is approximately the same as for brine at 25°C. The viscosity curves for the 1000 ppm xanthan and the 10.000 emulsion polymer solutions seem to flatten out toward a constant value, η_0 at low shear rates. This value is known as the low-shear Newtonian viscosity. At higher shear rates both solutions appear to behave shear thinning. Increasing the concentration leads to a higher Newtonian viscosity. At low concentrations (e.g., the 10 ppm, 30 ppm and 90 ppm polymer solutions) the polymer solution can be viewed as a colloidal solution where the polymer molecules are coiled in the shape of a solid spheres. The probability of the polymer molecules interacting with each other increases as the concentration increases. When the polymer molecules get entangled with each other they show an increased solution viscosity.

The 10 ppm, 30 ppm and 90 ppm polymer solutions all exhibit DR. At these concentrations no shear thinning is observed. Therefore, shear thinning cannot be the rheological property which is responsible for DR in the turbulent flow regime.

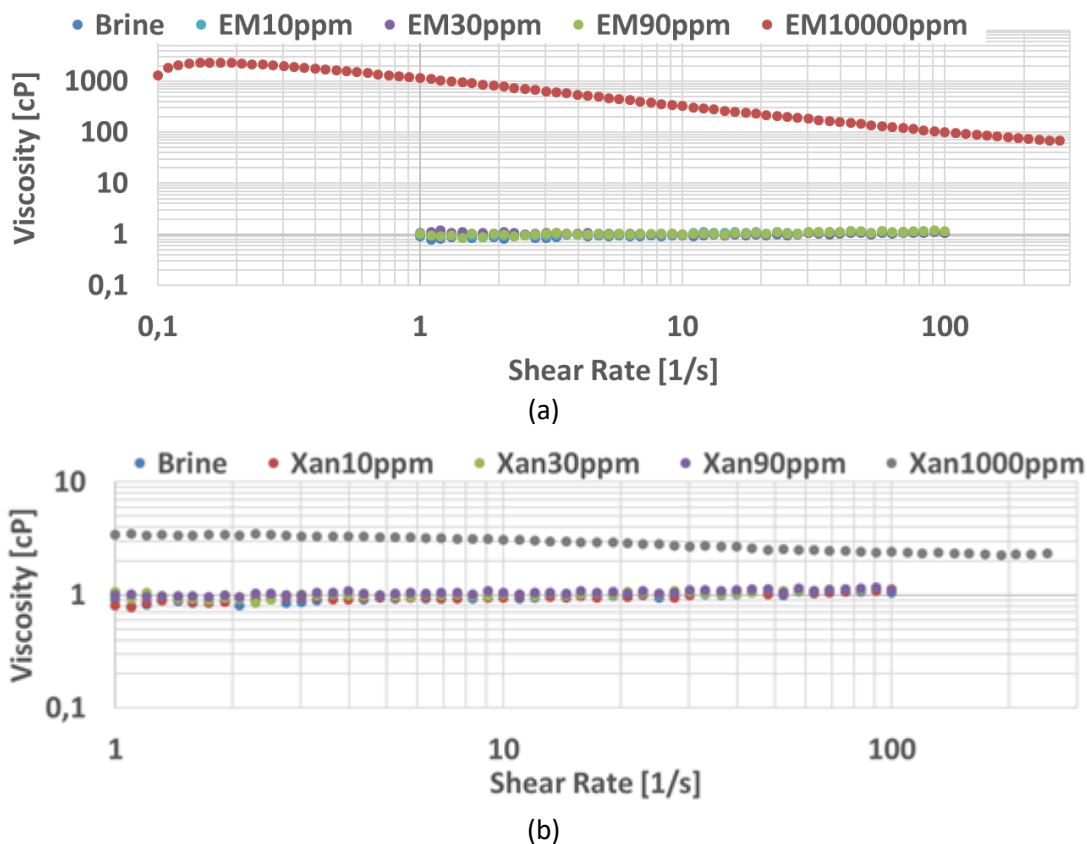


Figure 5-16: Viscosity as function of shear rate for the polymeric solutions used in this study

5.4.2. Shear rheology of the surfactant solutions

CTAB combined with the counter ion NaSaL is the only surfactant in this study that can be called a DRA. The other surfactants did not seem to be effective as a drag reducer. Nevertheless, rheological measurements are performed on these surfactants to observe the difference between the surfactants that reduce drag and those who do not. The surfactants AOS, APG and APG with 1-propanol behave as a Newtonian fluid. Increasing the surfactant concentrations leads to an increase in viscosity due to an increase of the dissolved surfactants. For AOS a 100.000 ppm solution led to viscosity that is approximately 2 times higher than the viscosity of the brine. The results of the surfactants that are not capable of reducing drag can be consulted in Appendix B: Rheology of non DR surfactants.

Figure 5-17 exhibits the viscosity as function of shear rate at different concentrations of CTAB+NaSaL. The 100 ppm solution behaves as a Newtonian fluid and does not enhance the viscosity of the brine significantly. This solution did not lead to any %DR as can be observed in Figure 5-15. The other concentrations behave more shear thinning as the concentration increases. The Newtonian plateau is visible for the 1000 ppm, 2500 ppm, 4500 ppm and 10.000 ppm concentrations at low shear rates. Increasing the concentration leads to an increase in the viscosity of this Newtonian plateau and the viscosity of the shear thinning region in general. Drag reducing surfactants always contain rod-like micelles.

These micelles are anisotropic and can be orientated in shear flow. At low shear rates the micelles rotate in a shear flow with a nearly constant rotational speed. When the shear rate increases the rotational speed of the rod-like micelles becomes non-uniform and the rods become more and more aligned in the flow direction (Gyr, A. and Bewersdroff, H.-W., (1995)). Where the Brownian motion dominates at low shear rates, the shear gradient dominates at high shear rates causing the rods to align in the flow direction. Due to this alignment the rod-like micelles behave as a concentrated polymer solution. (Gyr, A. and Bewersdroff, H.-W., (1995)). The aligned rod-like micelles cause a lower hydrodynamic resistance, which causes the shear thinning behavior. The 1000, 2500 and 4500 ppm solution all cause DR. Therefore, we can conclude that these solutions contain rod-like micelles. The shear viscosity measurements also indicate that these CTAB+NaSaL solutions have shear thinning behavior and therefore contain rod-like micelles. The results of APG and the 100 ppm CTAB+NaSaL solutions do not increase the viscosity and as a result shear thinning is not observable. At high concentrations of AOS the viscosity is significantly increased and the solution still behaves Newtonian. It is therefore expected that even at these high concentrations of AOS the micelles are still not rod-like and no DR will occur.

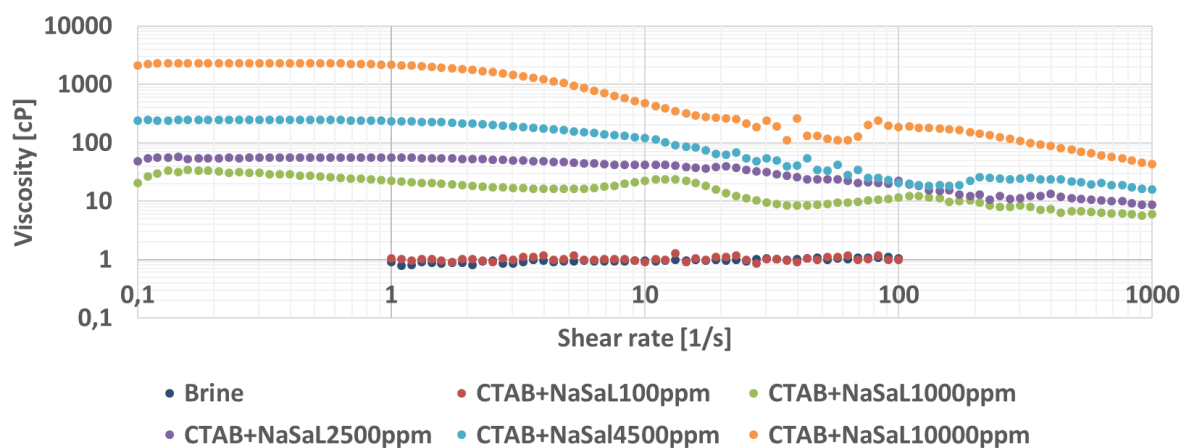


Figure 5-17: Viscosity as function of shear rate for different concentrations of CTAB+NaSaL.

5.5. Pressure Drop Localization

Multiple pressure gauges are connected at different locations along the test tube in order to assess the pressure drop over various parts of the test tube. This will also give insight in how the drag is being reduced along the test tube. Six pressure gauges are connected to the tube. It was expected that the first part of the test tube would be the most interesting part as that will be the location where the turbulent flow will start. Also does the flow enter the test tube by going through an elbow. Therefore, the pressure gauges at the first part are placed more closely to each other. The first pressure gauge is installed at the inlet of the test tube. The other 5 pressure gauges are installed at 10 cm, 30 cm, 70 cm, 110 cm and 150 cm from the inlet of the tube. These six pressure gauges made it possible to calculate six pressure drops along various locations of the tube. The pressure drops are respectively called dp_1 , dp_2 , dp_3 , dp_4 , dp_5 and dp_{tube} . Figure 5-18 shows a schematic view of how the pressure gauges are placed along the test tube, and over what pressure gauges the pressure drops are calculated.

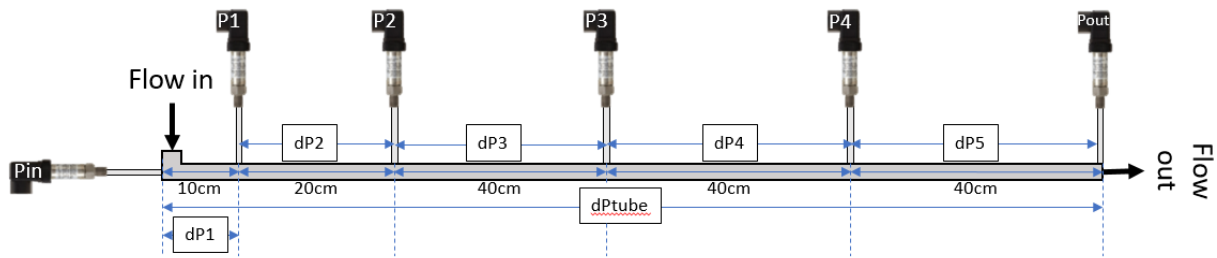


Figure 5-18: Schematic view of the placement of the pressure gauges along the test tube and the names for the pressure drop calculations

The solutions used for this experiment are the solutions that showed significant DR, namely xanthan 90 ppm, emulsion polymer 90 ppm and CTAB+NaSaL2500ppm. Figure 5-19 shows the pressure as function of the distance along the test tube. In Figure 5-19 (a) the pressures at a flow rate of 50 ml/min are plotted. At this flow rate the flow through the test tube is assumed to be laminar. It can be observed that xanthan and the emulsion polymer have the same pressures as brine at each location along the test tube, indicating that no DR occurs. The CTAB+NaSaL solution has a pressure drop along the tube that is higher than the other DRAs and even brine, indication a drag increase which can be attributed to the significant increase in viscosity caused by the CTAB and NaSaL combination. Figure 5-19 (b) exhibits the same as (a) but at a flow rate of 200 ml/min. At this flow rate the flow through the test tube is assumed to be turbulent. In this plot brine has the highest pressure at each location along the test tube followed by xanthan, CTAB+NaSaL and the emulsion polymer.

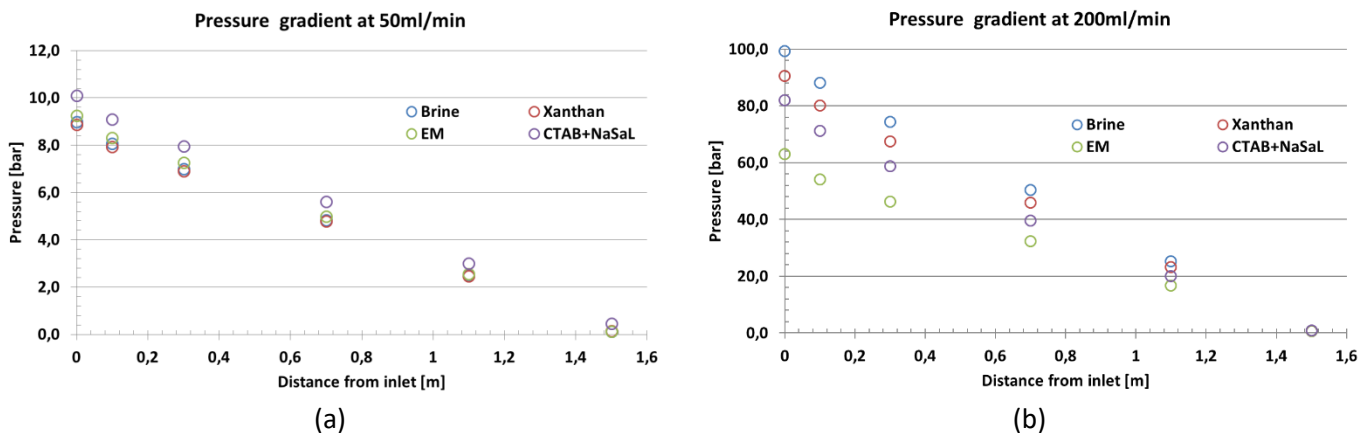


Figure 5-19: Distance from the inlet of the test tube against the pressure for: (a) a laminar flow of 50 ml/min and (b) a turbulent flow of 200 ml/min. The concentrations are 90 ppm, 90 ppm and 2500 ppm respectively for xanthan, EM and CTAB+NaSaL

The pressure drops calculated are not all over the same length of test tube as is shown in Figure 5-18. The pressure drops are normalized to a pressure drop over a section of one meter in order to be able to compare the pressure drops calculated along the test tube with each other. Figure 5-20 exhibits the pressure gradient over a section of one meter for the different DRAs. For all solutions applies that the pressure drop per meter is significantly higher at dP1, corresponds to the pressure drop over the first 10 cm of the test tube, than the other sections of the test tube. This increase in pressure drop can be attributed to the elbow at the beginning of the test tube. The second interval of the test tube corresponding to dP2 has a slightly higher pressure drop compared to other sections. A reason for this is

that this section of the test tube lies closely to the first section and that the steady pressure drop has not yet been established in the second section. The other sections experience a constant pressure drop. Figure 5-20 clarifies that the pressure drop over all the sections is lowest for the emulsion polymer. At dP1 CTAB+NaSaL has a slightly higher pressure drop than xanthan even though at all the other intervals xanthan has a higher pressure drop. Figure 5-21 shows the %DR at each interval along the test tube. Also in this figure the observation of the cross over between xanthan and CTAB+NaSaL can be observed between dP1 and dP2. The difference between dP1 and dP2 is more significant for the emulsion polymer and the CTAB+NaSaL surfactant than with xanthan. The elbow and the higher viscosity of the CTAB+NaSaL solution decrease the DR ability of this solution in the first part of the test tube. In the other parts CTAB+NaSaL seems to have an increasing %DR as the distance from the inlet increases. The emulsion polymer shows a decreasing trend in terms of DR along the test tube whereas xanthan shows a steadier DR along the test tube. This difference can be attributed to the more rigid chemical structure of xanthan. Furthermore, the velocity profile is not fully developed immediately at the entrance of the test tube. The distance for the velocity profile to fully develop is dependent on the flow velocity and on the tube diameter. It was assumed that due to the small diameter of the test tube the velocity profile would develop quickly thanks to the high velocity. But even though does the incompletely developed velocity profile negatively influence the %DR in the first section of the test tube.

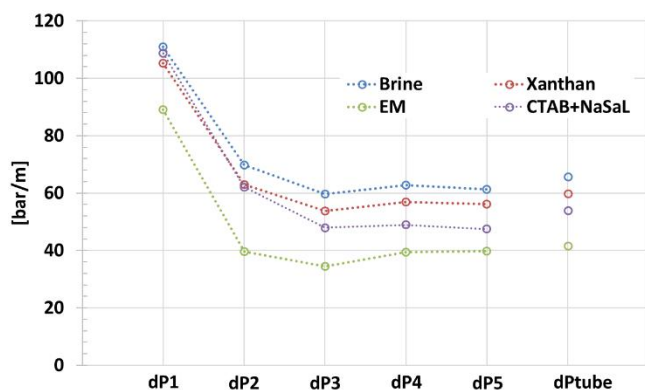


Figure 5-20: Pressure drop over each interval normalized over one meter. The pressure drop calculations are taken at a flow rate of 200 ml/min

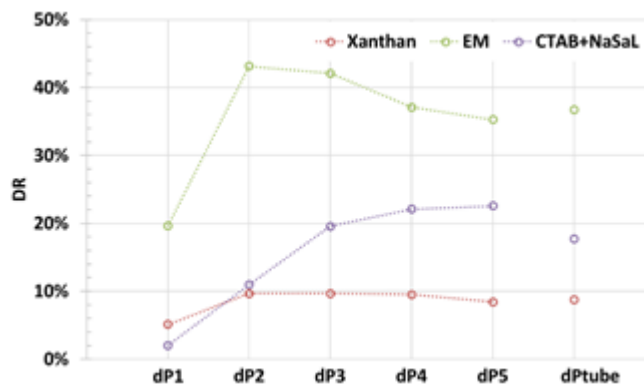


Figure 5-21: %DR at each interval over which the pressure drop is calculated. The pressure drop calculations are taken at a flow rate of 200 ml/min

5.6. Drag Reducing Agent Degradation

Three different methods are used in order to see how degradation affects the solutions that have shown to be effective DRAs. The first method is to prepare a 300 ml solution of the DRAs and run them for at least 2 hours through the flow set-up while monitoring the pressure drop over the inlet and outlet of the test tube every minute. The second method is done simultaneously with the first method; however the second method makes use of the in-line viscosity sensor. This sensor monitors the viscosity at the outlet of the test tube every minute. For these two methods an elbow is introduced at the entrance of the test tube in order to induce additional shear to the agents. The third method is to mechanically shear the DRA solutions for two days in succession after which a rheometer will be used to observe the difference in shear rheology compared to a fresh solution. The results for the third method can be consulted in Appendix C: Degradation Monitoring Using the Rheometer.

5.6.1. Degradation monitoring using pressure drop

The pump used in this experiment has two cylinders with a volume of ~50 cc. The cylinders can be set to work independently or can be set to work together. For the previous flow loop experiments only one and the same cylinder is used. This is done to ensure the same throughput for every solution and therefore make the comparison between the different solutions more reliable. For the degradation experiment a steady delivery rate should be maintained so both cylinders have to work together, and alternately one must fill up as the other cylinder is delivering. The flow rate is set to 140 ml/min to assure turbulent flow through the test tube. For this flowrate the cylinders alternate around three times a minute. Due to wear that could be seen noticeably in the moving parts of cylinder B, the alternation between cylinder A and cylinder B did not go faultlessly. The alternation point is therefore a continuous point that can be seen in the data as fluctuations in the pressure drop. These fluctuations are diminished by averaging the data.

Figure 5-23 exhibits the pressure drop evolution over time for the different DRAs at a flow rate of 140 ml/min, and Figure 5-23 shows the corresponding %DR. From these figures it can be observed that xanthan and the emulsion polymer show a significant DR during the first 20 minutes of the experiment. CTAB+NaSaL on the other hand shows only a small decrease in DR in the first 10 minutes. After the first 10 minutes of the experiment the %DR remains constant. It should be noted that (at a flow rate of 140 ml/min) after little more than 2 minutes all the fluids inside the reservoir have already passed the flow loop and are therefore reused.

The emulsion polymer loses its DR ability the quickest, making it less efficient in looped flow systems. Xanthan also shows degradation as it recirculates in the flow loop. Xanthan is less susceptible to degradation in comparison to the emulsion polymer due to its more rigid chemical structure. But also, xanthan would be inefficient to use in looped flow systems. The CTAB+NaSaL on the other hand shows almost no degradation in the two hours that it is been tested in the flow loop. This means that the micellar rod-like structures that give the DR effect are being repaired when the shear force is being removed. The timescale of the rod-like micelles repairing themselves happens within the timescale needed for the surfactants to reenter the flow loop. This self-healing property of the CTAB+NaSaL mixture makes it perfect for use in looped flow systems. Figure 5-23 and Figure 5-23 furthermore show that the degradation is more severe in the first few minutes and flattens out after the DRA keeps passing the set-up. The reason for this

is that as the chains are being degraded the force exerted on them becomes smaller and smaller until a steady state occurs where all the chains are broken and that the chains cannot be degraded by the flow field anymore.

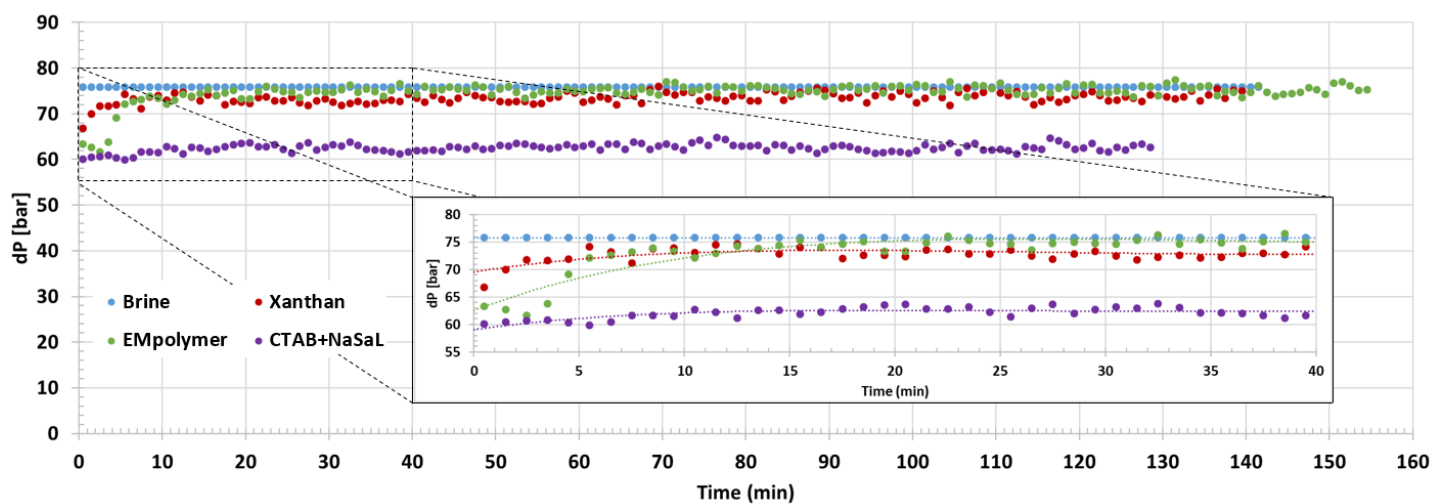


Figure 5-23: Pressure drop evolution over time for the DRAs at a flow rate of 140 ml/min

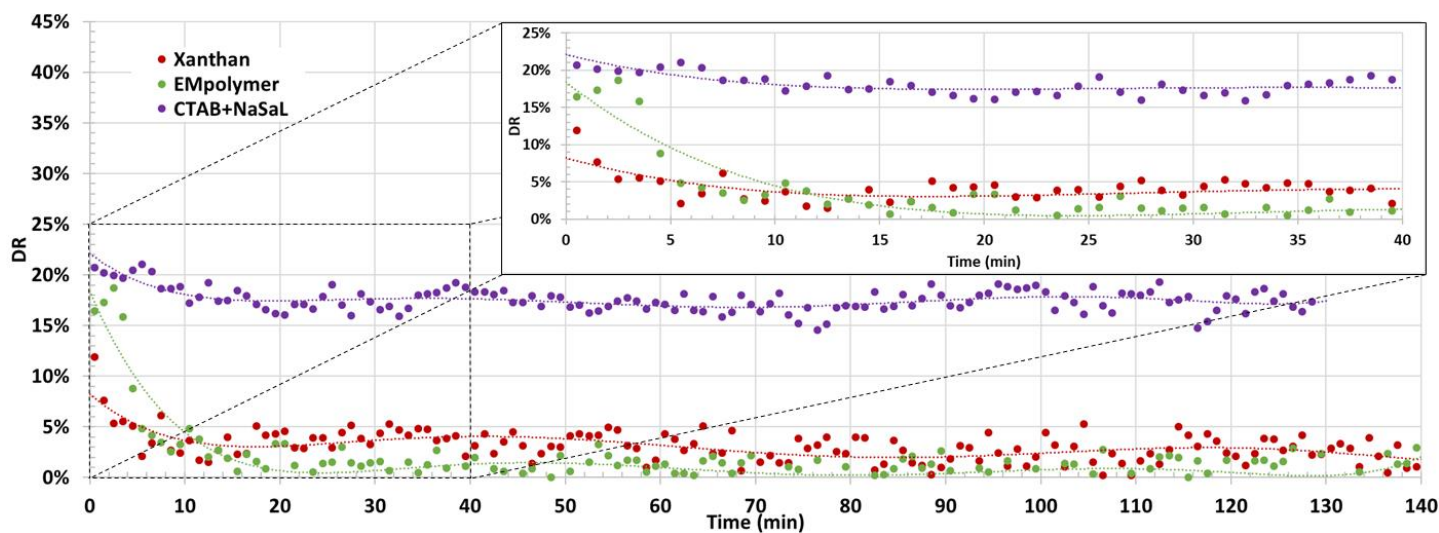


Figure 5-23: DR as function of time for the different DRAs at a flow rate of 140 ml/min

5.6.2. Degradation monitoring using in-line viscosity sensor

The in-line viscosity sensor has an output which is based on the Acoustic Viscosity (AV). In order to know what AV results in what actual viscosity, the sensor is firstly calibrated using a rheometer. This resulted in the following expression for the derived viscosity:

$$\mu = \frac{AV}{\rho}. \quad (5-1)$$

The shear rate at which the viscosity sensor operates is determined using the rheometer and a shear thinning solution. The exact method of calibration is described in Appendix D: Calibration of the In-line Viscosity Sensor.

Figure 5-24 exhibits the AV as function of time for the DRAs. For the polymeric solution a concentration of 90 ppm, and for the CTAB+NaSaL solution a concentration of 2500 ppm was taken. It can be observed that the AV of the polymeric solutions are close to that of brine. This agrees with the results obtained from the shear rheology experiments. The AV of the CTAB+NaSaL solution is significantly higher than that of the other solutions, which is also in agreement with the shear rheology experiments discussed earlier in this report. Appendix D: Calibration of the In-line Viscosity Sensor, showed that an exact ascription of a certain viscosity obtained from the sensor to the solution might be tedious especially at low viscosities. Using the viscosity sensor as a monitoring tool on the other hand should not lead to any problems. The results in Figure 5-24 do not show a significant decrease in AV over the time scale length of this experiment. The AV of xanthan seems to increase after 35 minutes and then decrease back after 78 minutes from the beginning of the experiment. This event can be attributed to a sudden decrease in temperature, after which the temperature goes back to its normal value.

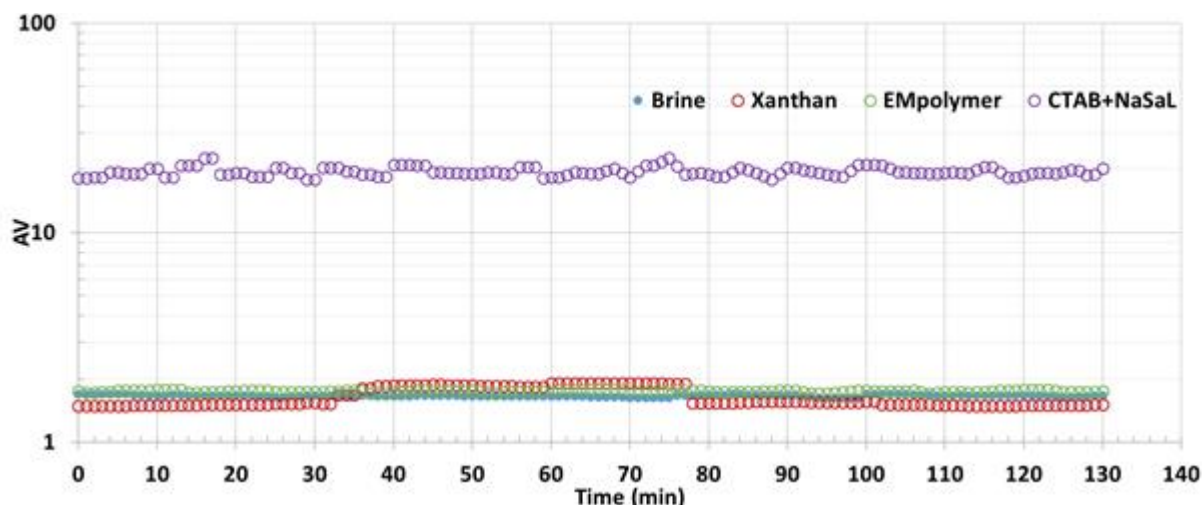


Figure 5-24: Acoustic viscosity (AV) as function of time for the DRAs.

The previous degradation experiment, which monitored the pressure drop over time at a steady flow rate showed that the polymeric DRAs show degradation when continuously percolating through the flow loop. The viscosity sensor did not prove to be useful as a measuring tool for degradation. A reason for this could be that the way of attachment of the sensor to the flow loop using an elbow fitting was not optimal. The elbow increases the risk of having dead volumes and collecting points for debris at the face of the viscosity

sensor. The assumption that due to the high velocities this risk might be ignored could be falsely taken and a dead volume, where the sensor is measuring the same fluid sample over and over again (marked in green in Figure 5-25) needs to be contemplated in this experiment. Using a tee (T) fitting with a set-up as observed in Figure 5-26 is a preferred installation of the viscosity sensor to the flow set-up.

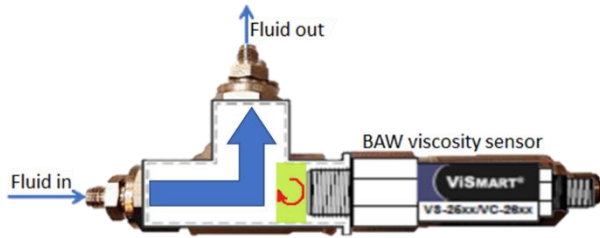


Figure 5-25: Elbow fitting used to connect the viscosity sensor to the flow loop. A dead volume where no flow occurs is marked green

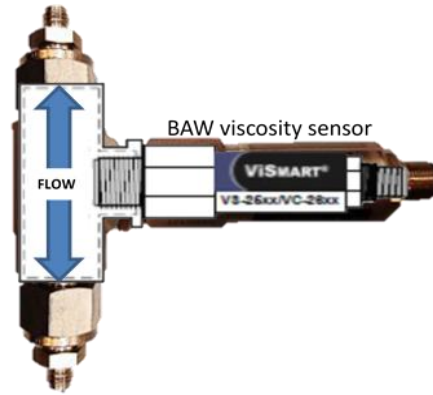


Figure 5-26: Recommended way of connecting viscosity sensor to the flow loop

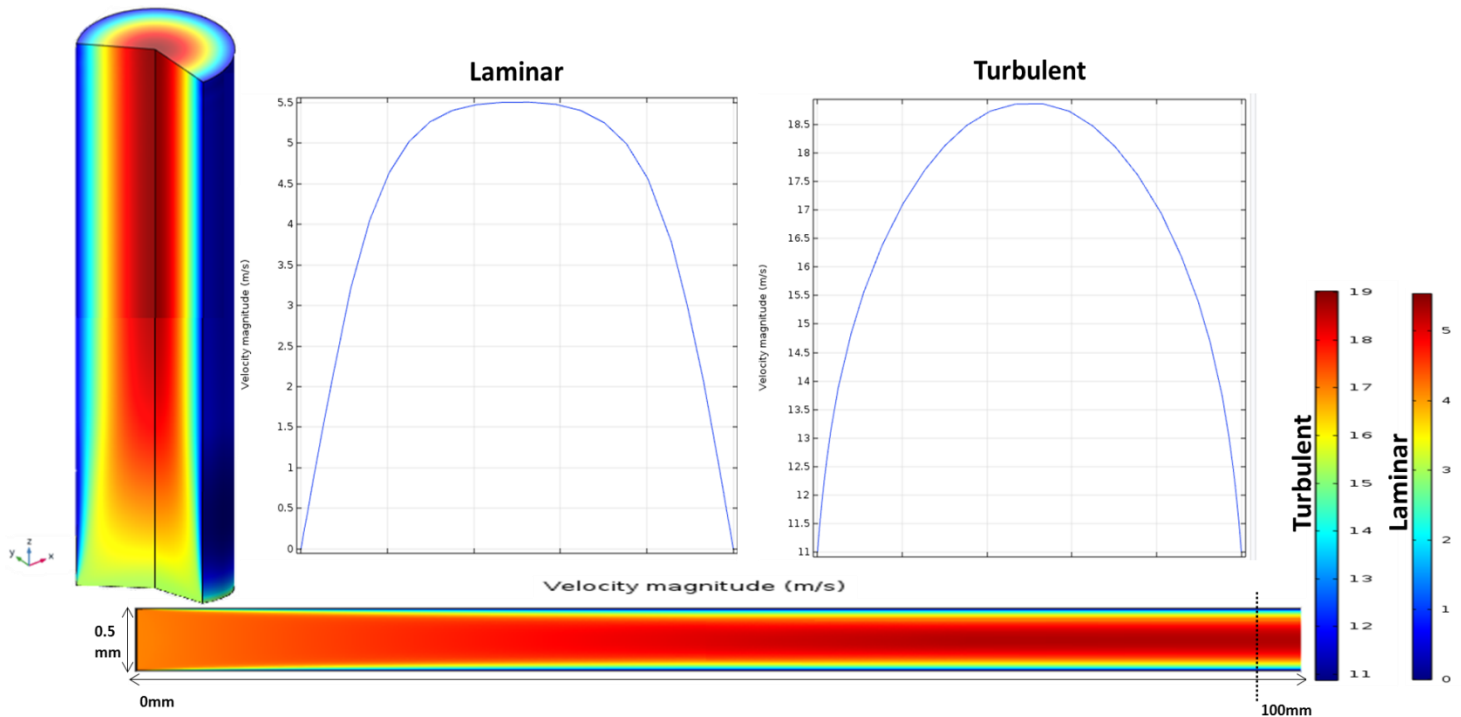


Figure 5-27: Surface plot of the velocity over the first 100 mm of the test tube. The flow enters the test tube from left and flows to the right. Note that the velocity field takes approximately 70 mm to fully develop. The same can be seen in the three dimensional plot. The velocity profiles at laminar and turbulent flow are also plotted. Note that usage of the $k - \epsilon$ model for turbulent flow simulation does not result in having a zero velocity at the boundary wall

5.7. Numerical Results

The numerical $k - \epsilon$ model is used in COMSOL Multiphysics 5.3a to simulate turbulent flow along the test tube. A geometry that resembles the geometry of the test tube is used in this model. The numerically obtained results will be discussed and a comparison with the experimental results are presented. Turbulent flow is simulated by using a flow velocity of 16.97 m/s in the $k - \epsilon$ model. This resembles a flow rate of 200 ml/min, for which the velocity in the test tube is also approximately 16.97 m/s. For the laminar flow simulation a flow velocity of 4.24 m/s is used resembling a flow rate of 50 ml/min, for which the velocity in the test tube is also approximately 4.24 m/s. Figure 5-27 shows the velocity field over the first 100 mm of the test tube. This figure shows that the velocity profile is not fully developed at the entrance of the test tube and needs approximately 70 mm to fully develop. Figure 5-27 also shows the velocity profile at a fully developed laminar and turbulent flows at the location indicated with the dashed line. In the turbulent flow simulator the velocity profile shows that the velocity at the walls is not zero. This can be attributed to the wall functions used in the $k - \epsilon$ model as explained in chapter 4.2.2. Usage of the $k - \epsilon$ model with wall functions can therefore be classified as an unsuitable modelling technique for better understanding the mechanisms of DR, as many theories state that DR is related to locations close to the walls. The solid boundary is a distributed source of vorticity and together with the stretching mechanism they are the main reasons why the interaction of additives with the flow is so important in the near wall region.

A model which incorporates simulations in the near wall region is the Low Reynolds number $k - \epsilon$ model. The low Reynolds number $k - \epsilon$ model also simulates turbulent flow, other than the name makes you think. The flow in this model is overall turbulent but the “low Reynolds” refers to the layer close to the wall. The low Reynolds $k - \epsilon$ model is used for simulating single-phase flows at high Reynolds numbers. The equations solved by the low Reynolds number $k - \epsilon$ model are the Navier-Stokes equations for conservation of momentum and the continuity equation for conservation of mass. Just like the $k - \epsilon$ model whose results are discussed earlier. Turbulence effects are modeled using the AKN two-equation $k - \epsilon$ model. The AKN model is a so-called low-Reynolds number model, which means that it can resolve the flow all the way down to the wall. The AKN model depends on the distance to the closest wall. This model therefore includes a wall distance equation, other than the normal $k - \epsilon$ which uses wall functions as explained in chapter 4.2.2. Figure 5-28 shows the velocity profile obtained by using the low Reynolds $k - \epsilon$ model. It can be observed that usage of this model results in a zero velocity at the wall as is expected. The low Reynolds number $k - \epsilon$ model does require a denser mesh over the whole geometry than the normal $k - \epsilon$ model. This results in long computation times making it a very costly method. Using a dense grid along the walls and a coarser grid at the remaining locations and using the low Reynolds number $k - \epsilon$ to resolve the equations along the walls and the normal $k - \epsilon$ model for the remaining domain can speed up the process.

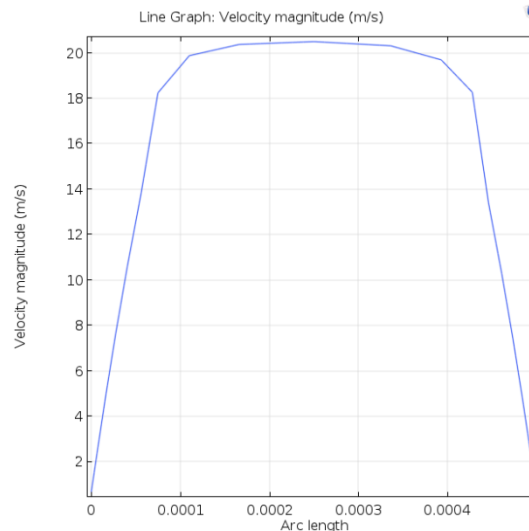


Figure 5-28: Velocity profile derived using the low Reynolds number $k - \epsilon$ model. Note that the velocity is zero at the wall

The pressure along the length of the tube and the fully developed velocity along the radius of the tube is shown in Figure 5-29. The pressure drop over the tube for brine along the test tube was measured to be 9.5 bar at a velocity of 4.24 m/s and 98.89 bar at a velocity of 16.97 m/s. The numerical simulation shows higher pressure drops over the test tube than the pressures measured experimentally. This occurs for both the laminar and the turbulent flow case.

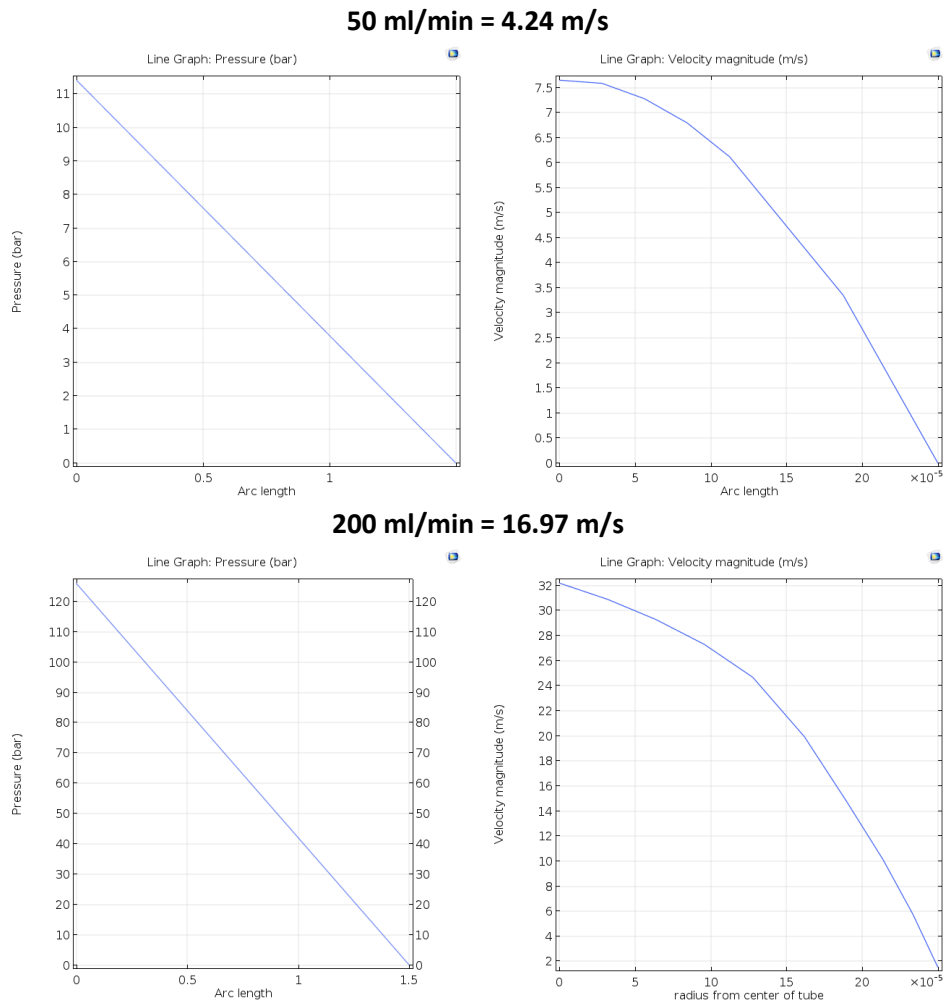


Figure 5-29: Pressure along the length of the tube and the fully developed velocity along the radius of the tube for a velocity of 4.24 m/s and a velocity of 16.97 m/s respectively

6. Conclusion

When a Drag Reducing Agent (DRA) is injected into a pipeline the result is fluid particles moving more efficiently in a less turbulent flow pattern with less wasted energy. Pipelines treated with drag reducing agents operate at lower pressures or provide significant greater throughput. It was possible to design, built and perform measurements with a set-up to measure the drag reduction in pipe flow. This experimental study is performed with the purpose of assessing the drag reducing abilities of certain polymers and surfactants. In order to assess this ability, a set-up capable of achieving turbulent flow is build. The experimental results made it possible to draw the following conclusions:

- **The set-up used in this study** is able to achieve turbulent flows as is validated by running the base case brine through the set-up. A transition from laminar to turbulent flow is observed at flowrates between 70 ml/min and 80 ml/min, which corresponds to Reynolds numbers of ~ 3100 and ~ 3600 respectively. At flowrates above 80 ml/min the flow through the set-up is assumed to be turbulent.
- **Three types of surfactants**, each from a different branch of surfactants are used in this study. The surfactants used are AOS¹, CTAB² and APG³, which are a cationic, anionic and a nonionic surfactant respectively. The CMC for AOS, CTAB and APG are 55 ppm, 65 ppm and 60 ppm respectively.
 - Addition of salts, co-surfactants or counter-ions can induce the formation of rod-like micelles, by neutralizing or dispersing the electrostatic repulsion between the ionic head groups and therefore stabilize the micelle and stimulate formation of larger micelles. Addition of 1-pentanol at concentrations up to 10.000 ppm did not lead to DR. Addition of Sodium Salicylate to CTAB with a 1:1 ratio led to a maximum DR of 33% at 2500 ppm concentration.
 - The AOS and APG surfactants used in this study did not show any DR at (for DRA applications) high concentrations up to 20.000ppm concluding that at these concentrations these surfactants do not contain rod-like micelles.
 - Dynamic Light Scattering (DLS) measurements on various concentrations of AOS revealed that very high concentrations are needed to increase the particle size significantly. The hydrated particle size as function of concentrations first decreases due to the increased repulsion between the AOS molecules at increasing AOS concentration. This repulsion leads to an increase in the rotational speed of the particles causing an apparent decrease in hydrated particle size. The hydrated particle size does not tell much about the micellar shape. For classification of the micellar shape, DLS is simply not enough.

¹ Abbreviation for α -Olefin Sulfonate

² Abbreviation for hexadeCylTrimethylAmmonium Bromide

³ Abbreviation for Alkyl PolyGlucoside

- **The viscosity of the solution is dependent on the concentration of the DRA.** At low concentrations the viscosity enhancement due to the presence of the DRA is negligible. At higher concentrations the viscosity of the DRA increases and behaves as a shear thinning fluid. Finding the correct Reynolds number is therefore difficult due to the difficulties in finding the correct shear stress in a turbulent flow at a certain wall distance. This is because the viscosity of shear thinning polymer solutions can vary with the wall distance.
- **Shear-thinning cannot be the rheological property that is responsible for polymeric DR in turbulent flows,** as the polymeric DRA solutions all showed Newtonian fluid behavior.
 - As polymers xanthan (a biopolymer), and a synthetic emulsion polymer based on polyacrylamide are used. Maximum DR factors are 23% for xanthan at 90ppm and 32% at 90ppm for the synthetic emulsion polymer.
 - Installing several pressure gauges along the test tube showed that xanthan has the same DR factor at each location of the test tube, the emulsion polymer has a decreasing DR factor as the distance from the inlet of the test tube increases. The CTAB+NaSaL DRA has an increasing DR factor as the distance from the inlet increases.
- **Degradation of polymers but no degradation of the CTAB+NaSaL surfactant.**
 - The polymeric DRA effectiveness decreases with time because some of the additives are destroyed or their specific configuration necessary to produce drag reduction is broken down. This effect has a greater impact on the synthetic polymer compared to xanthan, as xanthan has a more rigid chemical structure and is therefore harder to break down.
 - The surfactant solution does not show any degradation over a time period of 2 hours. From this it can be concluded that the micellar rod-like structures present in the solution are able to regenerate after the shear is removed, and that this regeneration happens quickly.
- **DR only occurs at turbulent conditions.**
- **Usage of the $k - \epsilon$ model with wall functions is an unsuitable modelling technique for better understanding the mechanisms of DR,** as the flow is not modelled at the near wall boundary. The solid boundary is a distributed source of vorticity and together with the stretching mechanism they are the main reasons why the interaction of additives with the flow is so important in the near wall region. A low Reynolds number $k - \epsilon$ model can be used instead, but this model needs a much denser grid over the whole geometry leading to an increase in computation time.

7. Recommendations

The following recommendations can be made based on the results from this study:

- **Using a bigger pump** capable of achieving higher Reynolds numbers is useful. In this way a critical Reynolds number at which the maximum DR is obtained, for every solution could be determined.
- **Usage of different diameters test tubes** to see the effect of diameter on the DR for these DRA. Most practical flow systems use larger tube sizes than those used in the laboratory, it is important to be able to scale up to predict drag reduction performance in large pipes from small diameter measurements. Drag reduction prediction for pipes with a different diameter, now that the flow behavior of the solutions in the test pipe is known. One of the most used up-scaling method is the two-loci method of Granville (1977, 1984).
- **Attachment of the first pressure gauge further away from the inlet** of the test tube, to assure a fully developed velocity profile at the measurement point of the first pressure gauge.
- **Usage of other hydrodynamic methods to characterize micellar shape and size**, such as Depolarized Dynamic Light Scattering (DDLDS) or Multi Angle Dynamic Light Scattering (MADLS) are available or even electron microscopy.
- **Checking CTAB and NaSal solutions with different ratios between them** to decrease viscosity enhanced effect but maintain the DR effect.
- **Search for an environmental acceptable surfactant to use as a DRA.** In this study APG was used. Addition of 1-pentanol did not induce the formation of rod-like structures. Addition of other fatty alcohols (hexanol) can be tried.
- **Measure extensional viscosity** for better understanding of DR mechanisms.
- **Addition of a core flood set-up to the current set-up.** In this way the DRA can be tested whether they cause an injectivity decline. This is a key element of using DRA in petroleum well applications. Appendix E: Connection of a Core Flood Set-up, gives more information about why and how a core flood set-up is connected to the current set-up.
- **DR is accompanied by a reduction in the heat transfer coefficient** due to the increase in thermal resistance between the wall and the bulk fluid (White, A., (1970)). This can be very interesting for geothermal applications.
- **Velocity profile measurements** (ultrasound Doppler velocimeter) to determine the structure of turbulence and how DRAs effect these structures.
- **Addition of the DRA behavior to the numerical model.**

Appendix A: z-Average

Dynamic Light Scattering (DLS) data is analyzed using the technique of cumulants as is explained by Koppel, D.E. (1972). This technique makes use of the z-average as it is mathematically stable and insensitive to noise. The z-average is expressed as:

$$D_z = \frac{\sum S_i}{\sum \left(\frac{S_i}{D_i}\right)}, \quad \text{A-1}$$

where, S_i is the scattered intensity from particle i and D_i is the diameter of that same particle. The cumulant analysis uses a polynomial through the log of the correlation function G ,

$$\ln(G) = a + bt + ct^2 + dt^3 + et^4 + \dots, \quad \text{A-2}$$

where b is the z-average diffusion coefficient, the z-average particle size is calculated by using the Stokes-Einstein relation,

$$D_i = \frac{k_B T}{3\pi\mu d}, \quad \text{A-3}$$

where, D_i is the hydrodynamic diameter of particle i , k_B is the Boltzmann's constant, T is the temperature, μ is the dynamic viscosity of the dispersant and b is the z-average diffusion coefficient.

The z-average is only interpreted correctly if the distribution is narrow. The reason behind this is that DLS only uses the first three terms (i.e., a , b and c) for the standard analysis to avoid over-resolving the data. The polydispersity index (PdI) is defined as:

$$PdI = 2c/b^2, \quad \text{A-4}$$

where, b is the coefficient of the second term in equation B-2. The PdI gives an indication of the width of the overall distribution assuming a single mean. For analysis of spherical and monomodal samples with a $PdI < 0.1$, the cumulant analysis gives a good description of the size. For wide distributions with a $PdI > 0.5$ there is a loss of accuracy when solely relying on the z-average. Instead a distribution analysis should be used to determine the peak positions. For $0.1 < PdI < 0.5$ the z-average size can be used for comparative purposes.

Appendix B: Rheology of non DR surfactants

The viscosity versus the shear rate for the solutions that did not show any DR are shown in Figure A. All the solutions behave as a Newtonian fluid. It can be observed that increasing the concentration of AOS leads to higher overall viscosity. That these solutions all behave Newtonian can be an indication that no rod-like micelles are present in the solution and that no 'wormlike' micelles are formed.

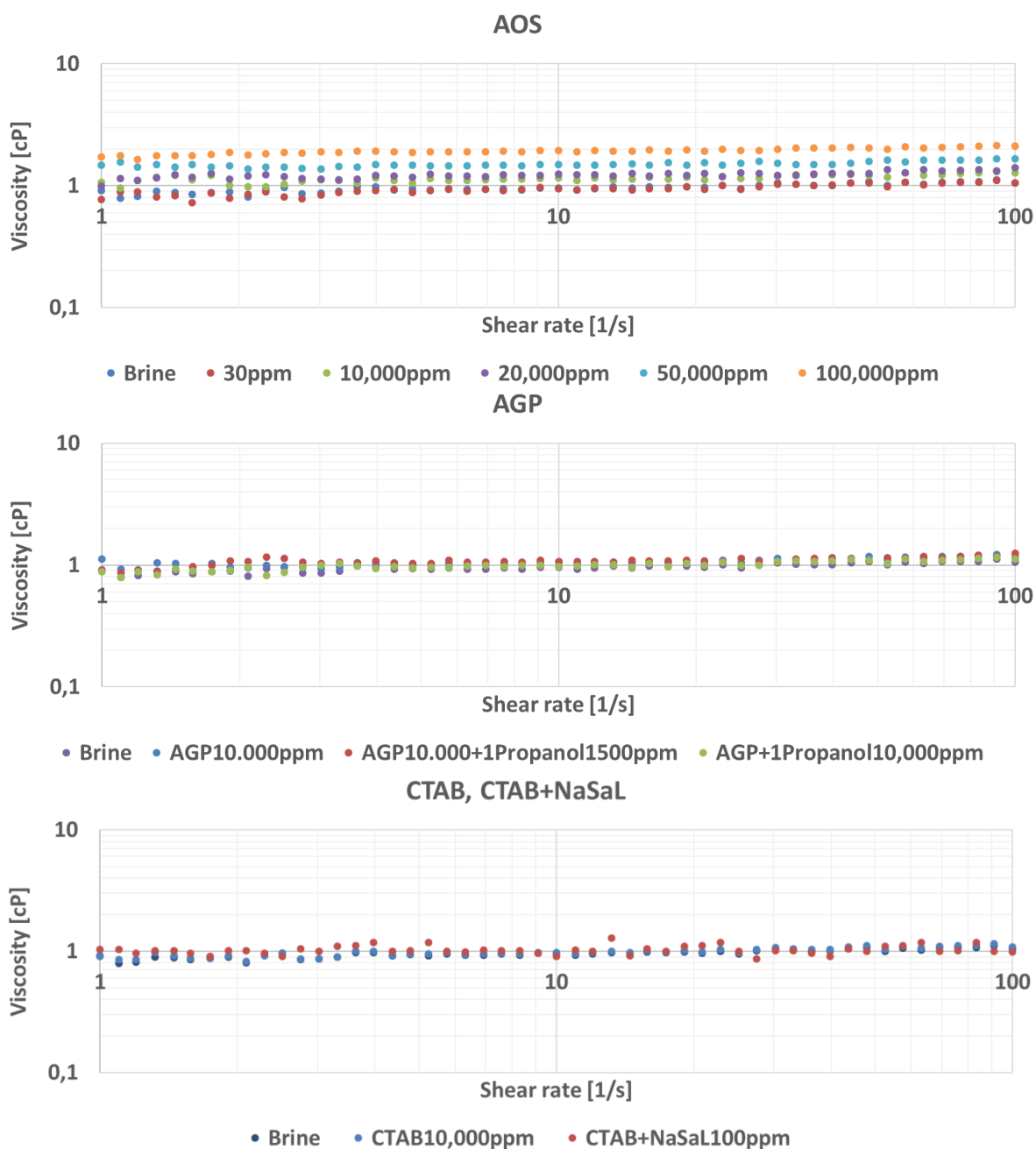


Figure A: Viscosity as function of shear rate for the solutions that did not show DR

Appendix C: Degradation Monitoring Using the Rheometer

The DRA solutions are sheared using a magnetic stirrer at ~ 1000 rpm for two days after which the solutions are studied using the rheometer. The difference between a fresh solution and a two day sheared solution can be viewed in Figure B. The results for the EM polymer after two days of shearing behaves as expected. As the polymer chains are sheared the viscosity should be closer to the viscosity of the dispersant, namely brine. Xanthan seems to obtain an increase in viscosity after two days of shearing. This seems counter intuitive but as xanthan is a biopolymer containing nutrients for all kinds of microorganisms, leading to an increase in the number of micro-organisms. The increased concentration of micro-organisms leads to an apparent increase in viscosity. Indeed, the CTAB+NaSaL solution shows an increase in the viscosity for shear rates in the so called Newtonian plateau. However, as the shear rate increases the sheared CTAB+NaSaL solution and the fresh solution's viscosity curves come together. It might be that the fresh solution is not efficiently dissolved and that the increased time of shearing helped the CTAB+NaSaL to a more complete dissolution.

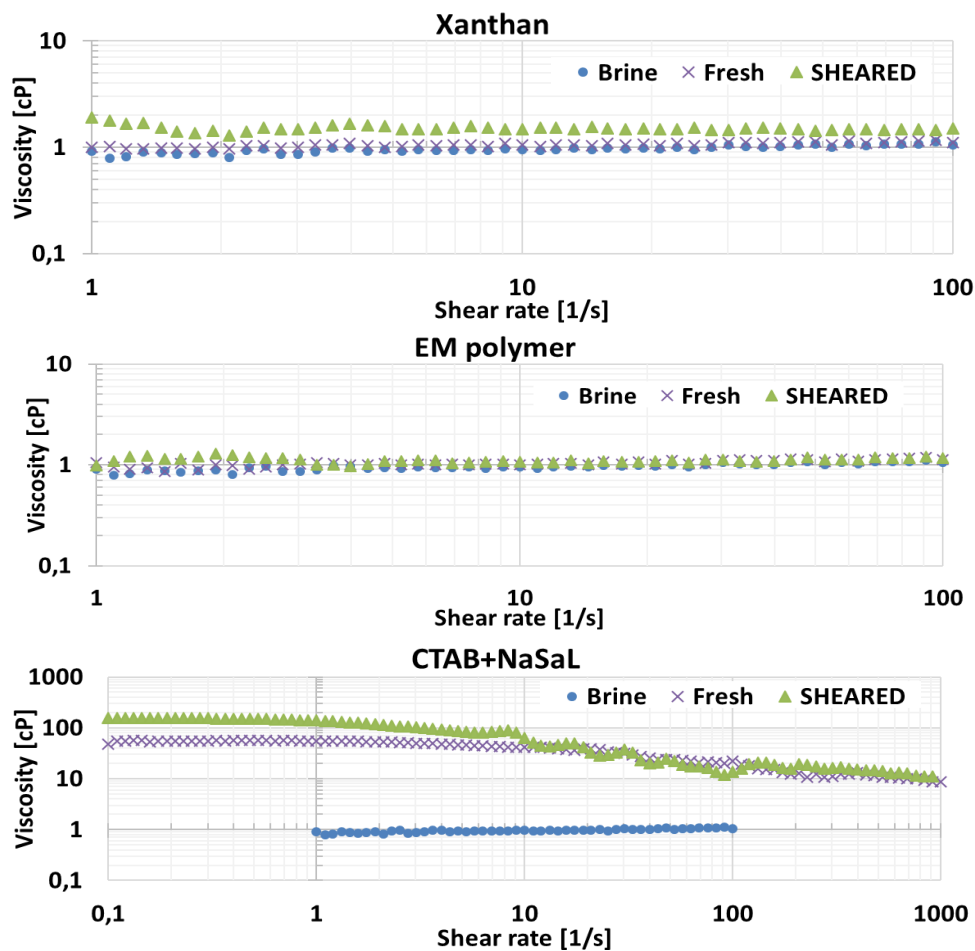


Figure B: Viscosity as function of shear rate for the different DRAs both for a fresh prepared solution as a for 2 days sheared solution

Appendix D: Calibration of the In-line Viscosity Sensor

The viscosity sensor is calibrated using glycerol solutions with different concentrations of glycerol and demineralized water. The sensor has an output in Acoustic Viscosity (AV) that needs to be converted to the dynamic viscosity. The Anton Paar MCR302[®] rheometer is used as calibration tool. Table A, shows 6 different glycerol solutions with their corresponding dynamic and acoustic viscosity. These solutions are made using 86% glycerol. Figure C, shows the viscosity and acoustic viscosity versus the glycerol concentrations. A relationship can be derived from observations of the acoustic viscosity obtained by the sensor and the dynamic viscosity obtained by the rheometer. The relationship is called the theoretical viscosity and states:

$$\mu_{theoretical} = \frac{AV}{\rho}, \quad (D-1)$$

where, AV is the acoustic viscosity and ρ is the density of the solution. As can be observed in Table A, the error between the theoretically obtained viscosity and the viscosity from the Anton Paar rheometer is larger for low viscosities. It is therefore difficult to obtain an exact value for the dynamic viscosity for solutions that are not viscous (i.e., water).

Table A: Information of the used solutions for calibrating the sensor

Glycerol 86% mL	Distilled water mL	Glycerol %	Density g/cm ³	Viscosity cP	Viscosity AV	Theoretic Viscosity cP	Error %
15	0	86%	1,22	115,80	140,921	115,17	1%
13	2	75%	1,19	35,52	40,873	34,24	4%
11	4	63%	1,16	15,09	19,590	16,83	12%
9	6	52%	1,13	7,66	8,073	7,12	7%
7	8	40%	1,10	4,38	6,826	6,18	41%
0	15	0%	1,00	1	1,386	1,39	39%

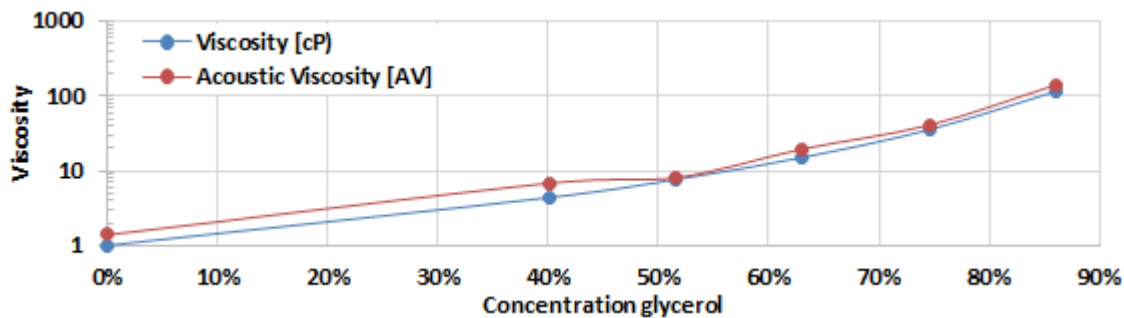


Figure C: Viscosity against concentration glycerol

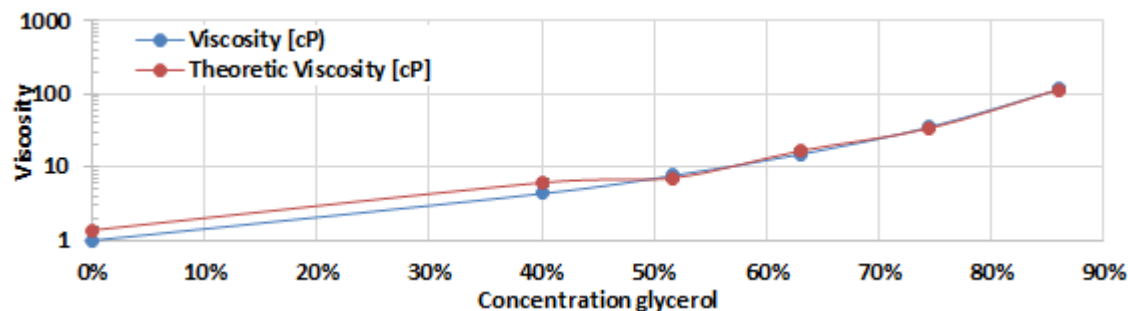


Figure D: Viscosity against glycerol concentration for the dynamic viscosity and the theoretical viscosity

The shear rate at which the viscosity sensor operates is also determined using the rheometer. Only in this case a shear thinning fluid is used instead of glycerol, which behaves Newtonian. The shear thinning fluid should have a high viscosity enhancing power, but within the read range of the viscosity sensor in order to have a reliable result. The CTAB+NaSaL 2500 ppm solution is used as a shear thinning fluid. By looking at the results obtained from the rheometer and from the viscosity sensor one can derive that the viscosity sensor operates at a shear rate of $\sim 100 \text{ s}^{-1}$. The viscosity sensor is then connected to the flow loop using the elbow connection. A 50% glycerol solution is introduced to the flow loop and the acoustic viscosity is measured as the glycerol flows through the set-up. The measurements are done for multiple flowrates and the results are shown in Table B. The theoretic viscosity matches the dynamic viscosity of 50% glycerol at 26°C obtained using the rheometer. It can be observed that the value for the acoustic viscosity varies with the flowrate. This might be explained by the fact that the sensor is not connected properly and that there might be a dead volume in front of the sensors surface. Summarizing, it can be stated that the viscosity sensor can be used to monitor the solutions flowing through the set-up but deriving the precise values for the viscosity using solely the sensor might be tedious, especially for solutions in the low viscosity range.

Table B: Data obtained from the viscosity sensor whilst being connected to the flow loop. The theoretic viscosity is calculated using the equation provided earlier.

Flowrate [ml/min]	content	Av. Temp [deg. C]	Av. AV [-]	Density [g/cm ³]	$\mu_{theoretical}$ [mPa*s]
100	water	27	1.54	0.997	1.54
100	water	27	1.66	0.997	1.67
150	water	27	1.66	0.997	1.66
200	water	27	1.79	0.997	1.79
200	water	28	1.75	0.997	1.75
100	glycerol	26	11.00	1.144	9.61
50	glycerol	26	10.74	1.144	9.39

Appendix E: Connection of a Core Flood Set-up

At low concentrations the polymer solutions behave like a colloidal solution, where the polymer molecules are coiled into small spheres. At turbulent flow, a coil stretch transition can occur where the stretched molecules can reduce the turbulence and cause DR. Using low concentrations of polymer solutions can therefore be helpful in water injection sites by decreasing the pumping power. A drawback can be that the coiled spheres can cause injection problems in the reservoir rock by plugging the pores. Therefore to get an idea of the injectivity decline caused by the DRAs, a core flood set-up can be attached to the current set-up as is shown in Figure E. The surfactant DRAs are not expected to plug the core and therefore no injectivity decline in the porous medium should occur when using surfactant DRAs at low concentrations.

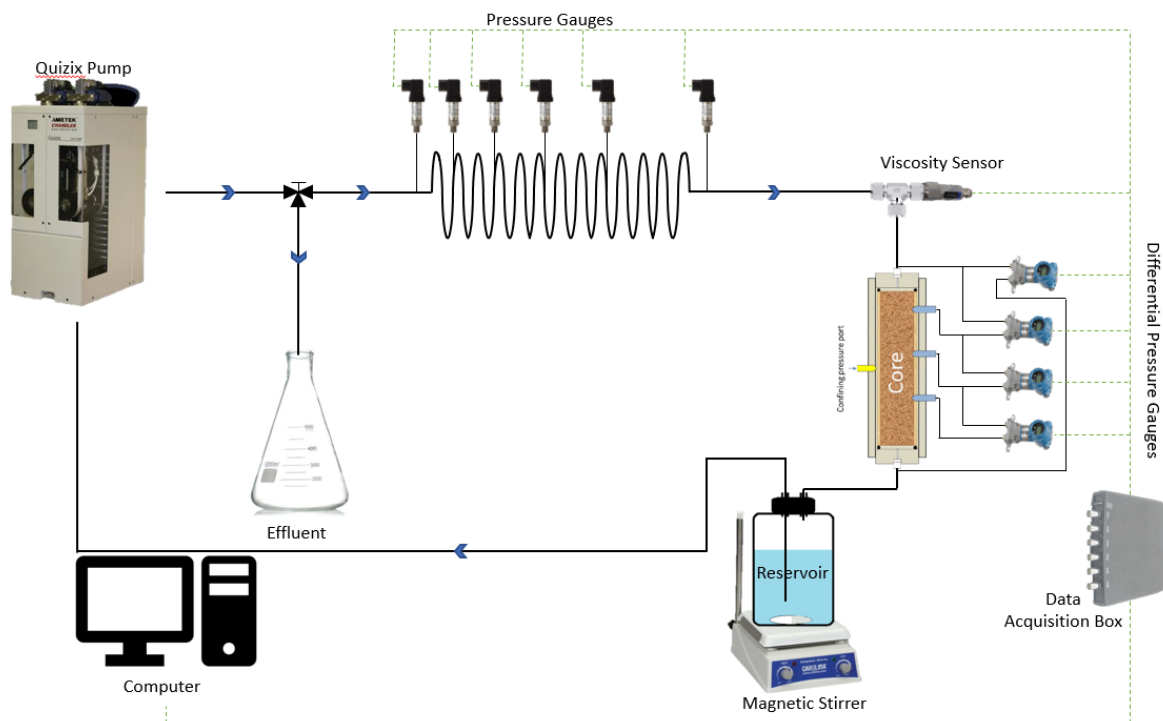


Figure E: Schematic view of the set-up where a core flood set-up is attached

Appendix F: PHREEQC Geochemical Simulation

The brine used in this study has the following molality for the different ions in one kg of water:

Na	K	Ca	Mg	S (6)	Cl
443.0809	9.488904	19.41215	100.9669	51.5922	521.141

PHREEQC calculates the equilibrium concentrations of the mixture. The results are shown below:

```

-----Solution composition-----

```

Elements	Molality	Moles
Ca	1.941e-02	1.941e-02
Cl	5.211e-01	5.211e-01
K	9.489e-03	9.489e-03
Mg	1.010e-01	1.010e-01
Na	4.431e-01	4.431e-01
S (6)	5.159e-02	5.159e-02

```

-----Description of solution-----

```

pH	=	7.000
pe	=	4.000
Specific Conductance (µS/cm, 25°C)	=	51685
Density (g/cm³)	=	1.02553
Volume (L)	=	1.01140
Activity of water	=	0.981
Ionic strength (mol/kgw)	=	7.300e-01
Mass of water (kg)	=	1.000e+00
Total alkalinity (eq/kg)	=	1.204e-06
Total carbon (mol/kg)	=	0.000e+00
Total CO2 (mol/kg)	=	0.000e+00
Temperature (°C)	=	25.00
Electrical balance (eq)	=	6.900e-02
Percent error, 100*(Cat- An)/(Cat+ An)	=	5.67
Iterations	=	7
Total H	=	1.110124e+02
Total O	=	5.571259e+01

-----Distribution of species-----

Species	Molality	Activity	Log		Log Gamma	mole cm ³ /mol
			Molality	Activity		
OH-	1.647e-07	9.930e-08	-6.783	-7.003	-0.220	-2.54
H+	1.329e-07	1.000e-07	-6.876	-7.000	-0.124	0.00
H2O	5.551e+01	9.810e-01	1.744	-0.008	0.000	18.07
Ca	1.941e-02					
Ca+2	1.698e-02	4.218e-03	-1.770	-2.375	-0.605	-16.65
CaSO4	2.433e-03	2.878e-03	-2.614	-2.541	0.073	7.50
CaOH+	9.122e-09	6.867e-09	-8.040	-8.163	-0.123	(0)
CaHSO4+	2.513e-09	1.892e-09	-8.600	-8.723	-0.123	(0)
Cl	5.211e-01					
Cl-	5.211e-01	3.262e-01	-0.283	-0.486	-0.203	18.82
H(0)	1.197e-25					
H2	5.984e-26	7.079e-26	-25.223	-25.150	0.073	28.61
K	9.489e-03					
K+	9.259e-03	5.724e-03	-2.033	-2.242	-0.209	9.70
KSO4-	2.300e-04	1.543e-04	-3.638	-3.812	-0.173	34.88
Mg	1.010e-01					
Mg+2	8.278e-02	2.392e-02	-1.082	-1.621	-0.539	-20.37
MgSO4	1.818e-02	2.151e-02	-1.740	-1.667	0.073	5.84
MgOH+	1.215e-06	8.518e-07	-5.915	-6.070	-0.154	(0)
Na	4.431e-01					
Na+	4.341e-01	3.121e-01	-0.362	-0.506	-0.143	-0.47
NaSO4-	8.945e-03	6.003e-03	-2.048	-2.222	-0.173	21.54
NaOH	2.620e-18	3.099e-18	-17.582	-17.509	0.073	(0)
O(0)	0.000e+00					
O2	0.000e+00	0.000e+00	-42.170	-42.097	0.073	30.40
S(6)	5.159e-02					
SO4-2	2.180e-02	3.837e-03	-1.662	-2.416	-0.754	17.62
MgSO4	1.818e-02	2.151e-02	-1.740	-1.667	0.073	5.84
NaSO4-	8.945e-03	6.003e-03	-2.048	-2.222	-0.173	21.54
CaSO4	2.433e-03	2.878e-03	-2.614	-2.541	0.073	7.50
KSO4-	2.300e-04	1.543e-04	-3.638	-3.812	-0.173	34.88
HSO4-	4.955e-08	3.731e-08	-7.305	-7.428	-0.123	40.99
CaHSO4+	2.513e-09	1.892e-09	-8.600	-8.723	-0.123	(0)

-----Saturation indices-----

Phase	SI**	log IAP	log K(298 K, 1 atm)	
Anhydrite	-0.51	-4.79	-4.28	CaSO4
Gypsum	-0.23	-4.81	-4.58	CaSO4:2H2O
H2(g)	-22.05	-25.15	-3.10	H2
H2O(g)	-1.51	-0.01	1.50	H2O
Halite	-2.56	-0.99	1.57	NaCl
O2(g)	-39.20	-42.10	-2.89	O2
Sylvite	-3.63	-2.73	0.90	KCl

Bibliography

Cover image: <http://www.arcticphoto.co.uk/gallery2/arctic/modern/industry/ak0917-23.htm>

Abdulbari, H.A., Yunus, R.M., Abdurahman, N.H. & Charles, A., (2013) *Going against the flow- A review of non-additive means of drag reduction*. J. Ind. Eng. Chem., 19, 27

Abed, M.A., Saxena, A. & Bohidar, H.B., (2004) *Micellization of alpha-olefin sulfonate in aqueous solutions studied by turbidity, dynamic light scattering and viscosity measurements*. Colloids and Surfaces A: Physicochem. Eng. Aspects 233 pp: 181–187

Berne, B.J. & Pecora, R., (1976, 2000) *Dynamic Light Scattering With Applications to Chemistry, Biology and Physics*. John Wiley and Sons, ISBN 0-486-41155-9

Bruining J. and Fijnaut, H.M., (1979) *A Rotational Diffusion Coefficient of the 70s Ribosome Determined using Depolarized Laser Light Scattering*. Biophys. Chem 9(4), 345-353

Burger, E.D., Munk, W.R. & Wahl H.A., (1982) *Flow increase in the Trans Alaska Pipeline Through Use of a Polymeric Drag-Reducing Additive*. SPE: 10.2119.9419-PA

Brostow, W., (2008) *Drag reduction in flow: Review of applications mechanism and prediction*, Journal of Industrial and Engineering Chemistry Volume 14, Issue 4, Pages 409-416

Cai, S. & Higuchi, Y., (2014) *Drag-reduction behavior of an unusual nonionic surfactant in a circular pipe turbulent flow*. Journal of Hydrodynamics 26: pp 400-405

Chou, L.C., (1991) *Drag reducing cationic surfactant solutions for district heating and cooling systems*. Ph.D. Thesis, The Ohio State University

Colebrook, C.F., (1939) *Turbulent Flow in Pipes with Particular reference to the Transition Region between the Smooth and Rough Pipe Laws*. J. Inst. of Civil Engrs., 11, pp 133-156

De Gennes, P.G., (1986) *Towards A Scaling Theory of Drag Reduction*. Physica, 140A, pp. 9-25

Drappier, J., Divoux, T., Amarouchene, Y., Bertrand, F., Rodts, S., Cadot, O., Meunier, J. & Bonn, D., (2006) *Turbulent drag reduction by surfactants*. Europhys. Lett., 74 (2), pp. 362-368

Granville, P.S., (1977) *Scaling-up of pipe flow frictional data for drag reducing polymer solutions*. Proc. 2nd Int. Conf. on drag reduction, BHRA (eds. Stephens, H.S. & Clarke, J.A.) Cambridge 81,1-12

Granville, P.S., (1984) *A method for predicting additive drag reduction for small diameter pipe flow*. Proc. 3rd Int. Conf. on drag reduction, BHRA (eds. Sellin, R.H.J. & Moses, R.T.) Bristol C3,1-8

Gyr, A. and Bewersdroff, H.-W., (1995) *Drag Reduction of Turbulent Flows by Additives*. Kluwer Academic Dordrecht, The Netherlands

Hamley, I. W., (2000) *Introduction to soft matter*. Polymers, Colloids, Amphiphiles and Liquid Crystals Wiley, England

Hellsten, M., (2002) *Drag-Reducing Surfactants*. Journal of Surfactants and Detergents, vol. 5, No. 1

Hinch, E.J., (1977) *Mechanical Models of Dilute Polymer Solutions in Strong Flows*. The Physics of Fluids, 20 (10), pp. S22-S30

Hellsten, M., & Harwigsson, I., (1994) *A new biodegradable friction reducing additive (FRA) for district cooling networks*. Proceedings of the 85th International District Heating and Cooling Association

Huang, T., & Crews, J.B., (2008) *Nanotechnology Applications in Viscoelastic Surfactant Stimulation Fluids*. Society of Petroleum Engineers. doi:10.2118/107728-PA

Hunter, R. J., (2001) *Foundations of Colloid Science*. 2nd edition, Oxford University Press, -Knovel Library, Ch 9, ISBN 019-5850502

Jouenne, S., Anfray, J., Cordelier, P.R., Mateen, K. & Levitt, D., (2015) *Degradation (or Lack Thereof) and Drag Reduction of HPAM Solutions During Transport in Turbulent Flow in Pipelines*. Society of Petroleum Engineers. doi:10.2118/169699-PA

Kampen Van, N.G., (2007) *Stochastic Processes in Physics and Chemistry*. 3rd Edition, North Holland, Ch 1, ISBN 9780444529657

Kim, N.J., Kim, S., Lim, S.H., Chen, K., & Chun, W., (2009) *Measurement of drag reduction in polymer added turbulent flow*. Int. Commun. Heat Mass Transfer, 36, 1014

Koppel, D.E., (1972) *Analysis of Macromolecular Polydispersity in Intensity Correlation Spectroscopy: The Method of Cumulants*, J. Chem. Phys 57 (11), pp 4814-4820

Landau, L.D., & Lifshitz, E.M., (1959) *Fluid Mechanics*, Vol 6 of course of Theoretical Physics, 2nd Edition, Pergamon Press (1959), ISBN 0-08-033932-8

- Landahl, M.T., (1977) *Dynamics of Boundary Layer Turbulence and the Mechanism of Drag Reduction*. The Physics of Fluids, 20 (10), pp. S55-S63
- Liaw, G., Zakin, J.L. & Patterson, G.K., (1971) *Effects of Molecular Characteristics of Polymers on Drag Reduction*. AIChE J., Vol 17 nr 2, pp. 391-397
- Li, P.W., Kawaguchi, Y. & Yabe, A., (2000) *Feasibility Study of New Heat Transportation System With Drag-Reducing Surfactant Additives*. Symposium on Energy Engineering in the 21st century, Ping Cheng Ed., pp 716-722 in proceedings
- Lu, B., (1997) *Ph.D. Dissertation*, The Ohio State University, Columbus, Ohio
- Lumley, J.L., (1969) *Drag Reduction by Additives*. Ann. Rev. Fluid Mech., 1, pp. 367-383
- Lumley, J.L., (1973) *Drag Reduction in Turbulent Flow by Polymer Additives*. J. Polymer Sci.: Macromol. Rev., 7, pp. 263-290
- Mohammadi, B. and Pironneau, O., (1994) *Analysis of the K-Epsilon Turbulence Model*. John Wiley, ISBN-0298-3168, pp 58-62.
- Moody, L.F., (1944) *Friction Factors for Pipe Flow*. Transactions of the American Society of Mechanical Engineers, 66, 671-681
- Mysels, K.J., (1949) *U.S. Patent 2, 492173*.
- Odell, J.A. & Keller, A., (1986) *Flow-induced Chain Fracture of Isolated Linear macromolecules in solution*. Journal of Polymer Sciences Part BL Polymer Physics, vol 24, issue 9, pp. 1889-1916
- Ohlendorf, D., Interhal, W., & Hoffmann, H., (1986) *Surfactant systems for drag reduction: physico-chemical properties and rheological behavior*. Rheo Acta 25 468-486
- Padday, J.F., Pitt, A.R. & Pashley, R.M., (1975) *Menisci at a free liquid surface: surface tension from the maximum pull on a rod*. J. Chem. Soc., Far. Trans. I, 71(10), 1919-1931
- Singh, R.P., (2002) *Drag reduction*, in *Encyclopedia of Polymer Science and Technology*. J. I. Kroschwitz Ed., John Wiley & Sons, Inc., New Jersey, 519
- Sohn, J.I., Kim, C.A., Choi, H.J. & Jhon, M.S., (2000) *Drag-reduction effectiveness of xanthan gum in a rotating disk apparatus*. Elsevier
- Sorbie, K.S., (1991) *Polymer-Improved Oil Recovery*. Springer Science+Business Media New York

- Stradner, A., Glatter, O. & Schurtenberger, P., (2000) *A hexanol-induced sphere-to-flexible cylinder transition in aqueous alkyl polyglucoside solutions*. *Langmuir* 2000;16:5354_5364.
- Tanford, C., (1972) *Micelle Shape and Size*. *J. Phys. Chem.* 76:3020
- Tiong, A.N.T., Kumar, P. & Saptoru, (2015) *Reviews on Drag Reducing Polymers*. *A. Korean J. Chem. Eng.*
- Toms, B.A., (1949) *Some Observation on the Flow of Linear Polymer Solutions through Straight Tubes at Large Reynolds Number*. *Proceedings of the First International Congress of Rheology, North Holland, Amsterdam, 2*, pp. 135-141,
- Toms, B.A., (1977) *On the early experiments on drag reduction by polymers*, *The physics of fluids, Vol 20* (10) S1-S5
- Virk, P.S., Merrill, E.W., Mickley, H.S., Smith K.A., & Mollo-Christensen, E.L., (1967) *The Toms phenomenon: turbulent pipe flow of dilute polymer solutions*. *J. Fluid Mech.*, 30, 305
- White, A., (1970) *Heat Transfer Characteristics of Dilute Polymer Solutions in Fully Rough Pipe Flow*. *Nature*, 227(5257), 486-487
- Wu, S.J., Hsu, C.H., & Lin, T.T., (2007) *Model test of the surface and submerged vehicles with the micro-bubble drag reduction*. *Ocean Eng.*, 34, 83
- Wu, S.J., Ouyang, K., & Shiah, S.W., (2008) *Robust design of microbubble drag reduction in a channel flow using the Taguchi method*. *Ocean Eng.*, 35, 856
- Wyatt, N.B., Gunther, C.M., & Liberatore, M.W., (2010) *Drag reduction effectiveness of dilute and entangled xanthan in turbulent pipe flow*. Elsevier
- Zakin, J.L., B. Lu, & H.-W. Bewersdorff, (1998) *Surfactant Drag Reduction*. *Rev. Chem. Eng.* 14:253.
- Zakin, J.L., Brosh, M., Poreh A., & Warshavsky, M., (1971) *Exploratory study of friction reduction in slurry flows*. *Chem. Eng. Professional Symposium Series*, 67, 85
- Zigrang, D.J. & Sylvester, N.D., (1985) *A Review of Explicit Friction Factor Equations*. *ASME. J. Energy Resour. Technol.*107(2):280-283.

2018

Azeddine Toutouh

Drag Reduction in Turbulent Flows by Polymers and Surfactants

Drag Reduction in Turbulent Flows by Polymers and Surfactants

An Experimental Study Into the Mechanisms of Drag Reduction by Additives

A. Toutouh

